Forschungszentrum Jülich
in der Helmholtz-Gemeinschaft

Fabrication and characterization of planar Gunn diodes for Monolithic Microwave Integrated Circuits

Simone Montanari

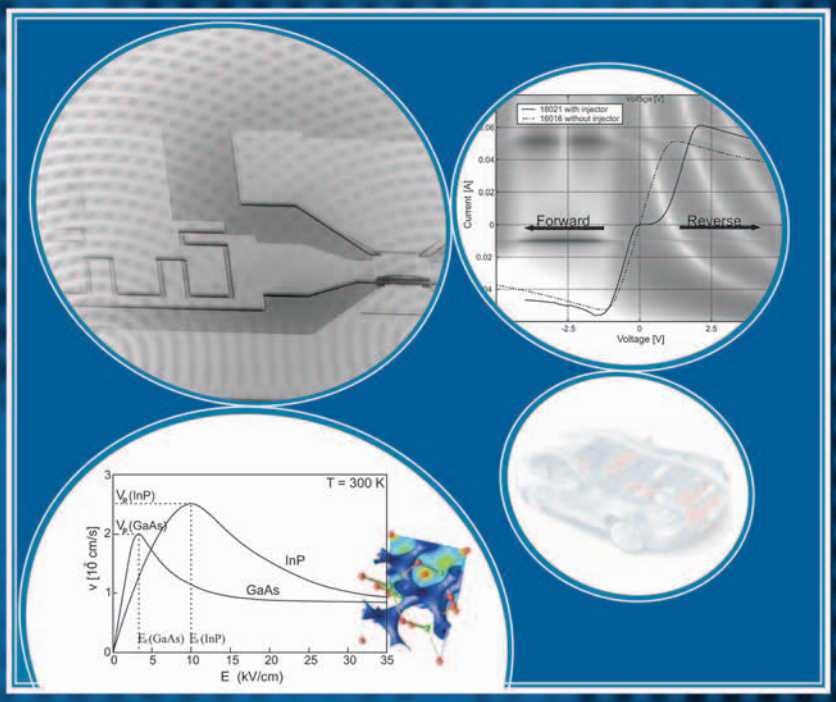

Informationstechnik
Information Technology

Schriften des Forschungszentrums Jülich
Reihe Informationstechnik / Information Technology Band / Volume 9

Forschungszentrum Jülich GmbH
Institut für Schichten und Grenzflächen

Fabrication and characterization of planar Gunn diodes for Monolithic Microwave Integrated Circuits

Simone Montanari

Schriften des Forschungszentrums Jülich
Reihe Informationstechnik / Information Technology Band / Volume 9

ISSN 1433-5514 ISBN 3-89336-396-3

Bibliographic Information published by Die Deutsche Bibliothek.
Die Deutsche Bibliothek lists this publication in the Deutsche Nationalbibliografie; detailed bibliographic data are available in the Internet <http://dnb.ddb.de>.

Publisher and Distributor:	Forschungszentrum Jülich GmbH Zentralbibliothek 52425 Jülich Phone +49 (0)2461 61-5368 · Fax +49 (0)2461 61-6103 e-mail: zb-publikation@fz-juelich.de Internet: http://www.fz-juelich.de/zb
Cover Design:	Grafische Betriebe, Forschungszentrum Jülich GmbH
Printer:	Grafische Betriebe, Forschungszentrum Jülich GmbH
Copyright:	Forschungszentrum Jülich 2005

Schriften des Forschungszentrums Jülich
Reihe Informationstechnik / Information Technology Band / Volume 9

D 82 (Diss., Aachen, RWTH, 2005)

ISSN 1433-5514
ISBN 3-89336-396-3

Fabrication and characterization of planar Gunn diodes for Monolithic Microwave Integrated Circuits.

In the present dissertation, GaAs and GaN Gunn diodes have been investigated with respect to microwave generation in the field of automotive intelligent radar systems.
High quality planar Gunn diodes have been fabricated with two different hot electron injectors: a graded gap injector (GGI) and a novel resonant tunneling injector (RTI). Within the framework of the cooperation project between Forschungzentrum Jülich and Robert Bosch GmbH, GGI GaAs Gunn diodes have been studied and optimized. RF evaluation of their performance up to 110 GHz shows the effectiveness of different graded gap injectors. An estimation of the possible operational modes is given for diodes used as microwave generators at 77 GHz, with application in automotive radar systems. A second hot electron injector, the GaAs/AlAs double barrier resonant tunnelling injector has been proposed and designed. GaAs Gunn diodes with RTI have been successfully fabricated and characterized. RTI Gunn diodes present clear evidence of the injector effectiveness both in DC and RF conditions.
The design, processing and characterization of a novel GaAs Gunn diode based VCO-MMIC[1] fulfilled the second objective of this work. A simple and straightforward processing technology makes the proposed microwave generator competitive with cavity oscillators and transistor based MMICs.

Herstellung und Charakterisierung planarer Gunn-Dioden für monolitisch integrierte Mikrowellen-Oszillatoren.

In der vorliegenden Arbeit werden GaAs und GaN Gunn-Dioden für die Mikrowellenerzeugung in der Automobil-Branche untersucht.
Qualitativ hochwertige planare GGI Gunn-Dioden wurden mit zwei verschiedenen hot electron injectors hergestellt: ein graded gap injector (GGI) und ein resonant tunneling injector (RTI). Im Rahmen der Zusammenarbeit des Forschungszentrums Jülich mit der Robert Bosch GmbH erfolgte die Untersuchung und Optimierung von GGI GaAs Gunn-Dioden. Die Beurteilung des RF-Verhaltens bis 110 GHz zeigt die Effektivität der verschiedenen Graded Gap Injectors. Dargestellt ist eine Abschätzung der möglichen Arbeitsmodi für Dioden, welche als Mikrowellenerzeuger bei 77 GHz in Radarsystemen in der Automobilbranche Einsatz finden. Ein zweiter neuer hot electron injector, der GaAs/AlAs Doppelbarrieren RTI konnte erfolgreich vorgeschlagen und simuliert werden. GaAs Gunn-Dioden mit RTI wurden hergestellt und charakterisiert. Für beide, DC und RF Bedingungen zeigt die RTI Gunn-Diode deutliche Beweise für die Effektivität des injectors.
Mit dem Entwurf, der Prozessierung und der Charakterisierung eines neuartigen monolitisch integrierten Oszillators (MMIC-VCO), basierend auf einer GaAs Gunn-Diode, wird die zweite Zielsetzung innerhalb dieser Arbeit erfüllt. Durch die einfache und direkte Prozessierungstechnologie ist die hier vorgeschlagene Mikrowellenerzeugung konkurenzfähig zu Hohlraumresonator-Oszillatoren und transistorbasierten MMICs.

[1] Voltage Controlled Oscillator Monolithic Microwave Integrated Circuit.

Contents

Chapter 1

Introduction

Microwave generation for automotive applications

According to the World Health Organization [PSS+04], 1.2 million people died and about 50 million people were injured in the world due to road accidents during 2002. In economic terms, the costs of global road crashes have been estimated at US$ 518 billion. Aiming at the reduction of road accidents, various countermeasures have been developed: education, enforcement, engineering, and so forth.

The challenge of adaptive cruise control (ACC) and collision warning systems on passenger automobiles and long-haul trucks excite manufacturers of vehicles and radar modules as well. Three competing and potentially complementary technologies have appeared on the market: microwave, ultrasonic and conventional or infrared imaging systems (Fig. 1.1). Compared to optical systems, microwave sources have the advantage of being able to work in dusty, foggy or rainy environments. Ultrasonic sensors are in widespread use for parking aids, but with a typical range of less than 3 m and no facility for accurate object or speed discrimination, this technology does not represent an alternative to microwave systems.

There are many types of millimeter-wave radar system for automotive applications, differing by the method used to determine the distance and relative vehicle velocity. In this sense, one can distinguish: pulse radars, frequency-modulated continuous-wave

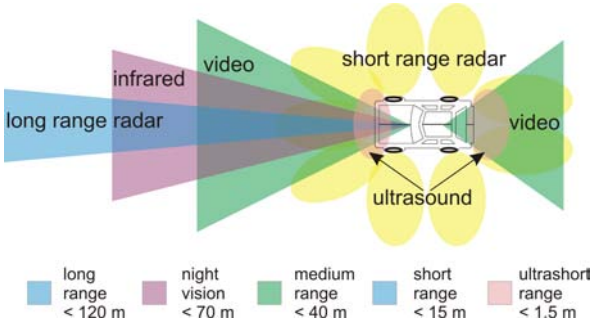

Figure 1.1: Comparison between long, middle and short range technologies.

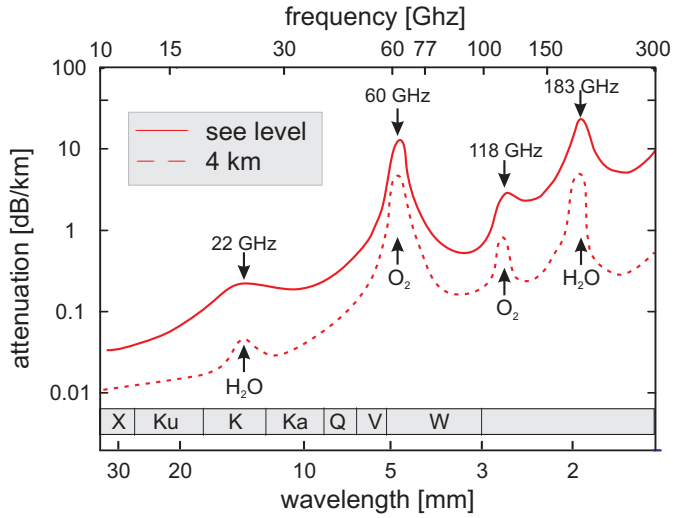

Figure 1.2: Atmospheric attenuation versus millimeter wavelengths. The IEEE radar bands are also shown [AM88].

radars and spread spectrum radars. Basically, the distance from the radar to the target is detected by measuring a time delay and the relative velocity of the target is obtained from the Doppler shift.

Integrating a sensitive radar module and its associated antenna into a vehicle platform is not an easy task. The introduction of new technologies like millimeter-wave radar testing into production facility, coupled with the requirement to drive costs as low as possible, put heavy demands on the design engineers, test department and the entire production team. Moreover, microwaves are reflected by metal surfaces and partially reflected by those of many other materials e.g. brick and concrete. The microcontroller has to be *intelligent* enough to recognize the signals reflected from vehicles from other interferences. Figure 1.2 shows the atmospheric attenuation in the frequency range between 10 and 300 GHz [AM88]. Among the unallocated (free) frequencies, 77 GHz has been chosen as a standard for ACC systems, as a good compromise between the attenuation caused by oxygen, water or water vapor.

1.1 Objectives of the dissertation

The aim of this dissertation is to propose, design, fabricate and characterize microwave and millimeter-wave generators based on solid state devices for automotive applications. More in detail, III-V semiconductor active devices have been considered and the attention has been focused on Gunn diodes. Two main objectives have been identified:

- Optimization of Gunn diodes for automotive application;

- Development of a novel planar Gunn diode voltage controlled oscillator.

The continuous progress of communication and automotive radar systems demands for efficient and compact oscillators with very stable frequency characteristics and low-noise levels. GaAs- and InP-based Gunn diodes have always been one of the best choices for microwave signal generation. State of the art GaAs Gunn diodes possess a graded gap injector. Starting from a deep analysis of the commercially available Gunn diodes, an optimization of the graded gap injector has been performed. Furthermore, an alternative hot electron injector, based on a resonant tunneling double barrier structure has been proposed and investigated.

Monolithic microwave integrated circuits (MMIC) represent the logical solution for cost effective mass-production mm-wave systems. In this direction, a good attempt has been done by Hwang et al. [HLK$^+$03], combining a miniaturized microstrip hairpin resonator with p-HEMTs (Pseudomorphic High Electron Mobility Transistors). Strohm et al. [SQI01] achieved similar results with SiGe HBTs (Heterostructure Bipolar Transistors) using SIMWIC (SIlicon Millimeter Wave Integrated Circuit) technology. In order to simplify the fabrication process and reduce the costs, backside treatments and via holes should be avoided. For these reasons, notwithstanding the better high frequency properties of the microstrip lines, coplanar waveguide technology (CPW) should be preferred. In our approach, a GaAs graded gap injector Gunn diode is integrated with a CPW low-pass filter for DC power supply and a planar resonator. The HF output has been realized with a simple capacitive coupler next to the Gunn diode.

1.2 Outline of the dissertation

The dissertation is organized in seven chapters. No chronological order of the various developments has been followed. Besides the **introductory chapter**, there are six chapters, which cover four main research areas: semiconductor device engineering, epitaxial growth, semiconductor processing and microwave engineering.

Chapter 2 will thoroughly examine the concept of microwave generation and, paving the way for the contents of the following chapters, the physics of the Gunn diode will be introduced as well.

Chapter 3 will present the GaAs and GaN material systems and review the wafer layer structures, describing each of them in detail and especially pointing out their strengths and weaknesses. Special attention has been paid to the device design for the hot electron injection into the L-valleys.

Chapter 4 will describe the experimental methods. It gives a brief overview of the different investigations and their functionality used within this work.

Chapter 5 will survey a comprehensive panorama of the technological processes involved in the fabrication of planar Gunn diodes and MMIC Gunn oscillators.

Chapter 6 will present the experimental results of the processed devices. The electrical measurement will be explained and compared with the literature, leaving place for sound interpretations.

Chapter 7 contains the summary of this work.

Chapter 2

Device Physics / Theoretical basis

In this chapter an overview of the basic principles behind a Gunn oscillator is presented. The phenomenon of the bulk negative conductivity concerning semiconductor with a particular band structure is explained. Relevance is given to the conditions under which oscillations, small signal amplification or only pure ohmic behaviour of the Gunn devices are achieved. A detailed description of different Gunn injectors will point out the possible device improvements. Finally the heat-sink issue is explained and a *finite elemente* thermal analysis illustrates the best geometric/material configurations for cooling Gunn devices.

2.1 Theory of the Gunn effect

2.1.1 History

The Gunn diode, also known as Transferred Electron Device (TED), is an active two-terminal solid-state device. It is unique in the sense that its voltage controlled negative differential resistance is only depending on bulk material properties rather than a junction or an interface.

The fundamental mechanism, the transferred-electron effect, was theoretically described by B. K. Ridley and T.B. Watkins in 1961 [RW61]. In 1962, Hilsum predicted the possibility of transfer-electron amplifiers and oscillators [Hil62]. In spite of Ridley-Watkins-Hilsum work, the transferred electron effect was named after an IBM researcher interested in the response of III-V semiconductors on pulsed voltages, J. B. Gunn.

In 1962, independently Gunn observed a "noisy" resistance, measured as a function of the voltage, applying 704 V on a GaAs sample. "Why did the reflected signal from a 50Ω transmission line, terminated in GaAs sample, produce several ampere of noise?" With better equipment Gunn detected regular current oscillations at about 5GHz and applied for a patent (1963). This spontaneous discovery founded the development of active-semiconductor devices to replace microwave vacuum tubes. After publishing his results [Gun63, Gun64, Dun65], many researchers started studying Gunn diodes.
H. Krömer was the first to link Gunn oscillations with the transferred-electron effect in 1964 ([Krö64]). A convincing evidence of such a correlation was delivered by A. R.

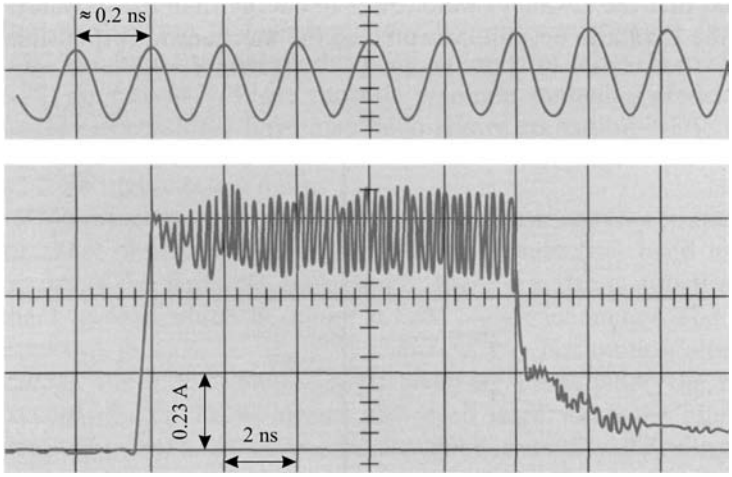

Figure 2.1: J. B. Gunn's first results applying 16 V, 10 ns voltage pulses. The device length was $2.5 \cdot 10^{-3}$cm and the corresponding oscillation frequency was 4.5 GHz [Gun63].

Hutson, A. Jayaraman and A. G. Chynoweth from Bell Labs in 1965. They showed how hydrostatic pressure could first decrease the threshold field and then suppress the current oscillations, demonstrating that the Gunn oscillations are based on the electron transfer from the low- to the high-energy valley (Γ and L).

2.1.2 The transferred-electron effect and the domain formation

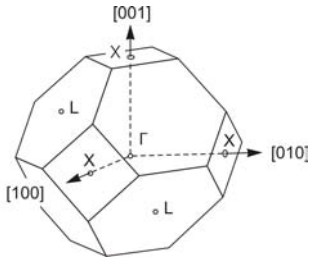

Figure 2.2: Crystallographic directions in a zinc-blende crystal.

The transferred-electron effect arises from the particular form of the band structure of some III/V compound semiconductors like GaAs, InP and GaN. As shown in Fig. 2.3, these materials are direct band-gap semiconductors, having the conduction band main minimum in the Γ-point. Two other satellite valleys[1] L and X are in the directions [111] and [100], respectively.

At low electric fields, the conduction band electrons occupy the bottom of the central valley. Applying an electric field, the electrons accelerate until they collide with imperfections of the crystal lattice. Via collisions, the electrons loose a component of their momentum, which is directed along the electric field, and some kinetic energy which raises the lattice temperature (Joule heating). As the electric field is incremented further, the mean electron energy becomes

[1] In this context, the zinc-blende structure of GaN will be considered. For a detailed description of GaN band structures, see section 3.1.2.

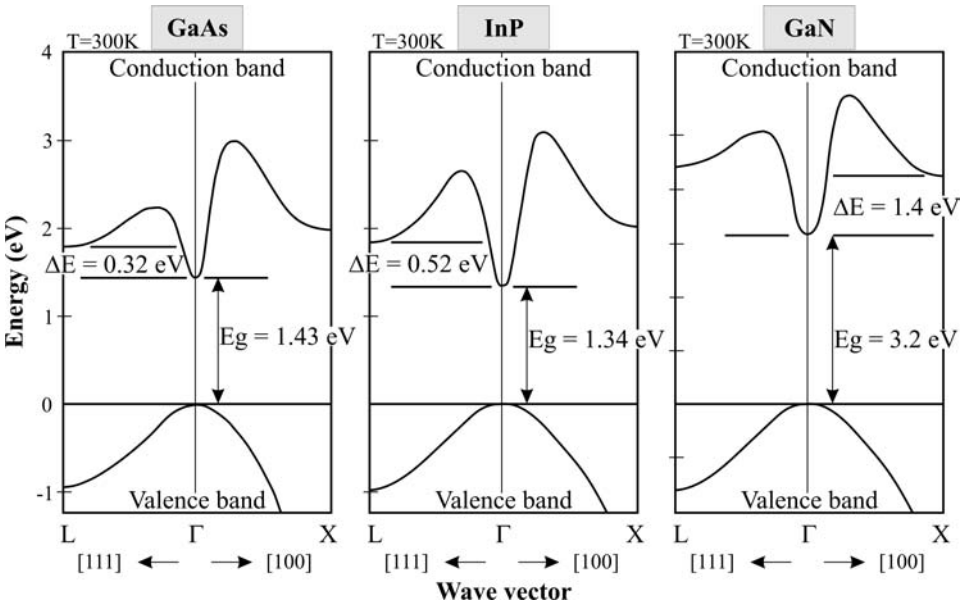

Figure 2.3: Simplified band structures of zinc-blende (cubic) GaAs, InP and GaN. [Sze98, Mor99]

higher, and higher energy states can be occupied in the conduction band. When the electron kinetic energy reaches the intervalley transfer energy $\Delta E = E_L - E_\Gamma$ (for GaAs 0.32 eV), electrons have the additional choice of occupying one of the satellite valleys (for GaAs the L-valley), as long as a suitable momentum transfer is also involved. The electron effective mass m^* is depending on the curvature of the band structure E(k) [IL03]:

$$\left(\frac{1}{m^*}\right)_{ij} = \frac{1}{\hbar^2}\frac{\partial^2 E(k)}{\partial k_i \partial k_j} \,, \tag{2.1}$$

where m^*_{ij} is effective mass tensor, $\hbar$ is the Plank constant and k is the wave vector. Assuming that the effective mass tensor components (in the direction of the principal axes) are equal to m^*, equation 2.1 can be simplified as:

$$m^* = \frac{\hbar^2}{d^2E(k)/d^2k} \,. \tag{2.2}$$

In the satellite valleys, the curvature is higher and the effective mass of the electrons is up to 6 times the Γ-valley effective mass[2]. Electrons with sufficient energy have the choice of occupying either valley. For these electrons there is a higher probability of occupying the satellite valleys which provide a relatively high density of states. In the satellite valleys, the electrons not only posses a higher effective mass, but also undergo

[2]For GaAs, electrons in L- valley have an effective mass of 0.4 m_0 and in Γ-valley of 0.068 m_0 [Hob74].

strong scattering processes [BHT72]. The combination of these two effects explains why the mobility in the side valley μ_L is up to 70 times lower compared to that in the central valley μ_Γ. If n_Γ and n_L are the electron density in the central and satellite valleys, respectively, the mean drift velocity $v_d(\mathcal{E})$ is:

$$v_d(\mathcal{E}) = \frac{\mu_\Gamma n_\Gamma + \mu_L n_L}{n_\Gamma + n_L}\,\mathcal{E}\ . \tag{2.3}$$

For higher electric fields, more electrons have the sufficient energy and the satellite valley occupation n_L will increase. Although an increasing electric field should lead to a higher electron drift velocity in each valley, the intervalley electron transfer can compensate this effect and result in a negative differential mobility. Defining η as the relative L-valley occupation

$$\eta = \frac{n_L}{n_\Gamma + n_L}, \tag{2.4}$$

and assuming that the mobility does not depend on the electric field, Eq. (2.3) leads to:

$$\frac{dv_d(\mathcal{E})}{d\mathcal{E}} = \mu_\Gamma - (\mu_\Gamma - \mu_L)\left(\eta + \frac{d\eta}{d\mathcal{E}}\mathcal{E}\right)\ . \tag{2.5}$$

In order to have a negative differential mobility, the following condition has to be fulfilled:

$$\frac{dv_d(\mathcal{E})}{d\mathcal{E}} < 0 \qquad \Rightarrow \qquad \frac{d\eta}{d\mathcal{E}} > \frac{\frac{\mu_\Gamma}{\mu_\Gamma - \mu_L} - \eta}{\mathcal{E}}\ . \tag{2.6}$$

Taking into account that $\frac{\mu_\Gamma}{\mu_\Gamma - \mu_L}$ is higher than 1 and η lower than 1, $\frac{d\eta}{d\mathcal{E}}$ must always be positive, which means that the L-valley relative occupation (η) has to increase with the electric field. Equation 2.6 confirms that the intervalley electron transfer can cause a negative differential mobility.

Figure 2.4 shows the average electron drift velocity as a function of the electric field for GaAs, InP and GaN. The drift velocity raises with the electric field up to the threshold field $\mathcal{E}_T$, hence a negative differential mobility appears and the drift velocity starts to decrease. $\mathcal{E}_T$ is extremely dependant of the material: in GaAs $\mathcal{E}_T$ is about $\sim$ 3.5 KV/cm, in InP it is $\sim$ 10 KV/cm and in GaN values between 140 KV/cm and 170 KV/cm are reported [KOB$^+$95, AWR$^+$98]

A frequency independent $v-\mathcal{E}$ characteristics can be used to describe electron transport in the presence of a time-varying electric field as long as the frequency of operation is significantly lower than the relaxation frequency f^* defined as [AP00]:

$$f^* = \frac{1}{\tau_{ER} + \tau_{ET}}\ , \tag{2.7}$$

where τ_{ER} is the energy relaxation time and τ_{ET} is the intervalley relaxation time. For GaAs and GaN, τ_{ER} is 1.5 and 0.15 ps, respectively and τ_{ET} is 7.7 and 1.2 ps [BHT72, KOB$^+$95]. Based on these values, the relaxation frequency f^* of GaAs is found to be 109 GHz. The frequency capability of GaN is superior, as indicated by the f^* of 740 GHz.

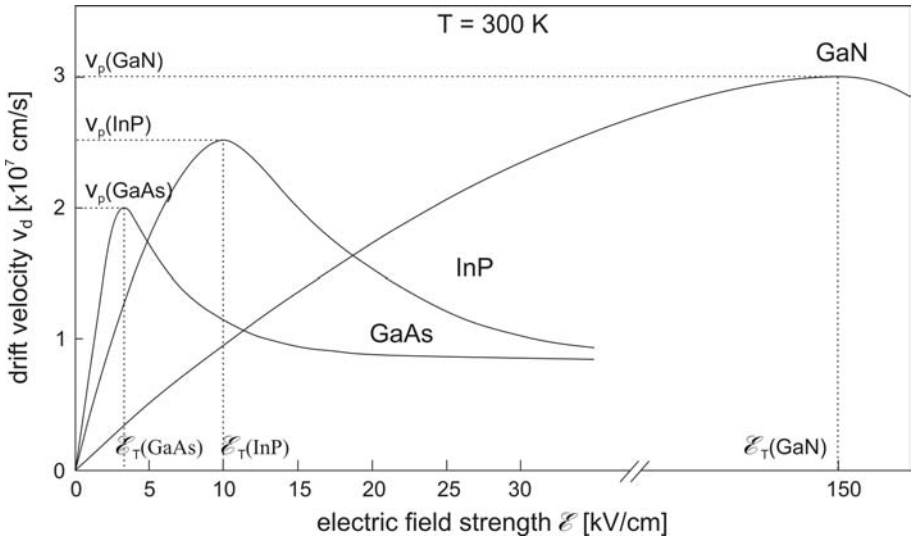

Figure 2.4: Schematic view of the average electron drift velocity v_d at 300K as a function of the electric field E for GaAs, InP and GaN [IL03, AWR+98].

In summary, the material requirements for transferred-electron negative differential mobility are [Hob74]:

- The energy gap from the satellite to central valley ΔE, must be several times larger than the thermal energy kT in order to avoid a thermal occupation of the satellite valleys at low electric fields.
- E_g, the fundamental energy gap, must be greater than ΔE: impact ionizations of electrons across E_g has to be avoided before intervalley transfer occurs.
- The effective mass in the satellite valleys must be appreciably larger than that in the lower valley.
- The electron mobility in the satellite valley must be much smaller than in the central valley.
- Transfer of electrons between the valleys must occur over a small range of electric fields.

Internal instabilities and domain formation

The negative differential mobility seen in Fig. 2.4 can be exploited directly for AC power generation, if the Gunn diode is connected to an adequate circuit. Stringent conditions are placed on its realization and further description will be given in section 2.3.3 (Low

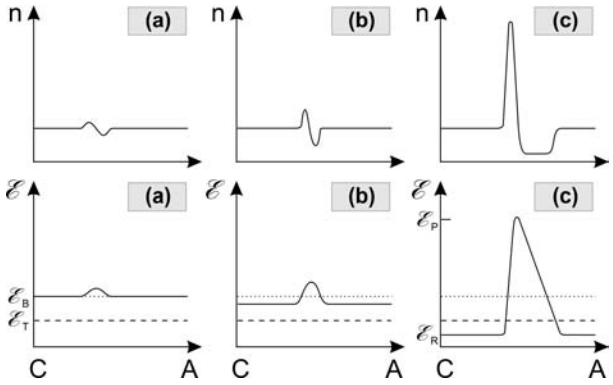

Figure 2.5: Schematic view of the growth of space-charge fluctuations to a stable dipole domain [Hob74]. C identifies the cathode (emitter) and A the anode (collector).

Space-charge Accumulation, LSA operating mode). One difficulty encountered when utilizing directly Gunn diodes as AC negative differential resistances, arises from internal instabilities.

To explain how a high-field-domain builds up in a semiconductor with a negative differential mobility, a simplified example from Hobson [Hob74] is presented. Let us consider an uniformly-doped device with an electron concentration n_0. A noise process or a defect in the doping uniformity causes a fluctuation in the electron density n. The fluctuation is an electric dipole, consisting of a depletion region and an accumulation region (Fig. 2.5(a)). The electric field relation to the non-uniformity in the space charge is given by the Poisson equation:

$$\epsilon_0 \epsilon_r \frac{\partial \mathcal{E}}{\partial x} = e\,(n - n_0) \ , \tag{2.8}$$

where ϵ_r is the relative permittivity and ϵ_0 is the vacuum permittivity.

If the mean electric field is below the threshold field $\mathcal{E}_T$, electrons with a higher electric field move faster than electrons elsewhere. The space charge accumulation fills in the depletion region and the fluctuation is damped by dielectric relaxation.

If the mean electric field is above $\mathcal{E}_T$, the drift velocity of the electrons in the region of higher field is reduced. The space-charge region swells (Fig. 2.5(b)) and, as a consequence of equation 2.8, the electric field raises in the region of the domain. In the rest of the device, the electric field sinks because the total voltage drop must remain constant.

In figure 2.5(c), the domain has reached a stable condition. The level of the electric field outside the domain $\mathcal{E}_R$ is under the threshold and the electric field in the domain reaches $\mathcal{E}_P$. $\mathcal{E}_P$ and $\mathcal{E}_R$ correspond to the same drift velocity. Inside the domain, electrons travel as fast as outside the domain and the space-charge region stops growing. When a domain is stable, no other domain can build up while $\mathcal{E}_R$ is below the threshold.

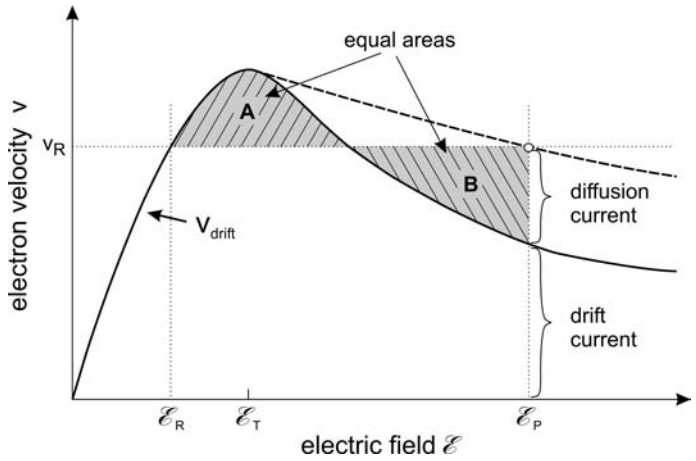

Figure 2.6: Illustration of the equal area relationship between $\mathcal{E}_R$ and $\mathcal{E}_p$ [But65, BFH66].

2.1.3 Domain Dynamics

In this section, the behaviour of stable domains will be examined. The stable space charge profile, or domain, drifts at a constant velocity through the device. The electric field in the different parts of this nonlinear entity is strictly related to the domain growth and decay and to the corresponding stability. The analysis of the domain form requires non linear solutions of the Poisson equation and the current continuity equation taking the $v - \mathcal{E}$ characteristics into account. An analytical solution of the problem comes from Butcher et al. [But65, BFH66]. Their most important results can be summarized in three items:

- If the diffusion parameter D is assumed constant and independent of the electric field, the domains travel with the same velocity as the electrons outside the domains (v_R).
- The peak electric field, $\mathcal{E}_p$ and v_R are related with the so-called *dynamic characteristic* (Fig. 2.6).
- The dynamic characteristic can be constructed geometrically from the $v - \mathcal{E}$ characteristics ($F_{v-\mathcal{E}}$) as the locus of points ($\mathcal{E}_p$,v_R), which satisfies the condition:

$$Area\left(\mathcal{A}(\mathcal{E}_p, v_R)\right) = Area\left(\mathcal{B}(\mathcal{E}_p, v_R)\right) \ , \tag{2.9}$$

where the region $\mathcal{A}$ is defined from

$$\mathcal{A}(\mathcal{E}_p, v_R) = \{(\mathcal{E}, v) \ : \ v > v_R \ \cap \ v < F_{v-\mathcal{E}}(\mathcal{E})\} \ ,$$

and the region $\mathcal{B}$ is defined from

$$\mathcal{B}(\mathcal{E}_p, v_R) = \{(\mathcal{E}, v) \ : \ v < v_R \ \cap \ v > F_{v-\mathcal{E}}(\mathcal{E}) \ \cap \ \mathcal{E} < \mathcal{E}_p \ \cap \ \mathcal{E} > \mathcal{E}_T\} \ .$$

The conserved[3] current density j is given by:

$$j = env_d(\mathcal{E}) \; + \; \epsilon_0\epsilon_r\frac{\partial\mathcal{E}}{\partial t} \; - \; eD\frac{\partial n}{\partial x} \; . \tag{2.10}$$

where the three terms represent, respectively, the drift, displacement and diffusion component. Equation (2.10) is simplified outside the domain, where n and $\mathcal{E}$ are independent of the position. The current is carried entirely as drift current. Inside the domain, all three terms of Eq. (2.10) play a role. The electric field gradients move and determine the displacement current to flow. At the peak field of the domain, there is no displacement current because $\partial E/\partial x = 0$, but the electron density gradient results in a diffusion current. Figure 2.6 illustrates the relative values between diffusion and drift currents. For the depletion region of the domain, the current is predominantly carried by a displacement current, while in the accumulation region there is a large drift current opposed by displacement and diffusion currents.

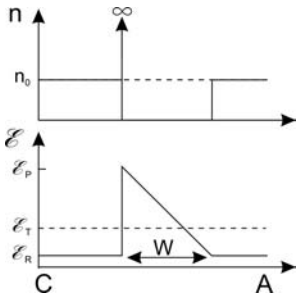

Figure 2.7: Domain profile in the limit condition of zero diffusion.

Further on, the form of a stable high field domain will be examined, neglecting the diffusion and it will be shown that the domains travel at the same velocity (v_{domain}) as the electrons outside the domain(v_R). If the diffusion coefficient D is assumed to be zero, the electron density of the domain must be zero (depletion region) or ∞ (accumulation region) [Hob74]. In this simple case, the electric field in the domain is triangular, as shown in Fig. 2.7. Outside the domain, nothing changes and the carrier concentration remains n_0. The current density outside the domain is

$$j = n_0 e v_R \; . \tag{2.11}$$

Inside the domain, in the case of a fully depleted region, the current density is written:

$$j^* = \epsilon_0\epsilon_r\frac{\partial\mathcal{E}}{\partial t} = -\epsilon_0\epsilon_r\frac{\partial\mathcal{E}}{\partial x}v_{domain} \; . \tag{2.12}$$

The Poisson equation requires:

$$\epsilon_0\epsilon_r\frac{\partial\mathcal{E}}{\partial x} = -n_0 e \; , \tag{2.13}$$

therefore

$$j^* = n_0 e v_{domain} \; . \tag{2.14}$$

By current continuity ($j^* = j$), Eq. (2.11) and Eq. (2.14) require that

$$v_R = v_{domain} \; . \tag{2.15}$$

In the case of a fully depleted domain, the result is not influenced by the electric field dependence of the diffusion constant D.

[3]Considering $\frac{\partial(j_{drift}+j_{diff})}{\partial x} = -\frac{\partial\rho}{\partial t} = -\epsilon_0\epsilon_r\frac{\partial}{\partial t}\frac{\partial\mathcal{E}}{\partial x} \Rightarrow \frac{\partial j}{\partial x}$ of (2.10) is 0 and the current is conserved.

The next problem consists in finding the stable value of the outside field $\mathcal{E}_R$ in connection with the applied terminal bias U_B. If L is the device length, w the width of the domain and U_D the domain voltage, U_B is given by:

$$U_B = U_D + \mathcal{E}_R(L - w) \; . \tag{2.16}$$

The domain length can be neglected, because it is small in comparison with the device length ($w << L$), therefore:

$$U_B = U_D + \mathcal{E}_R L \; . \tag{2.17}$$

U_D, in the case of the triangular domain (with the diffusion coefficient D=0) is given by:

$$U_D = \frac{w(\mathcal{E}_p - \mathcal{E}_R)}{2} \; . \tag{2.18}$$

From the Poisson equation

$$w = \frac{\epsilon_0 \epsilon_r (\mathcal{E}_p - \mathcal{E}_R)}{n_0 e} \; , \tag{2.19}$$

resulting for U_D the expression:

$$U_D = \frac{\epsilon_0 \epsilon_r (\mathcal{E}_p - \mathcal{E}_R)^2}{2 n_0 e} \; . \tag{2.20}$$

Equation (2.20), the electrical boundary condition (Eq. (2.17)) and the equal area rule between $\mathcal{E}_p$ and $\mathcal{E}_R$ determine the domain behaviour for a given terminal bias U_B. Figure 2.8 outlines the relationship between the domain voltage and the electric field outside the domain. In the diagram, the three *load lines* correspond to three different terminal biases U_B. The intercepts are the possible solutions for a given doping concentration n_o, device length L. The electrical field $\mathcal{E}_R$ is displayed versus the domain voltage U_D. Three configurations are possible:

Load line 1. The average electric field U_B/L (the intersection of the load-line with the $\mathcal{E}_R$-axis) is higher than threshold field $\mathcal{E}_T$. Under this condition, only one solution is possible and the solution is stable.

Load line 2. The average electric field U_B/L is equal to $\mathcal{E}_S = V_S/L$. The value V_S is called sustaining voltage. Under this characteristic voltage the domain will be extinguished in flight. At the sustaining voltage, the load-line is tangent to the $U_D - \mathcal{E}_R$ curve. V_S is extremely important concerning the analysis of the oscillation modes.

Load line 3. The average electric field U_B/L is lower than E_T and higher than $\mathcal{E}_S = V_S/L$. If the value U_B/L has been higher than $\mathcal{E}_T$ during the domain nucleation, two solutions are possible. The higher intercept is stable, the lower one unstable. Keeping in mind that the load line condition (Eq. (2.17)) must be satisfied all the time and that the $U_D - \mathcal{E}_R$ curve refers only to a steady state domain, the instability of the lower intercept can be explained with a simple example. Let us consider a

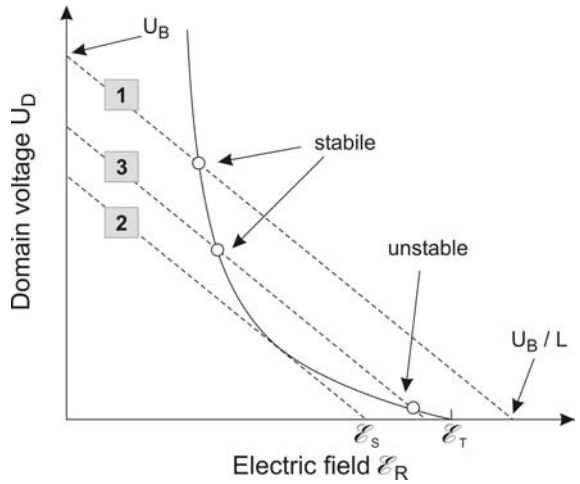

Figure 2.8: Diagram of the relationship between the domain voltage U_D and the electric field outside the domain $\mathcal{E}_R$ imposed by the space charge dynamics (solid-line). At the same time, the device must satisfy the boundary conditions contained in the load-line (dashed line). Three possible configurations for three external biases U_B are considered.

small noise fluctuation: a small increase of U_D causes $\mathcal{E}_R$ to decrease (Eq. (2.17)). The new state is not anymore on the $U_D - \mathcal{E}_R$ curve, but higher. In the new state, the electrons outside the domains move faster than the domain. This means that both the accumulation and depletion regions of the domain will grow causing a further increase of U_D (Poisson's equation). In the next state, the working point will move again higher on the load-line and the readjustment will continue up to the higher stable intercept.

2.1.4 The small signal behaviour of a transferred-electron device

In this section, the stability with respect to small current or voltage perturbations of the steady-state solutions will be considered [MC66, Hei71]. The analysis starts from the Poisson's and current equations:

$$\frac{\partial \mathcal{E}(x)}{\partial x} = \frac{e}{\epsilon_r \epsilon_0} \left(n(x) - n_0(x)\right) , \tag{2.21}$$

$$j = e\, n(x)\, v_d(\mathcal{E}) + \epsilon_r \epsilon_0 \frac{\partial \mathcal{E}}{\partial t} , \tag{2.22}$$

and from two assumptions about the fluctuations:

- the fluctuations are periodic in time;
- the fluctuations are small in comparison to the corresponding equilibrium values $\mathcal{E}_0$, j_0 and v_0.

The so defined fluctuations are governed by:

$$\mathcal{E}(x,t) = E_0 + \Delta\mathcal{E}(x)\, e^{i\omega t}\,, \tag{2.23}$$
$$j(t) = j_0 + \Delta j\, e^{i\omega t}\,, \tag{2.24}$$
$$v(x,t) = v_0 + \mu_0 \Delta\mathcal{E}(x)\, e^{i\omega t}\,. \tag{2.25}$$

From Eq. (2.21) and Eq. (2.23) it follows:

$$\frac{d\Delta\mathcal{E}}{dx}\, e^{i\omega t} = \frac{e}{\epsilon_r\epsilon_0}\,(n - n_0)\,, \tag{2.26}$$

and

$$n = n_0 + \frac{\epsilon_r\epsilon_0}{e}\,\frac{d\Delta\mathcal{E}}{dx}\, e^{i\omega t}\,. \tag{2.27}$$

Equations (2.23), (2.24) and (2.25) can be substituted in the current equation (2.22) and n can be eliminated with the help of Eq. (2.27), obtaining:

$$j_0 + \Delta j\, e^{i\omega t} = e\left(n_0 + \frac{\epsilon_r\epsilon_0}{e}\,\frac{d\Delta\mathcal{E}}{dx}\, e^{i\omega t}\right)\left(v_0 + \mu_0\, \Delta\mathcal{E}\, e^{i\omega t}\right) + i\,\epsilon_r\epsilon_0\Delta\mathcal{E}\,\omega\, e^{i\omega t}. \tag{2.28}$$

After some simplifications:

$$\Delta j = (i\omega\epsilon_r\epsilon_0 + e\mu_0 n_0)\,\Delta\mathcal{E} + v_0\epsilon_r\epsilon_0\frac{d\Delta\mathcal{E}}{dx} + \mu_0\epsilon_r\epsilon_0\Delta\mathcal{E}\,\frac{d\Delta\mathcal{E}}{dx}\, e^{i\omega t}. \tag{2.29}$$

The last term in Eq. (2.29) can be neglected, because it is of the same order as $\mathcal{O}((\Delta\mathcal{E})^2)$ and $\Delta\mathcal{E}$ was assumed to be small.

$$\Delta j = (i\omega\epsilon_r\epsilon_0 + e\mu_0 n_0)\,\Delta\mathcal{E} + v_0\epsilon_r\epsilon_0\frac{d\Delta\mathcal{E}}{dx}\,. \tag{2.30}$$

If the doping concentration in the active region is uniform, n_0 is not depending on x and Eq. (2.30) results in a linear differential equation with constant coefficients. Choosing $\Delta\mathcal{E}(x=0) = 0$ as boundary condition, the general solution is:

$$\Delta\mathcal{E}(x) = \frac{\Delta j}{\epsilon_r\epsilon_0 v_0\gamma}\left(1 - e^{-\gamma x}\right)\,, \tag{2.31}$$

where

$$\gamma = \frac{e n_0\mu_0}{\epsilon_r\epsilon_0 v_0} + i\frac{\omega}{v_0}\,. \tag{2.32}$$

Finally, from Eq. (2.23) and Eq. (2.31), we have:

$$\mathcal{E}(x,t) = \mathcal{E}_0 + \frac{\Delta j}{\epsilon_r\epsilon_0 v_0\gamma}e^{i\omega t} - \frac{\Delta j}{\epsilon_r\epsilon_0 v_0\gamma}e^{-\gamma x}e^{i\omega t}\,. \tag{2.33}$$

The second term on the right side of Eq. (2.33) describes an uniform field oscillation, independent of x; this governs in the LSA operating mode (see section 2.3.3). The last

term represents a wave propagating in the x direction with the same phase and group velocity v_0, because using (2.32) we obtain:

$$v_{phase} \equiv \frac{\omega}{Im[\gamma]} = v_0 \ , \ v_{group} \equiv \frac{\partial \omega}{\partial (Im[\gamma])} = v_0 \ . \tag{2.34}$$

This variable was defined as the drift velocity, at which the electrons move through the crystal under the influence of the external electrical field. The modulation $\Delta\mathcal{E}\, e^{i\omega t}$ of the electron density creates a space charge wave, which propagates with the electron drift velocity v_0.
If $\mu_0 > 0$, then $Re[\gamma] > 0$ and the wave is damped; if $\mu_0 < 0$, then $Re[\gamma] < 0$ and the wave amplitude increases. The sign of μ_0 depends first of all on the electric field in relation to the threshold field $\mathcal{E}_T$, as already explained in section 2.1.2 and shown in Fig. 2.4.
The device is stable with respect to small perturbations if the real part of the impedance Z is positive. Z is defined as:

$$Z = \frac{\Delta U}{A\ \Delta j} = \frac{\int_0^L \Delta E(x)\ dx}{Ae\ \Delta j} \ , \tag{2.35}$$

where A is the cross sectional area of the Gunn device. With Eq. (2.31) it follows:

$$Z(\omega) \ = \ \frac{1}{A\epsilon_r\epsilon_0 v_0}\ \frac{e^{-\gamma L} + \gamma L - 1}{\gamma^2} \ . \tag{2.36}$$

As demonstrated by McCumber and Chynoweth [MC66], Eq. (2.36) is well behaved for all finite ω and $Z(\omega)$ has no singularities. This means that the device described by Eq. (2.36) is always stable when it operates under constant current conditions.
In order to determine the stability under constant voltage conditions, the poles of the admittance $Y(\omega) = 1/Z(\omega)$ or the zeros of $Z(\omega)$ must be investigated. Setting $s = \gamma L$, the zeros of Eq. (2.36) correspond to the zeros $s_n = \phi_n + i\ \eta_n$ (n=0,1,2..) of

$$f(s) = e^{-s} + s - 1 = 0 \ . \tag{2.37}$$

It is necessary to divide f(s) into the real and imaginary part:

$$f(s_n) \ = \ e^{-\phi_n}(\cos(\eta_n) + i \sin(\eta_n)) + \phi_n + i\ \eta_n - 1 \ , \tag{2.38}$$

$$Re[f(s_n)] \ = \ e^{-\phi_n}\cos(\eta_n) + \phi_n - 1 \ , \tag{2.39}$$

$$Im[f(s_n)] \ = \ e^{-\phi_n}\sin(\eta_n) + \eta_n \ . \tag{2.40}$$

- The first zero is $s_0 = 0$: this means $\gamma L = 0$. Either the length of the device is zero (L=0) or the frequency and the mobilities are zero ($\gamma = 0$).
  $s_0 = 0$ is not a physically relevant zero of $Z(\omega)$.

- The other zeros s_n (n=1,2,3..) satisfy the conditions:

$$\eta_n = \frac{(4n+1)\pi}{2} - \arcsin\left[(1-\phi_n)e^{\phi_n}\right] , \tag{2.41}$$

$$\phi_n = -\frac{1}{2}\ln\left[\eta_n^2 + (1-\phi_n^2)\right] , \tag{2.42}$$

$$\lim_{n\to\infty}(\eta_n) = \frac{(4n+1)\pi}{2} , \tag{2.43}$$

$$\lim_{n\to\infty}(\phi_n) = -ln\left[\frac{(4n+1)\pi}{2}\right] . \tag{2.44}$$

The second zero is for $\phi_1 = -2.09$.

If $|\phi_1| < 2.09$, then the Re[Z] is positive and the device is stable. From Eq. (2.32), it results:

$$n_0 L \ < \ 2.09\ \frac{\epsilon_0 \epsilon_r v_0}{e|\mu_0|} . \tag{2.45}$$

Choosing the parameters for GaAs ($\epsilon_r = 12.9$, $v_0 = 10^7\ cm^2/s$ and $\mu_0 = 2500\ cm^2/Vs$), we have:

$$n_0 L \ < \ 6\ 10^{11}\ cm^{-2} . \tag{2.46}$$

Considering that the mobility depends on the doping level, the consistent stability condition for GaAs is given by:

$$n_0 L \ < \ 10^{12}\ cm^{-2} . \tag{2.47}$$

It can be concluded that, at room temperature, GaAs devices will always be stable with steady state properties, if the product $n_0 L$ is under the critical value. This result applies only for a small signal approach; nevertheless, with appropriate intensity of the electric field (i.e. $\gg \mathcal{E}_T$), samples with $n_0 L$ lower than the critical value provide amplification for microwave signals (i.e. $Re[\gamma] < 0$).

2.2 Gunn diode with hot electron injectors

Hot electron injection is the process of raising the electron energy to the level of the L band before it enters the drift zone. Without a hot electron injector, the electrons will remain in the Γ-valley until they gain enough energy to transfer to the upper valleys. The distance required to gain such an energy depends on the electric field level and, on a minor scale, on the device temperature. The region near the emitter, where most electrons reside in the Γ-valley, is called *dead-zone*. Gunn domains can build only outside the dead-zone. The dead-zone not only narrows the active region (up to 17% in a 1.5 μm GaAs Gunn device [NDS+89]), but introduces an undesirable positive serial resistance reducing the r.f. power and the efficiency of the device. Moreover, the dead zone is not constant and should be considered as an aleatory process having very bad influences on the device noise properties.

The solution to the described problems is to embed a hot electron injector in the emitter region just before the Gunn diode active region. An efficient injector leads to the following advantages:

- improved temperature stability of power and frequency,
- improved oscillator turn on characteristic, especially at low temperatures,
- increased efficiency (lower voltage drop on the injector),
- low phase noise.

The Schottky, graded gap and resonant tunneling injectors represent different approaches to fulfill these objectives.

2.2.1 Metal semiconductor Schottky contact injector

To understand how the Schottky contact injector works, it is useful to introduce briefly the physics behind a metal-semiconductor contact.

There are two kinds of metal-semiconductor contacts: ohmic and Schottky. An ohmic contact is a metal or silicide contact to a semiconductor with a small interfacial resistance and a linear I-V characteristics. In this case, the work function of the semiconductor must be greater than the work function of the metal ($\phi_s > \phi_m$) [Nea97]. The described condition is valid only for ideal ohmic contacts (e.g. indium based compounds). Typically, semiconductor engineers consider ohmic contacts also Schottky contacts with a very thin potential barrier and a linear I-V characteristic.
In a Schottky contact, the work function of the semiconductor must be smaller than the work function of the metal ($\phi_\mathrm{s} < \phi_\mathrm{m}$). The ideal energy-band diagram for a particular metal and n-type semiconductor before making the contact is shown in Fig. 2.9(a), where ϕ_m is the metal work function, ϕ_s is the semiconductor work function and χ is the semiconductor electron affinity. The vacuum level is used as a reference level. Before contacting, the Fermi level in the metal is above the Fermi level in the semiconductor. After contacting, in thermal equilibrium, the Fermi level has to be constant through the whole system and electrons from the semiconductor flow into the lower energy states in

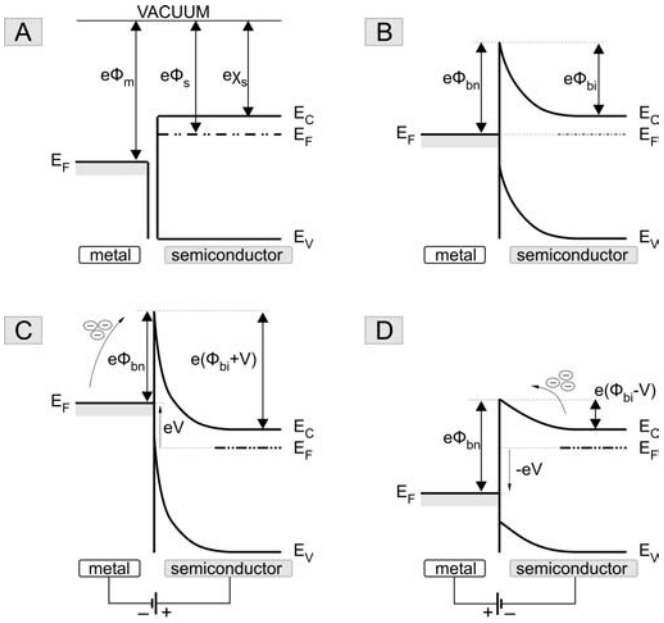

Figure 2.9: Energy-band diagrams for Schottky contact on n-semiconductor: (a) before contacting, (b) after contacting in equilibrium, (c) under reverse bias and (d) direct bias.

the metal. Positively charged donor atoms remain in the semiconductor, creating a space charge region (Fig. 2.9(b)). The potential barrier seen by electrons in the metal trying to move into the semiconductor is known as "Schottky barrier". Assuming an ideal interface, without Fermi pinning, the barrier height $\phi_{\rm bn}$ is given by:

$$\phi_{bn} = (\phi_m - \chi) \ . \tag{2.48}$$

On the semiconductor side, $V_{\rm bi}$ is the built-in potential barrier seen by electrons in the conduction band trying to move into the metal and is given by:

$$V_{bi} = (\phi_{bn} - \phi_n) \ , \tag{2.49}$$

where ϕ_n is the potential difference between the minimum of the conduction band in the semiconductor (E_c) and the Fermi level (E_F):

$$\phi_n \ = \ \frac{E_c - E_F}{e} \ , \tag{2.50}$$

where e is the electron charge.
In the reverse bias condition, where a positive voltage V is applied to the semiconductor with respect to the metal (Fig. 2.9(c)), the semiconductor-to-metal barrier increases, while $\phi_{\rm bn}$ remains constant in the idealized case. In the forward bias condition, a negative

voltage is applied to the semiconductor with respect to the metal (Fig. 2.9(d)) and the semiconductor-to-metal barrier decreases, while ϕ_{bn} still remains constant. In this case, electrons can move easily from the semiconductor into the metal.
Solving the Poisson's equation, it is possible to calculate the electric field present in the space charge region in the metal. The depletion layer width W of region is given by:

$$W = \sqrt{\frac{2\epsilon_s(V_{bi} + V - \frac{kT}{e})}{eN_d}} \ , \tag{2.51}$$

where N_d is the donor concentration, ϵ_s is the dielectric constant of the semiconductor, k is the Boltzmann constant and T is the temperature in K. The term kT/e arises from the contribution of the majority-carrier distribution tail [Sze81].
Three basic transport processes through the Schottky barrier can be identified:

- thermionic emission of electrons over the potential barrier (dominant process for moderate doped semiconductor $N_d < 10^{-17} cm^{-3}$),
- tunneling of electrons through the barrier (quantum-mechanical process important for heavily doped semiconductors and responsible for most ohmic contacts),
- recombination in the depletion region.

The ideal expression of the J-V characteristics taking into account the thermionic emission and the diffusion is [Sze81]:

$$J = J_s(e^{\frac{qV}{kT}} - 1) \ . \tag{2.52}$$

The saturation current density, J_s for the thermionic emission case is:

$$J_s = A^* T^2 e^{-\frac{q\phi_{bn}}{kT}} \ . \tag{2.53}$$

where A^* is the effective Richardson constant. Tunneling, recombination and injection cause deviations from the ideal behaviour. Introducing the serial resistance[4] R_s and the ideality factor n leads to

$$J = J_s(e^{\frac{qV - R_s J}{nkT}} - 1) \ . \tag{2.54}$$

Looking back at the first Gunn diodes, a Schottky barrier was always present. The quality of the ohmic contacts was extremely poor, leading to low uniformity, low reproducibility and high parasitic voltage drops.
Even if, in the last 30 years, amazing improvements have been achieved in metal-semiconductor contacts, an unsolvable problem remains for Schottky hot electron injectors: Fermi level pinning. The Schottky barrier on GaAs has a height of about 0.65 eV, not depending of the metal because of the Fermi level pinning. The barrier cannot be engineered properly and 0.65 eV is not the optimum barrier height for an efficient electron transfer from Γ to L valley. In a similar way, Fermi level pinning is present also in other III/V semiconductors, limiting the applications of the Schottky barrier injector Gunn diodes drastically.

[4] R_s is a resistance per unit area $[\Omega/cm^2]$

2.2.2 Graded gap injector

The idea of the graded gap AlGaAs barrier comes from the need of a potential barrier which can be optimized, changing its height, width and shape [CBK+88, NDS+89, GWCE88]. As seen in section 2.2.1, these parameters are difficult to control in the case of the metal-semiconductor Schottky barrier, especially concerning the reproducibility.

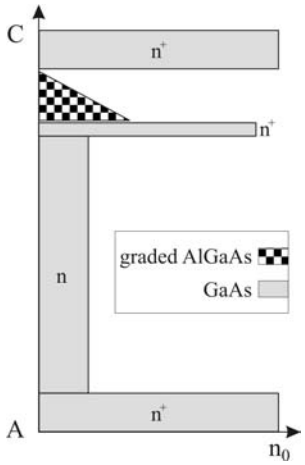

Figure 2.10: Principle schema of a Gunn diode with a graded AlGaAs injector. C identifies the cathode (emitter) and A the anode (collector).

The epitaxial process offers an extremely high accuracy and tuning possibilities for the injector fabrication. The material system $Al_xGa_{1-x}As$ maintain nearly the same lattice constants, with the change of the Al concentration. Grading the Al concentration, it is possible to obtain a potential barrier. The AlGaAs barrier has to be nominally undoped and the Al concentration starts at 0% (on the cathode/emitter side) and increases linearly up to the maximal concentration (in the anode/collector direction). The height of the barrier has to be designed considering the energy needed by electrons for the Γ to L transfer.
Establishing the width of the graded AlGaAs barrier, two factors have to be considered. The barrier has to be wide enough to prevent electrons to tunnel at lower energy levels; only the electrons passing over the barrier have enough energy for the intervalley transfer. On the other hand, a wide undoped AlGaAs barrier results in a too high serial resistance. The second part of the injector is a thin n^+ doped layer of GaAs, connecting the AlGaAs barrier to the Gunn active region. A complete view of the graded gap injector is illustrated in Fig. 2.10.

In order to correctly understand the behaviour of the graded gap injector Gunn diodes, complex simulations are required. Monte Carlo computations have demonstrated that the graded AlGaAs barrier, followed by a thin highly doped layer, increases the intervalley electron transfer and reduces the *dead-zone* thereby improving noise performance, temperature stability and power conversion efficiency [LR90]. A much simpler approach for the simulation of the DC behaviour considers the Gunn diode composed of two elements in series: the graded gap injector and the diode active region plus the contact resistance. For low bias (voltages much lower than the threshold), the Gunn active region plus the contact resistance have a linear characteristics and the graded gap injector can be modelled like a Schottky barrier. Under these assumptions, a load-line model is defined like in Fig. 2.11 where the voltage drop on the diode U_T is the sum of the single voltage drops, on the graded gap injector (U_I) and on the ohmic active region (U_R).

The following function describes the graded gap injector with a simple exponential law.

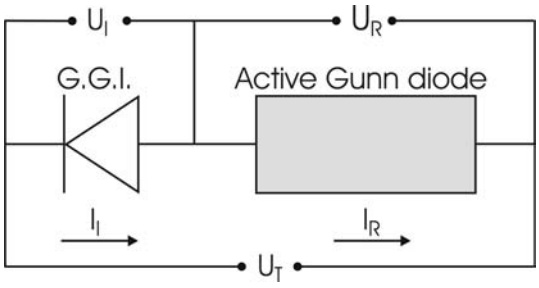

Figure 2.11: DC electrical model of a graded gap injector Gunn diode.

Two important parameters are introduced: the saturation current I_s (Eq. (2.53)) and the constant c_1, which is a measure of the tunneling current.

$$I_I = I_s e^{c_1 U_I} \ . \tag{2.55}$$

Then, considering the device area A and the active region length l, the current I_R through the active region can be written as:

$$I_R = -\frac{(U_T - U_I)A}{l\rho} \ . \tag{2.56}$$

The resistivity ρ can be expressed as:

$$\rho = \frac{1}{ne\mu} \ , \tag{2.57}$$

where n is the electron concentration, μ is the mobility and e is the electron charge. Introducing the Lambert transcendental function W(x) and defining the diode current as $I_T = I_I(U_I) = I_R(U_I)$, it follows:

$$U_I = \frac{-W(\frac{c_1 I_s l e^{c_1 U_T}}{n\mu e A}) + c_1 U_T}{c_1} \ , \tag{2.58}$$

$$W(x) = \frac{x}{e^{W(x)}} \ . \tag{2.59}$$

Substituting U_I in Eq. (2.55), the diode current I_T is obtained as function of the diode total bias U_T

$$I_T = I_s e^{-W(\frac{c_1 I_s l e^{c_1 U_T}}{n\mu e A}) + c_1 U_T} . \tag{2.60}$$

As shown in section 6.1.3, Eq. (2.60) matches the I-V behaviour of graded gap Gunn diode very well. The proposed model is fitted to the measured I-V characteristic in the reverse current direction for different temperatures. Moreover, taking into account the temperature dependence of I_s, the effective barrier height can be estimated.

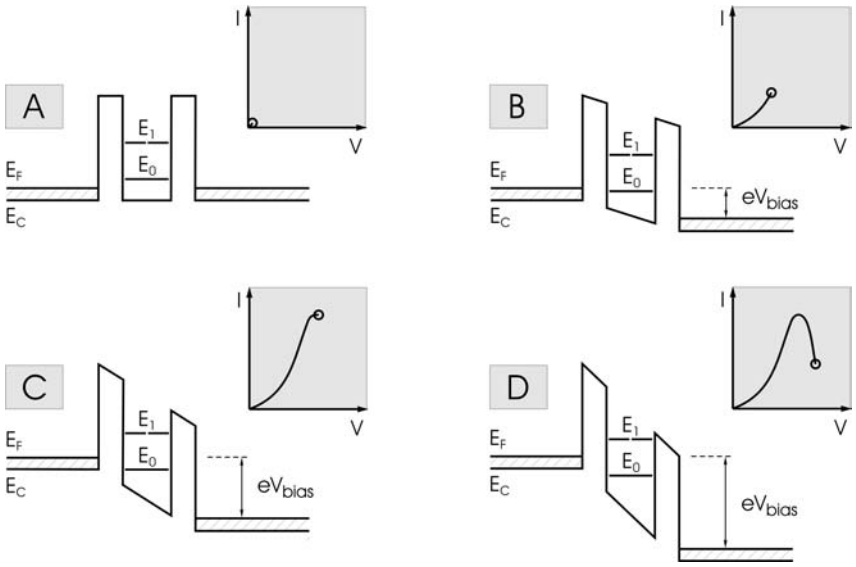

Figure 2.12: Bias-dependent band diagrams and current voltage characteristics for an RTD at 4 bias points: A, B, C, D.

2.2.3 Resonant tunneling injector

In section 2.2.2, the state of the art for hot electron injection in Gunn diodes has been discussed . This raises the question if a graded gap injector can be further improved. The solution might be in using the resonant tunneling effect, one of the most exciting quantum mechanical phenomena in semiconductor physics [CET74, TE73].

Resonant tunneling diodes (RTDs) are based on a double potential barrier structure like AlAs/GaAs/AlAs. The structure is designed such that resonant bound states are present in the quantum well. Electrons can tunnel through the double-barrier if their transversal energy is equal to the energy of one of the quasi bound states in the quantum well. The I-V curve of a double barrier structure can be in principle understood with the help of Fig. 2.12. Close to zero electrical bias, a small fraction of the electrons has an energy equal with the energy of the first quasi bound state (Fig. 2.12A). As the voltage increases, the resonant states are shifted down towards the Fermi level on the emitter side and a greater number of electrons can tunnel, contributing to the current (Fig. 2.12B). At a certain voltage, the conduction band level of the emitter side is aligned to the quantum well resonant level and a maximum appears in the current (Fig. 2.12C). Beyond this voltage, the resonant level drops below the emitter conduction band edge, resulting in a sudden drop of the current (Fig. 2.12D). For higher voltages, the current rises again, because of the combination of two effects: the next resonant level lowers and a thermionic emission occurs over the barrier.

The negative differential resistance of the RTD (Fig. 2.12D) has been exploited for microwave analog devices like oscillators [BPBP93] and mixers [MMP+91] and for

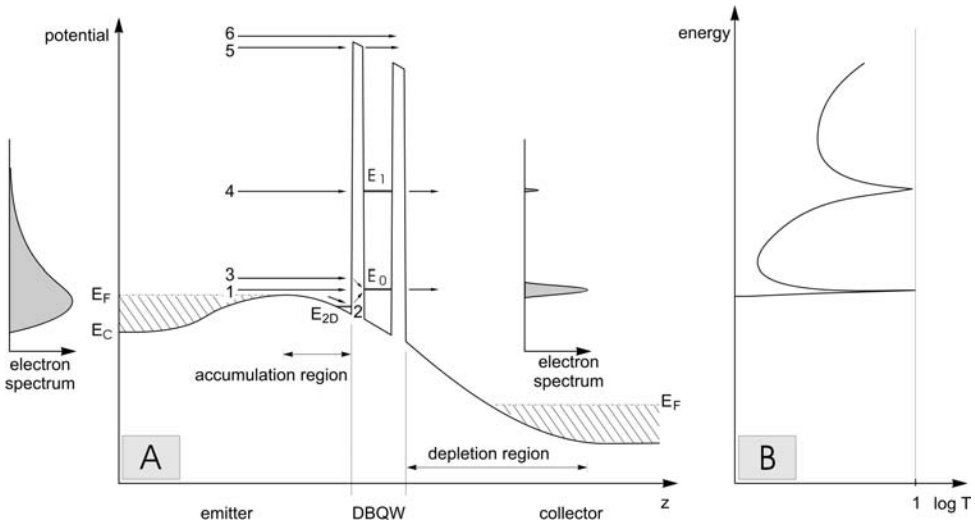

Figure 2.13: Band diagram of a typical GaAs/AlGas heterostructure (A) with the corresponding transmission probability T (B). The electron distribution before and after the double barrier points out the excellent energy filter capabilities of the device.

ultrafast digital devices like monostable-bistable transition logic elements (MOBILE) [MM93, SMI+01, Was03].

For RTD serving as a hot electron injector, no negative differential resistance is needed and only the small bias voltage region of the I-V curve should be considered. As a means to better understand the resonant tunneling injection, the different transport processes through a double barrier are examined [SHMS98]. In Fig. 2.13(A), the different transport paths are illustrated. The electrons with exactly the resonant energy E_0 tunnel through the double barrier with the probability of ~ 1 (process 1). In the emitter part, the electron accumulation in front of the first barrier bends the conduction band and causes the formation of a triangular potential well with discrete two-dimensional energy levels. Electrons can tunnel from the potential well through the double barrier with the help of a phonon (process 2). In a similar way, electrons undergoing the process 3, whose energy is a little higher than the resonant energy E_0, can tunnel due to an interaction with a phonon. In process 4, like in process 1, electrons have exactly the energy of the resonant level E_1. In process 5-6, high energy electrons cross the device, tunneling through only one barrier or overcoming the whole heterostructure (thermionic emission). Because of the required high energy, electrons involved in process 5 and 6 are relatively few.

The electron transmission probability T is a result of the different transport processes. In a first approximation, T can be expressed as a Lorentzian function of energy E with a

half width Γ_n [Dav98]:

$$T(E) = T_{max}\frac{\frac{1}{4}\Gamma_n^2}{\frac{1}{4}\Gamma_n^2 + (E - E_n)^2}\,, \tag{2.61}$$

$$T_{max} = \frac{4T_1T_2}{(T_1 + T_2)^2}\,, \tag{2.62}$$

$$\Gamma_n = \frac{\hbar}{\tau_n}\,, \tag{2.63}$$

where T_1 and T_2 represent the transmission probability of the single barriers, Γ_n the full energetic width at half maximum of the transmission probability T and τ_n is the electron lifetime in the energy state E_n.
The simulated T versus the electron energy is plotted in Fig. 2.13(B). It can be noticed a tunneling probability of one for the quantized energy states. The width of the resonance is exponentially dependent on the thickness of the barrier. Direct effects of the resonance can be seen in the electron distribution behind the double barrier. This confirms that this device can be used for building a very precise energy filter.

2.3 Gunn diode based oscillators

2.3.1 Theory of two-port networks

All electromagnetic processes can ultimately be explained by Maxwell's four basic equations:

$$\nabla \cdot \vec{D} = \rho_{\text{free}} , \tag{2.64}$$

$$\nabla \cdot \vec{B} = 0 , \tag{2.65}$$

$$\nabla \times \vec{E} = -\frac{\partial \vec{B}}{\partial t} , \tag{2.66}$$

$$\nabla \times \vec{H} = \vec{J}_{\text{free}} + \frac{\partial \vec{D}}{\partial t} . \tag{2.67}$$

However, it is not always possible or convenient to directly use these equations. Solving them can be quite difficult. Efficient design requires the use of approximations such as lumped and distributed models.

Linear or nonlinear networks, operating with signals small enough for the networks to respond in a linear manner, can be completely characterized by parameters measured at the network terminals (ports), no matter of the network contents. Once the parameters of a network are determined, its behaviour in any external environment can be predicted, again without regard to the network contents. Although a network may have any number of ports, network parameters can be explained most easily by considering a network with only two ports, an input port and an output port, like in Fig. 2.14. To characterize a network, any of the several parameter sets can be chosen; each of these offers certain advantages [Pac96]. Each parameter set is related to a group of four variables associated with the two-port model. Two variables represent the excitation of the network (independent variables), and the other two represent the response of the network to the excitation (dependent variables).

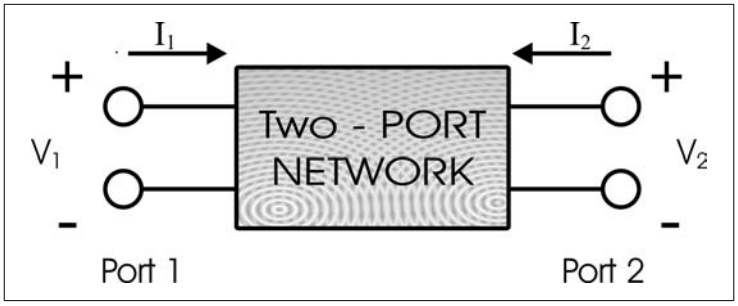

Figure 2.14: General two-port network

Y-parameters

If the network is excited by voltage sources v_1 and v_2, the network currents i_1 and i_2 will be related to them by the following equations:

$$i_1 = y_{11}v_1 + y_{12}v_2 \ , \tag{2.68}$$
$$i_2 = y_{21}v_1 + y_{22}v_2 \ , \tag{2.69}$$

where $Y = \begin{pmatrix} y_{11} & y_{12} \\ y_{21} & y_{22} \end{pmatrix}$ is called the admittance matrix.
In the absence of additional information, four measurements are required to determine the four parameters y_{11}, y_{12}, y_{21}, y_{22}. Each measurement is carried out with one port of the network excited by a voltage source, while the other port is short circuited, as better listed in the follows:

$$y_{11} = \left.\frac{i_1}{v_1}\right|_{v_2 = 0}, \text{ output short circuited,} \tag{2.70}$$
$$y_{12} = \left.\frac{i_1}{v_2}\right|_{v_1 = 0}, \text{ input short circuited,} \tag{2.71}$$
$$y_{21} = \left.\frac{i_2}{v_1}\right|_{v_2 = 0}, \text{ output short circuited,} \tag{2.72}$$
$$y_{22} = \left.\frac{i_2}{v_2}\right|_{v_1 = 0}, \text{ input short circuited.} \tag{2.73}$$

Z-parameters

Very similar to the admittance matrix is the impedance matrix. If the network is excited by current sources i_1 and i_2, the network voltages v_1 and v_2 will be related to them by the following equations:

$$v_1 = z_{11}i_1 + z_{12}i_2 \ , \tag{2.74}$$
$$v_2 = z_{21}i_1 + z_{22}i_2 \ , \tag{2.75}$$

where $Z = \begin{pmatrix} z_{11} & z_{12} \\ z_{21} & z_{22} \end{pmatrix}$ is called the impedance matrix.
In the absence of additional information, four measurements are required to determine the four parameters z_{11}, z_{12}, z_{21}, z_{22}. Each measurement is carried out with one port of the network excited by a current source while the other port is open circuited, as better

listed in the follows:

$$z_{11} = \left.\frac{v_1}{i_1}\right|_{i_2 = 0, \text{ output open,}} \tag{2.76}$$

$$z_{12} = \left.\frac{v_1}{i_2}\right|_{i_1 = 0, \text{ input open,}} \tag{2.77}$$

$$z_{21} = \left.\frac{v_2}{i_1}\right|_{i_2 = 0, \text{ output open,}} \tag{2.78}$$

$$z_{22} = \left.\frac{v_2}{i_2}\right|_{i_1 = 0, \text{ input open.}} \tag{2.79}$$

It is easy to see how impedance and admittance matrix are related:

$$Z = Y^{-1} \, . \tag{2.80}$$

h-parameters

Slightly different to the admittance and impedance matrices (but not less important as it will be shown in the next sections) is the hybrid matrix. If the network is excited by input current source i_1 and output voltage source v_2, the network output current i_2 and the network input voltages v_1 will be related to them by the following equations:

$$v_1 = h_{11} i_1 + h_{12} v_2 \, , \tag{2.81}$$

$$i_2 = h_{21} i_1 + h_{22} v_2 \, , \tag{2.82}$$

where $h = \begin{pmatrix} h_{11} & h_{12} \\ h_{21} & h_{22} \end{pmatrix}$ is called the hybrid matrix.
In the absence of additional information, four measurements are required to determine the four parameters h_{11}, h_{12}, h_{21}, h_{22}, as better listed in the following:

$$h_{11} = \left.\frac{v_1}{i_1}\right|_{v_2 = 0, \text{ output short,}} \tag{2.83}$$

$$h_{12} = \left.\frac{v_1}{v_2}\right|_{i_1 = 0, \text{ input open,}} \tag{2.84}$$

$$h_{21} = \left.\frac{i_2}{i_1}\right|_{v_2 = 0, \text{ output short,}} \tag{2.85}$$

$$h_{22} = \left.\frac{i_2}{v_2}\right|_{i_1 = 0, \text{ input open.}} \tag{2.86}$$

S-parameters

Even if all parameter sets contain the same information about a network, and it is always possible to obtain any set from another set (Table 2.1), **scattering parameters** are

S to Z $Z' = \frac{Z}{Z_0}$	**Z to S** $Z = Z'Z_0$
$z'_{11} = \frac{(1+s_{11})(1-s_{22})+s_{12}s_{21}}{(1-s_{11})(1-s_{22})-s_{12}s_{21}}$	$s_{11} = \frac{(z'_{11}-1)(1+z'_{22})-z'_{12}z'_{21}}{(1+z'_{11})(1+z'_{22})-z'_{12}z'_{21}}$
$z'_{12} = \frac{2s_{12}}{(1-s_{11})(1-s_{22})-s_{12}s_{21}}$	$s_{12} = \frac{2z'_{12}}{(1+z'_{11})(1+z'_{22})-z'_{12}z'_{21}}$
$z'_{21} = \frac{2s_{21}}{(1-s_{11})(1-s_{22})-s_{12}s_{21}}$	$s_{21} = \frac{2z'_{21}}{(1+z'_{11})(1+z'_{22})-z'_{12}z'_{21}}$
$z'_{22} = \frac{(1-s_{11})(1+s_{22})+s_{12}s_{21}}{(1-s_{11})(1-s_{22})-s_{12}s_{21}}$	$s_{22} = \frac{(1+z'_{11})(z'_{22}-1)-z'_{12}z'_{21}}{(1+z'_{11})(1+z'_{22})-z'_{12}z'_{21}}$
S to Y $Y = Y'Z_0$	**Y to S** $Y' = \frac{Y}{Z_0}$
$y'_{11} = \frac{(1-s_{11})(1+s_{22})+s_{12}s_{21}}{(1+s_{11})(1+s_{22})-s_{12}s_{21}}$	$s_{11} = \frac{(1-y'_{11})(1+y'_{22})+y'_{12}y'_{21}}{(1+y'_{11})(1+y'_{22})-y'_{12}y'_{21}}$
$y'_{12} = \frac{-2s_{12}}{(1+s_{11})(1+s_{22})-s_{12}s_{21}}$	$s_{12} = \frac{-2y'_{12}}{(1+y'_{11})(1+y'_{22})-y'_{12}y'_{21}}$
$y'_{21} = \frac{-2s_{21}}{(1+s_{11})(1+s_{22})-s_{12}s_{21}}$	$s_{21} = \frac{-2y'_{21}}{(1+y'_{11})(1+y'_{22})-y'_{12}y'_{21}}$
$y'_{22} = \frac{(1+s_{11})(1-s_{22})+s_{12}s_{21}}{(1+s_{11})(1+s_{22})-s_{12}s_{21}}$	$s_{22} = \frac{(1+y'_{11})(1-y'_{22})+y'_{12}y'_{21}}{(1+y'_{11})(1+y'_{22})-y'_{12}y'_{21}}$
S to h $h_{11} = h'_{11}Z_0$	**h to S** $h_{22} = \frac{h'_{22}}{Z_0}$
$h'_{11} = \frac{(1+s_{11})(1+s_{22})-s_{12}s_{21}}{(1-s_{11})(1+s_{22})+s_{12}s_{21}}$	$s_{11} = \frac{(h'_{11}-1)(1+h'_{22})-h_{12}h_{21}}{(1+h'_{11})(1+h'_{22})-h_{12}h_{21}}$
$h_{12} = \frac{2s_{12}}{(1-s_{11})(1+s_{22})+s_{12}s_{21}}$	$s_{12} = \frac{2h_{12}}{(1+h'_{11})(1+h'_{22})-h_{12}h_{21}}$
$h_{21} = \frac{-2s_{21}}{(1-s_{11})(1+s_{22})+s_{12}s_{21}}$	$s_{21} = \frac{-2h_{21}}{(1+h'_{11})(1+h'_{22})-h_{12}h_{21}}$
$h'_{22} = \frac{(1-s_{11})(1-s_{22})-s_{12}s_{21}}{(1-s_{11})(1+s_{22})+s_{12}s_{21}}$	$s_{22} = \frac{(1+h'_{11})(1-h'_{22})+h_{12}h_{21}}{(1+h'_{11})(1+h'_{22})-h_{12}h_{21}}$

Table 2.1: Parameter conversion table.

important in microwave design, because they are easier to measure at higher frequencies than the others. They are conceptually simple, dimensionless, analytically convenient, and capable of providing a great insight into a measurement or design problem.

Scattering parameters are commonly called S-parameters; they relate to travelling waves, which are scattered or reflected when a n-port network is inserted into a transmission line. Their definition, given by Kurokawa [Kur65], starts with the normalized complex voltage waves:

$$a_i = \frac{V_1 + Z_i I_1}{2\sqrt{|Re(Z_i)|}} \,, \tag{2.87}$$

$$b_i = \frac{V_1 - Z_i^* I_1}{2\sqrt{|Re(Z_i)|}} \,. \tag{2.88}$$

In the available measurement systems, there is only a 2-port network (i=1,2) and the reference impedances Z_i are real and equal to Z_0 (50Ω as described in the calibration section).

$$a_1 = \frac{V_1 + Z_0 I_1}{2\sqrt{Z_0}} = \frac{\text{voltage wave incident on PORT1}}{\sqrt{Z_0}} \,, \tag{2.89}$$

$$a_2 = \frac{V_2 + Z_0 I_2}{2\sqrt{Z_0}} = \frac{\text{voltage wave incident on PORT2}}{\sqrt{Z_0}} \,, \tag{2.90}$$

$$b_1 = \frac{V_1 - Z_0 I_1}{2\sqrt{Z_0}} = \frac{\text{voltage wave reflected from PORT1}}{\sqrt{Z_0}} \,, \tag{2.91}$$

$$b_2 = \frac{V_2 - Z_0 I_2}{2\sqrt{Z_0}} = \frac{\text{voltage wave reflected from PORT2}}{\sqrt{Z_0}} \,. \tag{2.92}$$

The linear equations describing the 2-port network are:

$$b_1 = s_{11} a_1 + s_{12} a_2 \,, \tag{2.93}$$

$$b_2 = s_{21} a_1 + s_{22} a_2 \,, \tag{2.94}$$

where $S = \begin{pmatrix} s_{11} & s_{12} \\ s_{21} & s_{22} \end{pmatrix}$ is the matrix of the following S-parameter:

$$s_{11} = \left.\frac{b_1}{a_1}\right|_{a_2=0} \hookrightarrow \text{Input reflection coefficient with the output port terminated by a matched load. } Z_L = Z_0 \Rightarrow a_2 = 0, \tag{2.95}$$

$$s_{12} = \left.\frac{b_1}{a_2}\right|_{a_1=0} \hookrightarrow \text{Reverse transmission gain with the input port terminated by a matched load. } Z_S = Z_0 \Rightarrow a_1 = 0, \tag{2.96}$$

$$s_{21} = \left.\frac{b_2}{a_1}\right|_{a_2=0} \hookrightarrow \text{Forward transmission gain with the output port terminated by a matched load. } Z_L = Z_0 \Rightarrow a_2 = 0, \tag{2.97}$$

$$s_{22} = \left.\frac{b_2}{a_2}\right|_{a_1=0} \hookrightarrow \text{Output reflection coefficient with the input port terminated by a. matched load. } Z_L = Z_0 \Rightarrow a_2 = 0. \tag{2.98}$$

2.3.2 Negative differential conductance oscillators

An oscillator can be considered as the combination of an active multiport and a passive multiport (the embedding network). For the active device, we have:

$$[V] = [Z][I] \, , \tag{2.99}$$

and for the embedding network:

$$[V'] = [Z'][I'] \, . \tag{2.100}$$

In our case, Z and Z' are the impedance matrixes of the diode and of the passive elements. By connecting the active and the embedding network:

$$[I] = -[I'] \, , \tag{2.101}$$

$$[V] = [V'] \, , \tag{2.102}$$

and from Eq. (2.99) and Eq. (2.100) results:

$$\{[Z] + [Z']\}[I] = 0 \, . \tag{2.103}$$

Now since $[I] \neq 0$, the matrix [Z]+[Z'] is singular or

$$det([Z] + [Z']) = 0 \, . \tag{2.104}$$

Equation 2.104 is the generalized oscillation condition. Since Z is a function of the frequency and of the voltage, the oscillating frequency can be determined for a given bias point. It can be demonstrated that an equivalent condition of Eq. (2.104) is [KO81]:

$$det([S][S'] - 1) = 0 \tag{2.105}$$

or in a similar way

$$det([Y] + [Y']) = 0 \, , \tag{2.106}$$

where S and Y are the scattering and admittance matrices of the diode and S' and Y' are the scattering and admittance matrices for the passive elements, respectively. If maximum power output and efficiency are not of prime importance, a satisfactory oscillator design can be achieved using small-signal scattering matrix parameters. The major shortcoming of small signal oscillator design is that it does not provide any way of predicting the steady-state oscillating signal level. Oscillator design based on large-signal scattering matrix (i.e. non-linear) parameters is much more complicated because of the difficulty of obtaining large-signal parameters.

2.3.3 Gunn oscillation modes

In order to generate microwave power, a transferred electron device has to be placed in a cavity or in a resonant circuit. Several modes of operation can be distinguished. Each of them provides particular advantages or disadvantages from the point of view of tunability, stability and efficiency. The following four main operation modes will be discussed [Hei71, Hob74]:

- the Transit Time mode,
- the Delayed Domain mode,
- the Quenched Domain mode,
- the LSA mode.

The Transit Time mode.

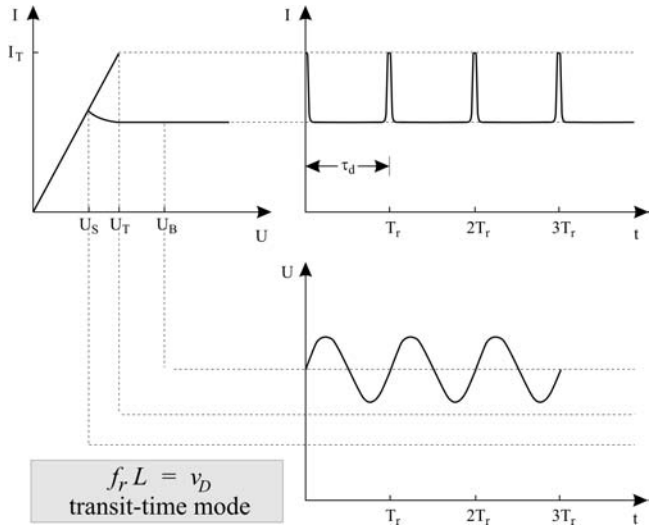

Figure 2.15: Current and voltage time evolution of the Gunn oscillator operating in the Transit Time mode.

In a purely resistive circuit, the oscillation frequency f_r is determined by the space charge or domain transit time τ_d:

$$f_r = \frac{1}{\tau_d} = \frac{v_{drift}}{L} \ . \tag{2.107}$$

This operating mode is commonly called Transit Time mode. The current flows with a sequence of short current pulses with the period τ_d. The current spikes occur when a domain enters the anode and the next one is originating from the cathode. The voltage is sinusoidal with the same period (Fig. 2.15). If the circuit is heavily loaded, the R.F. voltage is small enough not to oscillate below U_T.

The efficiency of the Transit Time mode is not particularly high because of the narrowness of the current pulse and the small r.f. voltage amplitude. Moreover, the frequency range is fixed to the natural domain transit frequency. This disadvantage influences also the frequency stability, because the domain transit time is strongly temperature dependant.

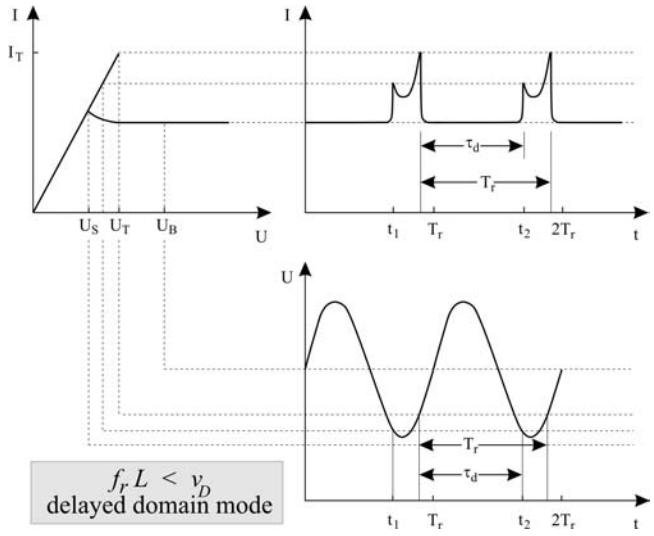

Figure 2.16: Current and voltage time evolution of the Gunn oscillator operating in the Delayed Domain mode.

The Delayed Domain mode.

In this case, the resonant period of the circuit $T_r = 1/f_r$ is longer than τ_d:

$$\frac{1}{2 \cdot \tau_d} = \frac{v_{drift}}{2 \cdot L} < f_r < \frac{1}{\tau_d} = \frac{v_{drift}}{L} \; . \tag{2.108}$$

The amplitude of the voltage sinusoidal waveform (Fig. 2.16) has to be large enough to cause the voltage to fall below threshold U_T over a portion of the cycle. The domain reaches the anode and disappears during the second half of the voltage oscillation, while the voltage is below the threshold. Before the next domain can be nucleated, the voltage has to rise again over the threshold. The efficiency of the Delayed Domain mode is higher than for the Transit Time and, thanks to the larger current pulses, can reach up to 7.2% [War66]. The frequency is controlled by the resonant circuit, whose tunability can be mechanical or electrical (parallel Schottky varactors). A good temperature stability is achieved, generally, for aluminium cavities or DRO (Dielectric Resonator Oscillators).

The Quenched Domain mode.

For this mode, the resonant period of the circuit $T_r = 1/f_r$ is shorter than τ_d, but longer than the domain nucleation and extinction time τ_s:

$$\frac{1}{\tau_d} = \frac{v_{drift}}{L} < f_r < \frac{1}{\tau_s} \; . \tag{2.109}$$

The circuit loading is further reduced and the voltage falls below the domain sustaining voltage U_S for a portion of the cycle. The domain is generated in the cathode and, before

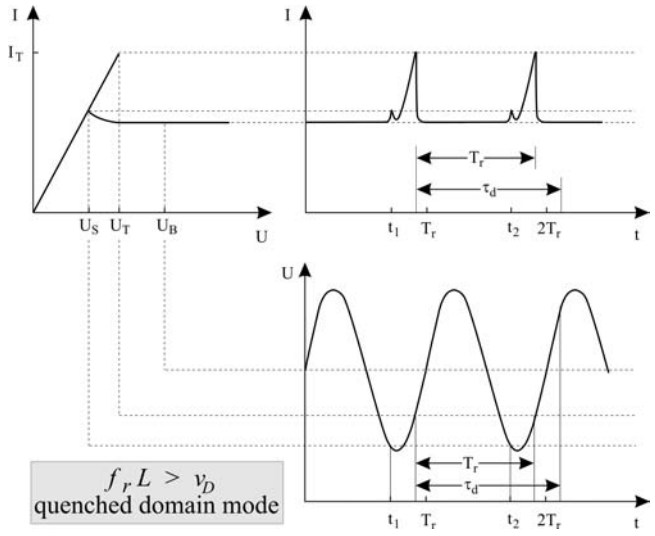

Figure 2.17: Current and voltage time evolution of the Gunn oscillator operated in the Quenched Domain mode.

reaching the anode, is quenched in flight, because the voltage falls below U_S. The next domain can not be nucleated until the terminal voltage rises above the threshold U_T. The main advantage of this mode consists in the generation of frequencies higher than the transit-time frequency. Considering the area under the current-pulse, it is evident that the efficiency of the Quenched Domain mode (5% [Hob74]) is higher than the one of the Transit Time mode, but lower than the one of the Delayed Domain mode.

The LSA mode.

It has been already anticipated, that a domain can be quenched before reaching the anode, if the device bias falls below U_S. The lifetime of the domain is connected with the resonance frequency of the circuit. If the frequency is high enough, the domain will not have time to fully nucleate and the diode operates in the LSA mode. LSA stands for Low Space-charge Accumulation. In this context, the I-V characteristics of the device should follow the v-E, which exhibits a region of negative differential mobility.
A first advantage of this mode consists in the high frequencies, which are achievable: the device length is not related to the oscillating frequency, which can be many times the transit time frequency (*overlength Gunn oscillator*). The second advantage concerns the R.F. output power: in the LSA mode, higher terminal voltages may be applied without causing impact ionizations [Hob74] and outstanding efficiencies up to 18.5% are reported [Cop67b].
The performances of the LSA mode are limited by four practical constraints to prevent the domain formation:

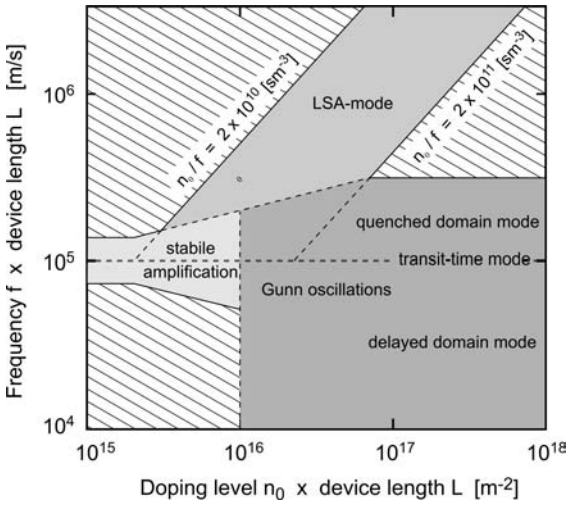

Figure 2.18: Representation of the operating modes of a Gunn diode [Cop67a]. The allocation of the different categories depends on three parameters: n_0L, fL and n_0/f.

- The doping concentration divided by the frequency n_0/f must remain in the interval $[2 \cdot 10^{10}, 2 \cdot 10^{11}]$ sm^{-3} (GaAs case) [Cop67b].
- The homogeneity of the doping concentration and of the related low field conductivity must be better than 10% [Cop67b, Hob72].
- Not to distort the uniform-field conditions with the unavoidable accumulation layer, the device must be much longer than the space-charge transit length per cycle.
- The oscillating circuit must be designed in a way to prevent a long delay before starting the oscillation. During this delay, a domain could nucleate and cause device breakdown by impact ionization.

Operating modes overview for a transferred electron device.

Figure 2.18 summarizes the operating modes of a GaAs transferred electron device as a function of the doping concentration, frequency and device length. Three different situations can be distinguished: stable amplification, domain oscillation and LSA oscillation. For $n_0L < 10^{16}$ m^{-2}, no domain formation appears and the device can be used as an amplifier in frequency ranges around the transit frequency. For $n_0L > 10^{16}$ m^{-2} three different domain oscillation modes are possible depending on the resonator frequency: Transit Time, Delayed Domain and Quenched Domain mode. For higher frequencies and for $n_0/f \in [2 \cdot 10^{10}, 2 \cdot 10^{11}]$ sm^{-3}, we have the LSA mode.

The presented boundaries should not be regarded as absolute. The device behaviour next to the boundaries is also depending on the bias voltage, device temperature and circuit loading.

2.4 The thermal behaviour of a Gunn diode

In today's environment of high performance semiconductor devices, the common complaints that it is possible to "cook an egg" or "warm your coffee" on an electronic appliance like a typical modern computer are not that far fetched. Many semiconductor manufacturers have grappled with the difficulty of combining highly evolved thermal dissipation techniques with the dual requirement of packaging simplicity and reliability. In this context, the problem of the Gunn diode cooling is crucial.

As illustrated in the previous chapters, the efficiency of a Gunn diode is not very high. In order to achieve the required R.F. output levels, D.C. power densities greater than 140 kW/cm^2 are reached[5]. Therefore, in addition to good electric contacts, the Gunn diode requires good thermal contacts to the environment to avoid its destruction by overheating.

The standard packaging consists in the removal of the heat occurring from one end of the device with an integrated gold heat sink. The heat-sink is electroplated on the semiconductor and then bounded to a copper pedestal ultrasonically or by thermocompression. Only for research purposes, sometimes copper is replaced with diamond, for which the thermal conductivity at room temperature is 30 times higher than copper.
In this work, an original quasi-planar double-sided heat-sinking is presented: from the bottom side, the heat flows through the semiconductor substrate and from the top side, thick gold airbridges for electrical connections are exploited also as heat-sink.

In this section after an analytical description of the thermal problem, finite elemente simulations of the standard and the double-sided heat-sink are compared. The efficiency of the top contact heat-sink is presented here theoretically and in chapter 6 experimentally.

2.4.1 Analytical solution of the simplified static heat transfer problem

For most geometries, the detailed solution of the heat-flow problem through a small active device in a massive heat-sink is complicated.
In the case of simple conduction[6], the heat transfer equation is given by:

$$-\nabla \cdot (\lambda \nabla T) = q \,, \tag{2.110}$$

where q is the power density of the heat source $[Wm^{-3}]$ and λ is the thermal conductivity[7].

In order to achieve simple analytical solutions, some assumptions are required. If interfacial and contact electrical resistances are negligible, all the heat is dissipated in the active region of the device. The composite geometry of the heat flow can be simplified as shown in Fig. 2.19. The Gunn device is considered as a series connection of a one dimensional active device region and a heat-sink with spherical symmetry heat flow.

[5] Think of 140 electric irons on a T-shirt of one cm^2.

[6] Only the stationary solution are considered ($\partial T/\partial t = 0$). The convection and the irradiation flow are not relevant for the Gunn device.

[7] Further on λ is assumed as a scalar value (isotropic condition), constant with temperature and pressure.

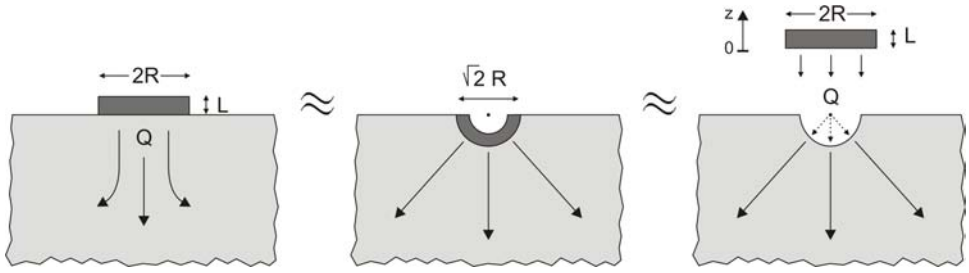

Figure 2.19: Approximation of the device geometry to simplify the heat transfer problem [Hob74].

The solution of of the first part of the heat flow problem for the one dimensional active region (dark-gray Fig. 2.19) with uniform heating is well-known [Hob74]:

$$T_{MAX} - T_0 = \frac{Ql}{2\pi R^2 \lambda_{AR}} \,, \tag{2.111}$$

where T_{MAX} is the maximum temperature, T_0 is the temperature at the border, L is the diode length, R is the diode radius, λ_{AR} is the thermal conductivity of the active region and $Q = q \cdot (l\pi R^2)$ is the dissipated power. The solution of the second part of the problem (heat flow in the heat-sink, light-gray Fig. 2.19)) ,considering a point source and spherical symmetry, is given by [Hob74]:

$$T_0 - T_\infty = \frac{Q}{\sqrt{2}\pi R \lambda_{HS}} \,, \tag{2.112}$$

where λ_{HS} is the thermal conductivity of the heat-sink.
Combining together Eq. (2.111) and Eq. (2.114), the complete heat flow equation is

$$T_{MAX} - T_\infty = \frac{QL}{2\pi R^2 \lambda_{AR}} + \frac{Q}{\sqrt{2}\pi R \lambda_{HS}}. \tag{2.113}$$

The thermal resistance Z_{TH} of the whole system Gunn diode and heat-sink is:

$$Z_{TH} = \frac{T_{MAX} - T_\infty}{Q} = \frac{L}{2\pi R^2 \lambda_{AR}} + \frac{1}{\sqrt{2}\pi R \lambda_{HS}}. \tag{2.114}$$

Equation 2.113 confirms that, for a given device length, it is preferable to have the radius R as large as possible. At the same time, in order to keep the electrical resistance constant, the device resistivity must increase. The resistivity is depending on the electron concentration. However, too low doping concentrations have to be considered with caution, in order to avoid low rf efficiencies.

Another important factor for Eq. (2.113) is the thermal conductivity: it depends extremely of material. The active region thermal conductivity for GaAs, InP and GaN are: $\lambda_{GaAs} = 45.5\ Wm^{-1}K^{-1}$, $\lambda_{InP} = 68\ Wm^{-1}K^{-1}$ and $\lambda_{GaN} = 130\ Wm^{-1}K^{-1}$.

The excellent value of GaN are compensated by the power density, which this material requires before having transferred electron effects. Crucial for reducing the thermal resistance is also the material choice of the heat-sink. Materials, which are often used, are: copper ($\lambda_{Cu} = 400\ Wm^{-1}K^{-1}$), gold ($\lambda_{Au} = 317\ Wm^{-1}K^{-1}$) and diamond ($\lambda_{diamond} = 2500\ Wm^{-1}K^{-1}$).

As an example, the temperature within the GaAs is computed for the case of an integrated gold heat-sink. A diode length L of 1.6 μm and a radius R of 35 μm have been considered with a dissipated power of Q = 5 W. For an environment temperature of $T_\infty = 300°$ K, the resulting maximal temperature within the device is

$$T_{MAX} \approx 426°K. \tag{2.115}$$

Replacing the gold heat-sink with a GaAs substrate, it follows

$$T_{MAX} \approx 1030°K. \tag{2.116}$$

Without heat-sink, the temperature is more than the double and the diode would be destroyed immediately.

2.4.2 Finite elemente simulations of the temperature distributions in a Gunn diode

The problem of the heat flow in Gunn diodes has been solved numerically with the commercial software *Finite Element Method Laboratory*. FEMLAB is a modelling package for the simulation of physical processes, which can be described via partial differential equations. The modelling activity is a sequence of four steps:

- Create the diode geometry with a 3D CAD environment.
- Define the physics of the heat flow including the necessary material parameters.
- Generate the finite elemente mesh.
- Compute and analyze the solution.

The simulation has been performed on two structures: a conventional Gunn diode chip and a quasi-planar Gunn diode with air-bridges.

The Gunn diode chip is composed of a cylindrical top gold contact with a diameter of 70 μm, a GaAs mesa with the same area and a conventional bottom heat-sink. The heat-sink consists of a cylindrical gold contact with a diameter of 350 μm and a height of 40 μm, laying on top of a copper block with a diameter of 800 μm and a height of 100 μm. As a boundary condition, the outer faces of the whole structure are kept thermally isolated, except for the copper bottom face, which is kept at a constant temperature of $300°K$.

The quasi-planar Gunn diode is composed of a GaAs mesa on top of a 350 μm thick GaAs substrate. The top face of the mesa ($18 \times 20\ \mu m^2$) is connected with 3 μm thick gold air-bridges to the substrate at a distance of 10 μm. The same boundary conditions have been chosen: the outer faces of the whole structure are thermally isolated, except

for the GaAs substrate bottom face, which is kept at a constant temperature of $300°K$. In both cases, the GaAs mesa is divided into a 1.6 μm active layer with a constant uniform power dissipation ($5\ V \times 26000\ kA/cm^2$) and two contact layers of 700 nm. No irradiation process has been considered.

The results of the simulations are presented in Fig. 2.20 - 2.23. In Fig. 2.20 and in Fig. 2.21, the temperature distribution is shown for the Gunn diode chip and for the quasi-planar Gunn diode, respectively. A 3D and a cross-sectional view of the two structures visualises the different temperature regions by means of different color levels. The maximal temperature reached by the Gunn diode chip is $471°K$. This result agrees well with similar computations ($475°K$) reported by Cords and Förster [CF02]. In the case of the quasi-planar Gunn diode, a higher temperature is expected, considering the poor thermal conductivity of the GaAs substrate. Surprisingly, the maximal temperature is only nine degree higher ($480°K$): the gold air-bridges spread the heat from the top increasing the interface area between the diode and the GaAs substrate. The thicker the gold air-bridges, the better the top-side cooling.
In Fig. 2.22 and in Fig. 2.23, the heat flux profile is presented: the background color and the size of the cones are proportional with the heat flux intensity. For the Gunn diode chip, the maximal heat flux is close to the border of the active region at the interface between GaAs and gold. The maximal flux intensity of 192 kW/cm^2 again agrees well with Cords' and Förster's result of 189 kW/cm^2.
For the quasi-planar Gunn diode, a high heat-flux is located at the border of the active region at the interface with the GaAs substrates. This region seams to be material independent, since a similar zone can be seen in the Gunn diode chip. Anyway, the highest heat flux values can be found in the arms of the gold air-bridges, confirming the important role, which they have in planar Gunn diodes.

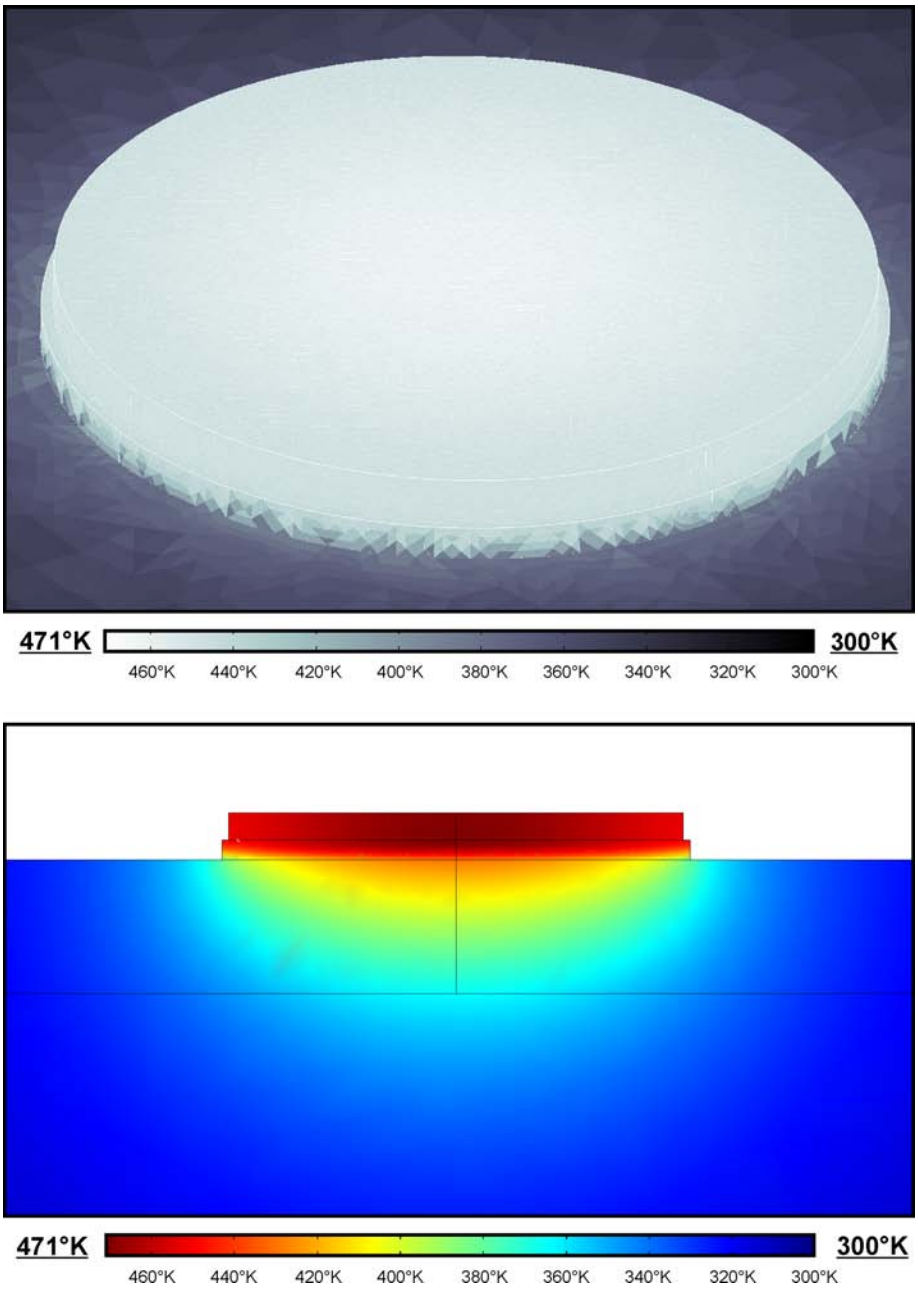

Figure 2.20: Heat-sink temperature profile for a standard Gunn diode chip.

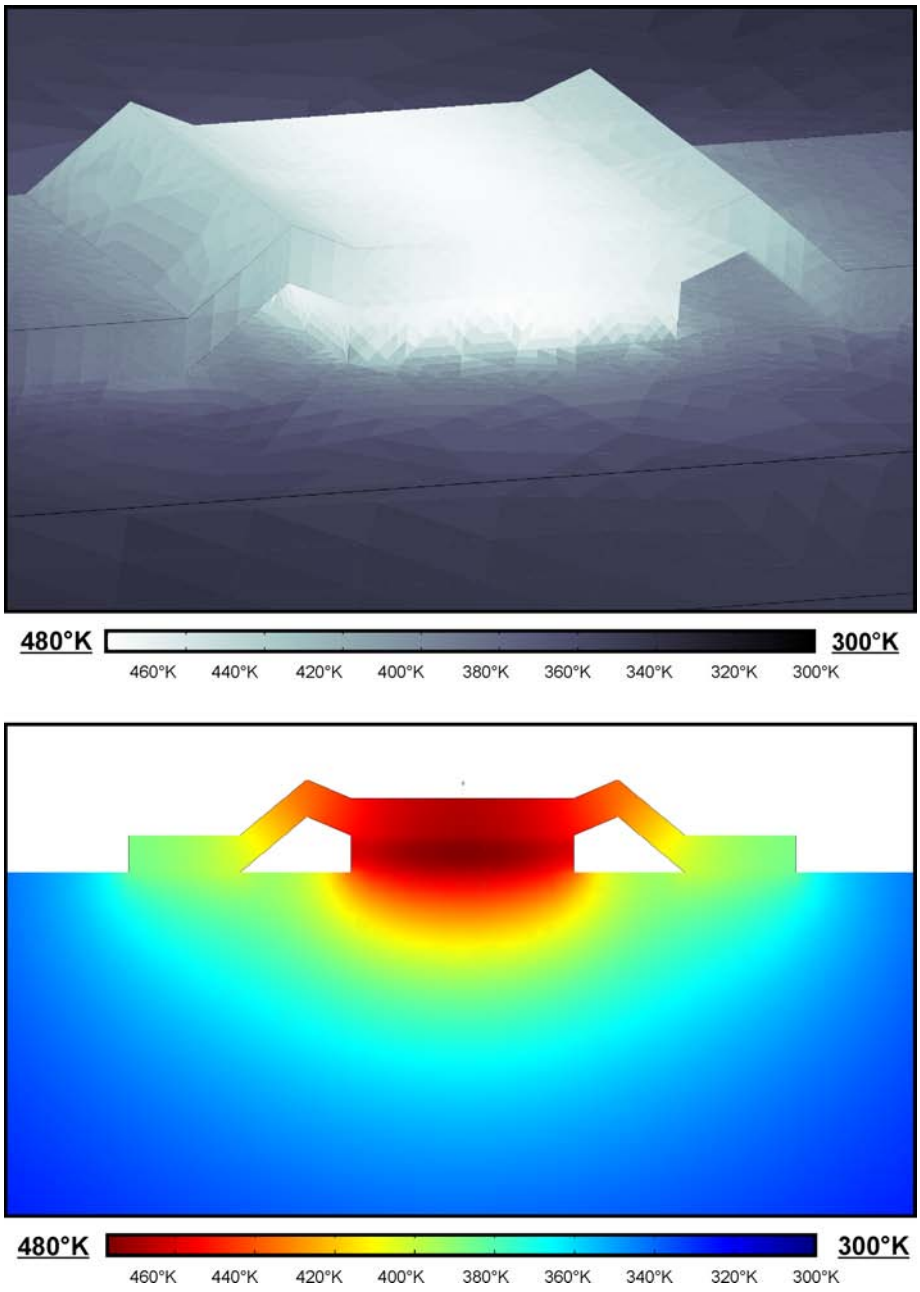

Figure 2.21: Double-sided heat-sink temperature profile for a quasi-planar Gunn diode.

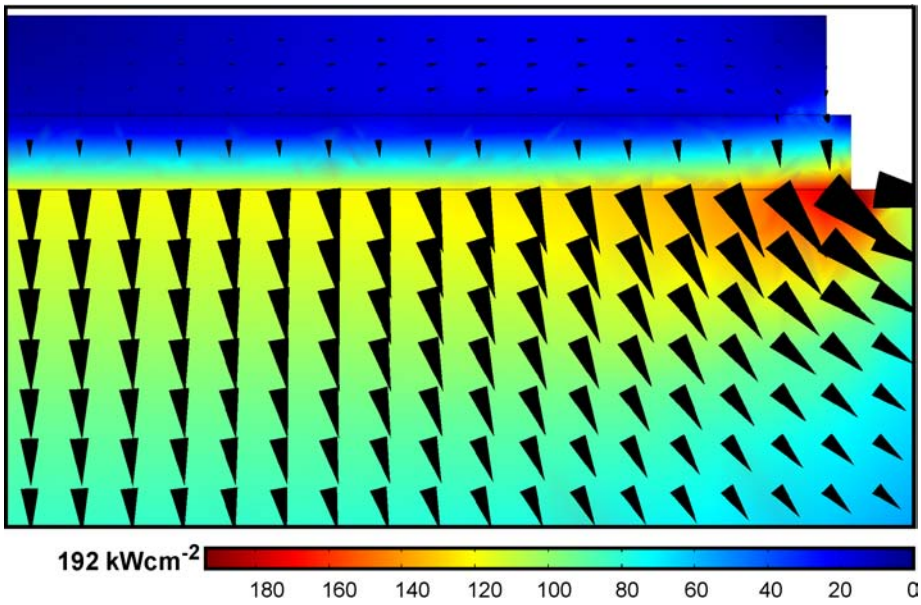

Figure 2.22: Heat flux profile for a standard Gunn diode chip.

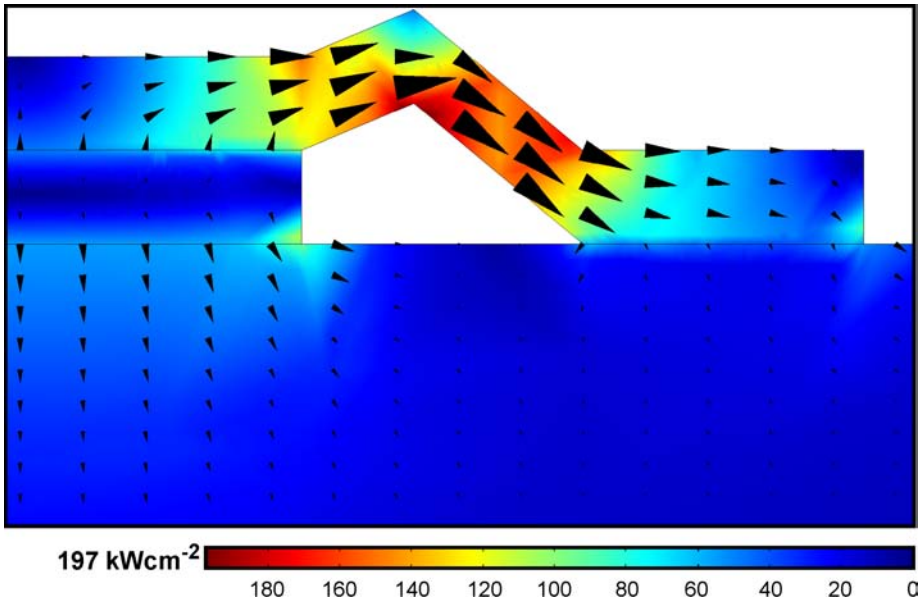

Figure 2.23: Heat-flux profile for a quasi-planar Gunn diode.

Chapter 3

III-V compound semiconductor material systems

This chapter offers a short overview of the employed material systems and of the epitaxy techniques used for the layer structure growth. Furthermore, the Gunn diode layer structures considered in this dissertation are described. In one particular case, the resonant tunneling injector Gunn diode, simulation results support the design choice.

3.1 Group-III/As and group-III/N material systems

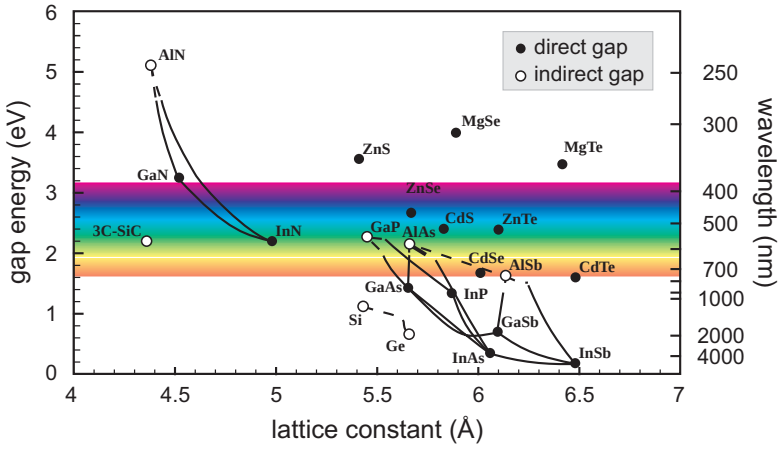

Figure 3.1: Bandgaps of the most important elemental and binary cubic semiconductors versus their lattice constant at 300°K. The right-hand scale gives the light wavelength λ, corresponding to the band gap energy [IL03, Riz01].

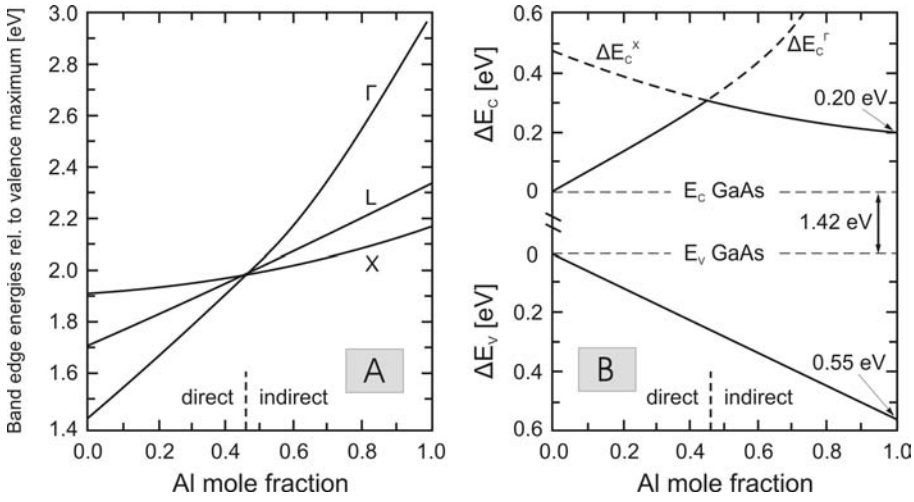

Figure 3.2: Bandgap energies of $Al_xGa_{1-x}As$ in different points of the Brillouin zone plotted versus the Al concentration [Kel96, Mal02]

3.1.1 GaAs, AlAs

Since the early days of semiconductor technology, the investigation on new phenomena in solid state physics lead to new devices and ICs. A number of different materials have been studied. Among all the new materials, the one that has received most attention is gallium arsenide, together with some of its closely related binary, ternary and quaternary compounds. After silicon, gallium arsenide is now regarded as the second most important electronic material.

Goldschmidt was the first who created GaAs in 1929. He found that it has a zincblende lattice with a FCC symmetry [Gol29]. Only in 1952, in fact, GaAs has been identified as a semiconductor by Welker (Siemens)[1]. The nature of the bond between gallium and arsine is predominantly covalent. The first device exploiting the direct band-gap of GaAs dates from 1962, when Hall et al. at GE [HFKC62] and Redhiker at al. at MIT Lincoln Laboratory [QRK+62], independently, obtained the first semiconductor laser. In the same year, Gunn (IBM) discovered the transferred electron effect and developed the first solid state microwave oscillator [Gun63].

Figure 3.1 shows the energy gaps and the lattice constants of of the most important elemental and binary cubic semiconductors. The connecting lines consider the case of ternary compounds, composed of various ratios of the corresponding binary materials. The compound $Al_xGa_{1-x}As$ maintains nearly the same lattice constant with the change of the Al mole fraction. This property and the related high quality heteroepitaxy have

[1]Goryunova described III-V materials as semiconductors for the first time in 1950. In her Ph.D. thesis, completed in 1951 at Leningrad State University, she indicated that III-V zinc-blend compounds are semiconductors. Due to the Cold War, her work was published outside the U.S.S.R. much later.

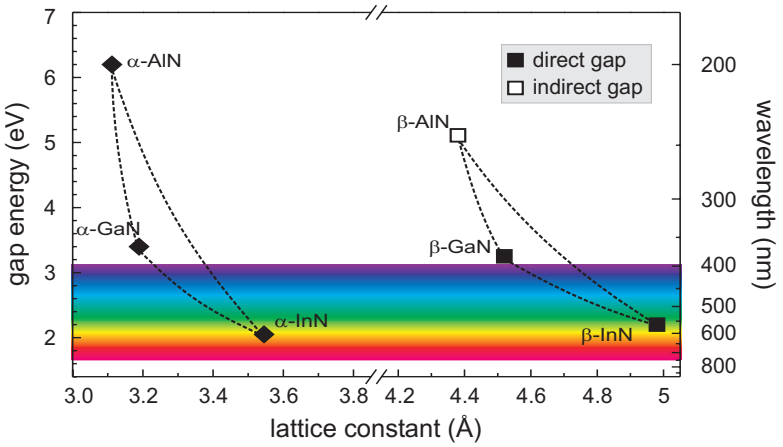

Figure 3.3: Bandgaps of III-N semiconductors with wurtzite ($\alpha - phase$) and zincoblende ($\beta - phase$) structure versus their lattice parameter at 300°K. The right-hand scale gives the light wavelength λ, corresponding to the band gap energy [Riz01].

opened new possibilities for advanced devices like double heterostructure lasers, high electron mobility transistors and heterostructure bipolar transistors; to describe the large possibilities offered by the epitaxial growth using $Al_xGa_{1-x}As$, and in general III/V compounds, a new expression has been coined: *bandgap engineering*.

In Fig. 3.2, the bandgap energy of the $Al_xGa_{1-x}As$ material system is plotted versus the Al concentration in different points of the Brillouin zone. At about 45% Al, the transition between direct and indirect bandgap can be observed.

3.1.2 GaN, AlN

As in the case of arsenides, between group III - elements and nitrogen, the nature of the bond is mainly covalent. However, for the nitrides, the large difference in the electronegativities causes a strong ionic component, which means very high bonding energies (AlN 11.5, GaN 8.9 and InN 7.7 $eV/atom$) and consequently excellent thermal and chemical stability. In contrast to GaAs, the thermodynamically stable phase of these materials is the hexagonal wurtzite structure, $\alpha - phase$. Beside to $\alpha - phase$, a metastable $\beta - phase$ with zincblende structure exists if very thin layers of GaN and InN are grown on cubic substrates like GaAs or silicon. The nitride materials with wurtzite structure form an alloy system (InGaN, AlGaN, InAlN), whose direct bandgaps range from 0.7 to 6.2 eV (Fig. 3.3). These give to group III-nitride unique optical properties, making them suitable for a large spectrum of optoelectronic applications. Another peculiarity of group III nitrides, in comparison with arsenides, is the existence of strong spontaneous and piezoelectric polarization fields. This property leads to an additional carrier accumulation at the strained interfaces $Al_xGa_{1-x}N/GaN$ in 2DEG structures, enhancing the electron

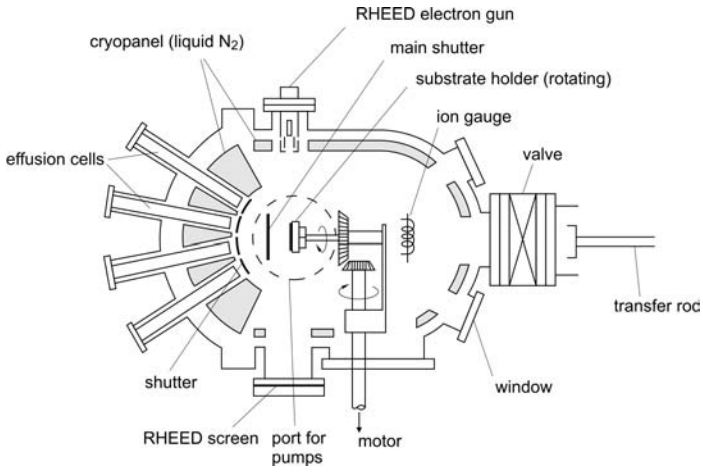

Figure 3.4: Schematic view of a MBE system from [IL03]. (Top cross-view)

concentrations in GaN HEMTs.

3.2 GaAs, AlAs grown by MBE

Molecular beam epitaxy (MBE) is a physical deposition method for growing thin epitaxial structures made of semiconductors, metals or insulators. The word epitaxy stems from the Greek words $\epsilon\pi\iota$ (epi=on) and $\tau\alpha\xi\iota\zeta$ (taxis=order). The etymology of the term already suggests the growth of thin films in an ordered way on a substrate or on a previously deposited layer. Solid source materials contained in *effusion cells* evaporate after the electrical heating. Under Ultra High Vacuum (UHV) conditions, a *molecular* (or atomic) *beam* builds from the evaporated materials. The epitaxial film grows from the *molecular beams* impinging on the substrate. The beams from different sources (*cells*), which have a conic distribution directed to the heated substrate, can be independently controlled by means of *shutters*. In the transition from the gas-phase to the solid-phase, the reciprocal interaction between the molecules causes the crystal formation and the growth takes place. Under optimal conditions, the growth rates, which are typically in the order of 1 monolayer per second (ML/s), are low enough to allow surface migration of the impinging species and smooth surfaces. The homogeneity of the deposited layers along the wafer can be improved adjusting the growth rate and the substrate holder rotation.

The GaAs Gunn diode structures considered in this thesis have been grown by molecular-beam epitaxy (MBE) on 2-inch semi-insulating GaAs substrates in a Varian ModGen II MBE system. The principle scheme of the MBE growth chamber is shown in Fig. 3.4. The substrate holder can be heated up to 900 °C . The source materials Ga, As, In, Al, Si (for n-doping) and Be (for p-doping) are placed in the effusion cells. The

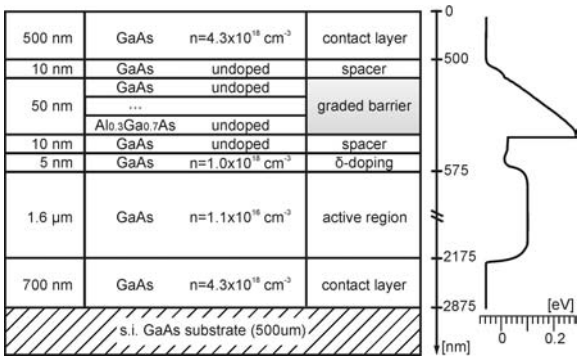

Figure 3.5: Typical layer sequence of the GaAs Gunn diode with a graded gap injector.

growth rate can be measured by a RHEED[2] system and is controlled by tuning the cells temperature. In order to monitor the doping levels, calibration samples are periodically grown and characterized by Hall and CV measurements (sections 4.3 and 4.4).

3.3 GaAs Gunn diode structures

3.3.1 Graded Gap injector GaAs Gunn diodes

In this section, the layer structures of the GaAs Gunn diodes with graded gap injectors (GGI) are presented. The starting point for the chosen layer-system are the structures suggested by Hutchinson at al. [HSCK96] and by Couch et al. [CBK$^+$88]. The optimization work, performed at the institute by Stock [Sto03], provided further helpful indications for the layer-system chioice.

A typical layer sequence of a GaAs Gunn diode with a graded gap injector is sketched in Fig. 3.5. It consists mainly of an undoped AlGaAs graded barrier structure followed by a $\delta-$doping and a thick low doped GaAs active region. The grading is linear, starting from 1.7% up to the maximum Al value. The role of the two 5 nm GaAs spacers is to avoid doping diffusion in the graded barrier.

In this work, different structures have been considered:

- One with a 1.6 μm active region without spacers. The absence of spacers makes the graded gap barrier not effective [Sto03](W16016).
- Two with 1.5 μm and 1.8 μm active regions and with a 50 nm long, 32% Al graded barrier each (W18006 and W18021 respectively).
- Four with 1.6 μm active regions and with 65 nm long, 28%, 30%, 32% and 34%, respectively, Al graded barriers (W18041, W18040, W18038, W18039).

[2]RHEED: Reflection High Energy Electron Diffraction

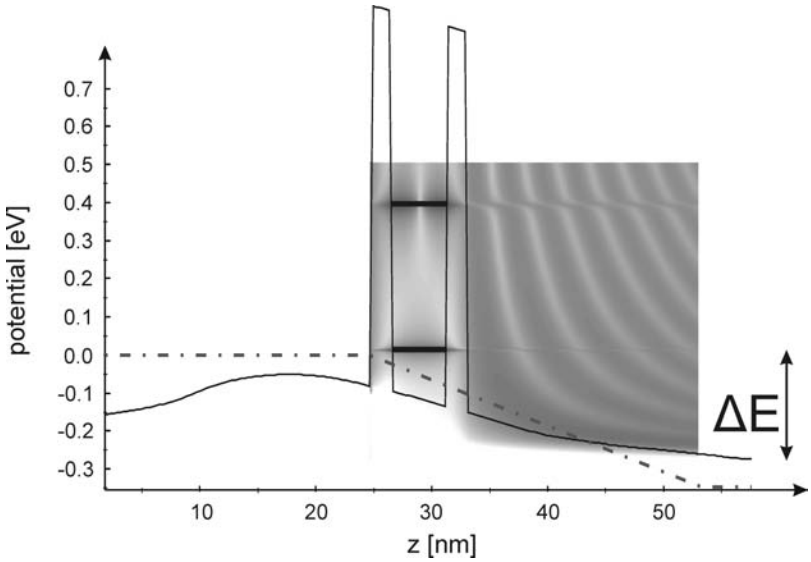

Figure 3.6: Conduction band profile and local density of states plot for a Resonant Tunnelling Injector

The first structure (W16016) is mainly used as a reference. Even if the electrical measurements show no hint of a hot electron injector, W16016 allows a comparison with the other structures. Wafers W18006 and W18021, which have the same full-working graded gap injector, were grown to demonstrate the influence of the active region length on the diode high frequency behaviour. Finally, in wafers from W18038 to W18041, the role of the maximum Al content in the injector has been examined.

3.3.2 Resonant tunneling injector GaAs Gunn diodes

The basic principles of the resonant tunneling injector (RTI) have been already discussed in section 2.2.3. The design of the AlAs double barrier RTI started from numerical simulations. The RTI is a completely new structure and no reference could be found in the literature.

The simulation of the resonant tunneling injector was done with the software package Wingreen [IM]. This is based on a self-consistent real-time Green's function approach [Ind99]. A simulation example is shown in Fig. 3.6. The conduction band and the local density of states of a RTI are presented for an applied bias voltage. The chosen bias voltage corresponds to a current density in the range 23-27 kA/cm^2. The layer structure has to be so that the following condition is satisfied: the first transmission energy level for the given current density range has to match the energy difference between the L- and the Γ-valley ($\Delta E \approx 310\ meV$ for GaAs). In order to make the RTI competitive, a further specification has been defined: the voltage drop on the RTI for the working

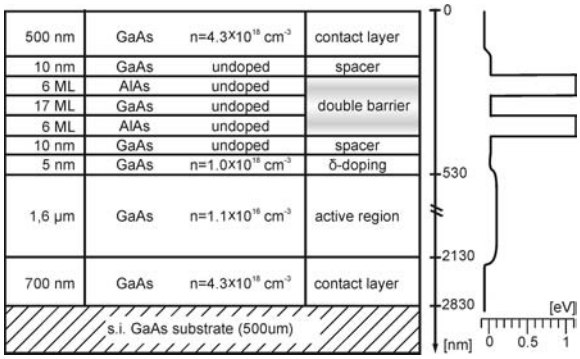

Figure 3.7: Typical layer sequence of the GaAs Gunn diode with a resonant tunneling injector.

current conditions, must be much lower than the one on the GGI.

In Fig. 3.7, a typical layer sequence of the RTI GaAs Gunn diode is presented. The structure is very similar to that of GGI GaAs Gunn diode: the active region, the spacers and the δ-doping layers have not been changed. The injector itself is undoped and consists in a sequence of AlAs/GaAs/AsAs (6 ML/17 ML/6 ML, W18069). A second wafer has been grown decreasing the AlAs thickness from 6 to 5 ML (W18069). The High Resolution Transmission Electron Microscopy (HRTEM) image illustrates a resonant tunneling double barrier with 6 ML of AlAs. The sample has been grown at 580 °C, an optimal temperature for well defined GaAs/AlAs interfaces [Lan99].

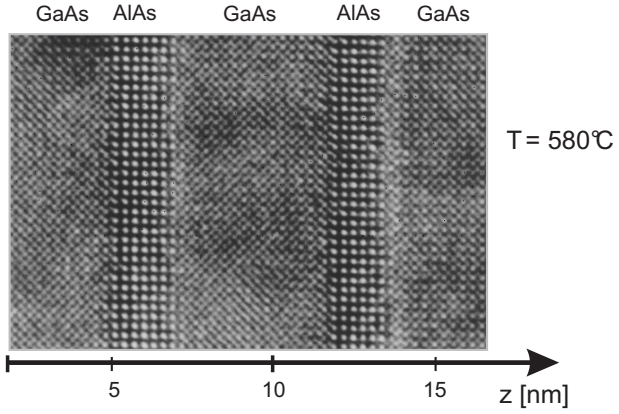

Figure 3.8: HRTEM image of a resonant tunneling double barrier AlAs/GaAs/AlAs (6 ML/17 ML/6 ML). It can be noticed that the interfaces are well-defined and the crystal quality is very good [Lan99].

3.4 GaN grown by MOVPE

In this section, the growth of GaN by Metal Organic Vapor Phase Epitaxy (MOVPE) is shortly explained. To avoid confusion, it should be noted that the epitaxial technique MOVPE is also known by the acronyms MOCVD (metalorganic chemical vapor deposition), OMVPE and OMCVD [Mor99].

The MOVPE is characterized by large-area growth capability, high surface mobility of the precursor gaseous molecules, good layer uniformity and precise control of the epitaxial deposition. These reasons together with the higher growth rate, made the MOVPE to be the favourite growth method for industrial purposes. By this technique, the gas phase growth precursors are transported by a carrier gas to a heated substrate, where the precursors are pyrolysed and the nitride film is deposited. The diffusion of the active materials to the substrate are favored by the depletion at the surface and the consequent concentration gradient of these materials in the gas phase, due to their consumption during the growth. The obtained byproducts are then transported out from the reactor together with the unused reactants. As group III sources, trimethylgallium or triethylgallium (-indium,-alluminium) are used, whereas the common nitrogen source is ammonia (NH_3). The high thermal stability of NH_3, although still low compared to N_2, is one reason to use high substrate temperatures, typically more than 550°C for InN and above 900°C for GaN and AlN. The high growth temperature and thus the high nitrogen vapor pressure lead to the problem of nitrogen loss from the nitride film and to carbon contamination from the decomposition of the organic radical during metalorganic pyrolysis. The loss of nitrogen is usually alleviated by the use of high V/III gas ratios during the deposition. The extreme requirements for the nitride growth have led also to the development of new MOVPE reactor designs.

The GaN Gunn diode structures, considered in this thesis, have been grown by MOVPE in an Aixtron AIX200 reactor on two inch Al_2O_3 substrates. Unlike the MBE system, RHEED is not suitable for in-situ monitoring of the growth rate in the high-pressure environment like MOVPE. RHEED requires a high electron mean free path, which can be achieved only in ultra high vacuum conditions. The growth rate is therefore determined by normalized reflectometry. A more accurate description of the MOVPE epitaxy and the experimental setup can be found in [Kal03].

3.5 GaN Gunn diode structures

During this work, four GaN wafers have been considered: G102, G394, G582, G695. The first 3 wafers are uniformly doped; they have been used to optimize the ECR-RIE process and to produce GaN nanocolumns; the GaN layers are about 4, 2.2, and 4 μm thick, respectively. The layer sequence of a GaN Gunn diode is sketched in Fig. 3.9. It is a typical Gunn diode without injector and δ-doping. It consists of a high doped 800 nm thick contact layer, followed by a 1600 nm low doped active region and by another high doped 200 nm thick contact layer. The typical surface morphology for the grown GaN Gunn wafer is shown in Fig. 3.10. The surface roughness for the $2 \times 2\mu m^2$ AFM scanned area is about 0.3 nm. This is a good result for GaN.

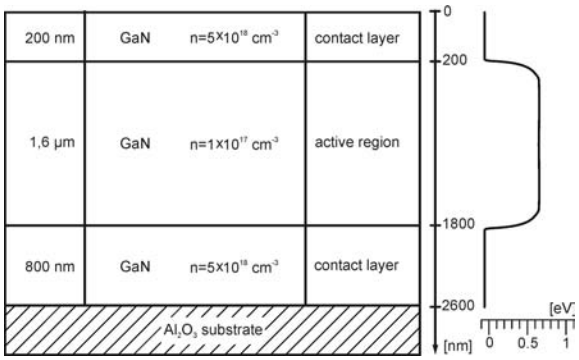

Figure 3.9: Layer sequence of the GaN Gunn diode.

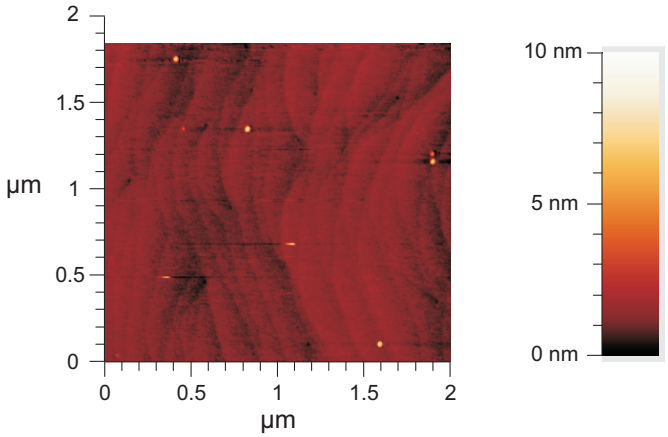

Figure 3.10: AFM image of the surface morphology for GaN Gunn structure (wafer G695).

Chapter 4

Experimental Methods

4.1 Atomic Force Microscope (AFM)

Atomic Force Microscopy technique provides three-dimensional surface topographies at nm resolution of a wide range of solid materials (conducting, insulating, magnetic). The basic principle is simple: a sharp tip scans the sample surface detecting the topography. Typical Si_3N_4 tips have a curvature radius of 10-15 nm and opening angle of about 20°. When the tip is brought very near to the surface to be analyzed, it undergoes attractive or repulsive forces. The cantilever, on which the tip is located, is deflected. An optical amplification system measures the tip movements. Figure 4.1 shows the system working principle: a laser beam points on the cantilever and four photodiodes in a cross configuration detect the reflected beam. While the sample is scanned, the tip-sample interaction is kept constant by feedback.

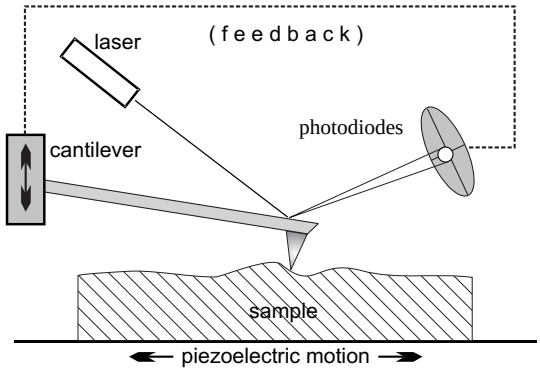

Figure 4.1: Schematic description of the operation principle of the AFM. The feedback loop (a compensation network or a computer program) monitors the cantilever deflection and keeps it constant by adjusting the vertical position of the cantilever.

Atomic Force Microscope has gone through many modifications for specific application

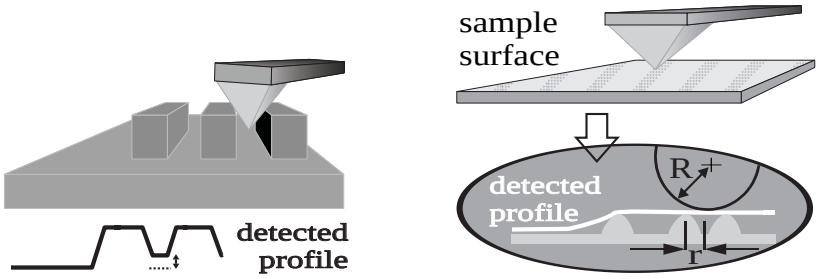

(a) (b)

Figure 4.2: Errors deriving from surface geometry (a) and tip geometry (b) during AFM characterization.

requirements. There are several AFM operating modes: *contact mode*, *tapping mode*, *phase imaging mode*...

The first and foremost mode of operation, the *contact mode*, is very similar to a profilometer: the tip-sample forces are maintained at a constant level and with piezoelectric motion, the surface is scanned by the tip.
The *tapping mode*, belongs to a family of AC modes, which refers to the use of an oscillating cantilever. The tip intermittently *touches* or *taps* the surface. The natural resonance frequency is shifted by the tip-sample force. The shift is proportional to the second derivative of the corresponding potential. This information is then converted in a topographical image of the surface. In order to filter out the thermal noise, a lock-in amplification is introduced and a more stable detection is allowed.
In *phase imaging mode*, the phase shift of the oscillating cantilever relative to the driving signal is measured. This phase shift can be correlated with specific material properties, which affect the tip/sample interaction.

The forces acting between the tip and the surface are of different nature and depend on the tip-sample distance. The first interaction is the electrostatic force. It begins at $0.1 - 1\ \mu m$ and may be either attractive or repulsive depending on the material. At $10 - 100\ nm$, surface tension effects result from the presence of condensed water vapor at the surface. The tip is pulled down toward the sample surface with attractive force up to $200\ pN$. Van Der Waals forces appear at the angstrom level above the surface: the atoms in the tip and sample undergo a weak attraction. Coming even closer, electron shells from atoms on both tip and sample repulse one another, preventing further intrusion by one material into the other (Coulomb forces, *contact mode*). Pressure exerted beyond this level leads to mechanical distortion and the tip or the sample may be damaged.

The actual sharpness of a tip influences directly its ability to resolve surface features. Moreover, certain tip damages (e.g. double-pointed and cracked tips) occur very often. In Fig. 4.2, the tip-sample geometry and interactions are considered. One obvious surface limitation is caused by deep grooves (Fig. 4.2(a)): the tip is not long enough, or thin enough, to reach the bottom of a recess. Furthermore, the tip cannot detect walls of the sample with an angle steeper than itself.

More errors are introduced by the tip geometries: consider a Si_3N_4 tip with a radius R measuring a series of parallel objects of radius r (Fig. 4.2(b)). As R increases, it decreases the ability of the tip to identify the radius r and to resolve the separation of the objects.

4.2 Scanning Electron Microscope (SEM)

Conventional light microscopes use a series of glass lenses to bend light waves and create a magnified image. The Scanning Electron Microscope handles electrons instead of light waves. The resolution of an optical microscope is limited by the wavelength of the used light. For an electron microscope, the wavelength λ from deBroglie is:

$$\lambda = \frac{h}{\sqrt{2mW}} = \frac{h}{\sqrt{2meV}} , \tag{4.1}$$

where h is the plank constant, m the electron mass and $W = eV$ is the kinetic energy of the electrons. For typical voltages between 5 and 20 kV, the wavelength is between 0.16 and 0.08 Å. These resolutions are very optimistic: the actual resolving power of a SEM is mainly depending on the apparatus. During this work, the scanning electron microscope Leo 982 has been used. It is equipped with the GEMINI field emission column providing typical resolutions of 4nm at 1kV, up to 1nm at 30kV.

After the air is pumped out from the column, an electron gun (at the top) emits a beam of high energy electrons. Four different sources can be used [Was03]: tungsten filament, LaB_6 crystal tip, Schottky emitter and the cold field emitter. In ultra-high vacuum conditions ($< 10^{-9}$mbar), the best beam properties are supplied by cold field emitter. Schottky emitter is a good compromise between performance and costs.

The electron beam travels downward through a series of magnetic lenses designed to focus the electrons to a very fine spot. Near the bottom, a set of scanning coils deflect the focused beam back and forth across the specimen, row by row. The SEM images are normally rendered black and white.

Samples have to be prepared carefully to withstand the vacuum inside the microscope. Biological specimens are dried in a special way, which prevents them from shrivelling. Because the SEM *illuminates* them with electrons, they also have to be made to conduct electricity. Often SEM samples are coated with a very thin layer of gold by sputtering deposition.

4.3 Hall measurements

The Hall effect measurement is a widely-used technique to determine electrical properties of semiconductors like majority carrier type, concentration and mobility. The Hall effect is based on the deflection by a magnetic field of moving charged particles.

In Figure 4.3, a rectangular sample has been considered. A voltage V_x and a magnetic field B_z are applied. Electrons and holes flowing in the semiconductor will experience a force, bending their trajectories, and they will build up on one side of the sample, creating a potential V_H across it (the so-called *Hall voltage*). Assuming that all the conduction

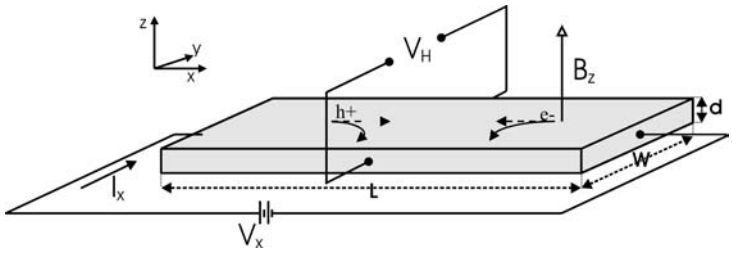

Figure 4.3: Sign convention and terminology for a rectangular Hall sample.

electrons have the same drift velocity $\overrightarrow{v_n}$ and the same relaxation time τ_c, the resulting Lorentz force acting on any electron is given by:

$$\overrightarrow{F} = -q(\overrightarrow{\mathcal{E}} + \overrightarrow{v_n} \times \overrightarrow{B}) \tag{4.2}$$

$$\overrightarrow{F} = m_e \frac{d\overrightarrow{v_n}}{dt} + m_e \frac{\overrightarrow{v_n}}{\tau_c} , \tag{4.3}$$

where $m_e\overrightarrow{v_n}/\tau_c$ is a damping term accounting for the scattering. In the steady state, the derivative of $\overrightarrow{v_n}$ in equation 4.3 is zero. Combining equations 4.2 and 4.3 and using the relation $\overrightarrow{J} = -qn_0\overrightarrow{v_n}$ for electrons, we get:

$$\overrightarrow{\mathcal{E}} = \frac{\overrightarrow{J}}{q\mu_n n_0} + \frac{\overrightarrow{J}}{qn_0} \times \overrightarrow{B} , \tag{4.4}$$

where $\mu_n = q\tau_c/m_e$ is the mobility. Considering $B_x = B_y = 0$ and $J_y = J_z = 0$, the vector equation 4.4 can be written as two scalar equations:

$$\mathcal{E}_x = \frac{J_x}{\sigma} \tag{4.5}$$

$$\mathcal{E}_y = -\frac{J_x B_z}{qn_0} = -\mu_n B_z \mathcal{E}_x , \tag{4.6}$$

where $\sigma = q\mu_n n_0$ is the conductivity and relation 4.5 is just the Ohm's law. Equation 4.6 expresses the fact that, along the y direction, the force on one electron due to the magnetic field ($q\mu_n B_z \mathcal{E}_x$) is balanced by a force ($-q\mathcal{E}_y$) due to the Hall field. (Eq. (4.6)) is generally written as

$$\mathcal{E}_y = R_H J_x B_z , \tag{4.7}$$

where $R_H = -\frac{1}{qn_0}$ is called the Hall constant. For a p-type semiconductor, it can be shown that

$$\mathcal{E}_y = R_H J_x B_z = \mu_p B_z \mathcal{E}_x \tag{4.8}$$

with $R_H = \frac{1}{qp_0}$, where p_0 is the equilibrium concentration of holes in the sample. It is thus seen that R_H has a negative sign for electrons and a positive sign for holes.

From 4.7, for a rectangular bar like in Fig. 4.3, the Hall constant and the Hall mobility can be expressed by:

$$R_H = \frac{V_H d}{I_x B} \tag{4.9}$$

$$\mu_H = \frac{L}{W}\frac{V_H}{V_x B}\,, \tag{4.10}$$

where V_H is the measured Hall voltage, V_x is the applied voltage along the length L, and I_x is the current. For a semiconductor with comparable concentrations of electrons and holes, R_H is given by

$$R_H = \frac{(\mu_p^2 p_0 - \mu_n^2 n_0)}{q(\mu_p p_0 + \mu_n n_0)^2} \tag{4.11}$$

and the interpretation of R_H and μ_H is difficult. But if the material is strongly extrinsic, the relation (4.11) for a highly n-doped material reduces to

$$R_H = -\frac{1}{q n_0} \qquad \text{and} \qquad \mu_H = \mu_n \tag{4.12}$$

and for a highly p-doped one to

$$R_H = \frac{1}{q p_0} \qquad \text{and} \qquad \mu_H = \mu_p \tag{4.13}$$

In these two cases, the measurement of R_H and μ_H determines the majority carrier concentration and the mobility, respectively.

The simplest arrangement for measuring the Hall voltage is the rectangular geometry shown in Fig. 4.3, but a number of spurious voltages is included in this measurement. All these spurious voltages are eliminated if four readings are taken by reversing the direction of the bias current I_x and the magnetic flux B. The true Hall voltage is then obtained by taking the average of the four readings. The contacts used for measuring the Hall voltage in Fig. 4.3 should be infinitesimally small, so that they do not distort the current flow. The bridge shaped samples shown in Fig. 4.4(a) are often used to reduce the distortion of the current. The ears on the pattern allow a large area to be used for contacting the sample without a severe distortion of current flowing through the specimen. The Hall voltage is measured between contacts 1 and 2, and then between 3 and 4. The average is taken as a final value.

In some cases, it may not be convenient to cut the specimen in the form of a rectangular bar. Van der Pauw [vdP58] suggested an interesting method, using an arbitrary shaped thin-flat sample. The above sample (simply connected, i.e., no holes or non-conducting islands or inclusions), contains four very small ohmic contacts placed on the sample periphery (preferably in the corners). In presence of a normal magnetic field to the sample surface, a current I_{ac} is established between two opposite contacts (a and c), and the voltage is measured between the other ones (b and d), as shown in Figure 4.4(b).

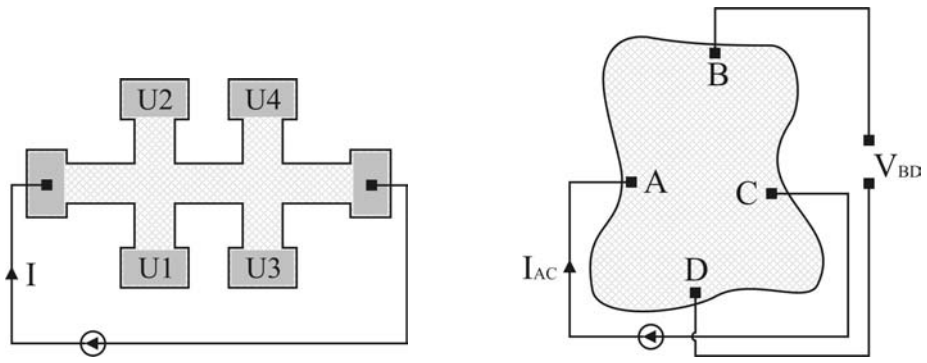

(a) A bridge-shaped Hall sample with two pairs of ears contacts.

(b) Van der Pauw arrangement for an arbitrary shaped sample.

Figure 4.4: Hall measurement contact configurations and layouts

The resistance, defined as:

$$R_{ac,bd} = \frac{V_{bd}}{I_{ac}} \tag{4.14}$$

is first measured with the magnetic field B, $R_{ac,bd}(+B)$ and then with the opposite field $-B$, $R_{ac,bd}(-B)$. If all the possibilities concerning the current and magnetic field polarity are considered, then the Hall constant is given by:

$$\begin{aligned} R_H \quad = \tfrac{d}{8B}(\quad & R_{ac,bd}(+B) - R_{ac,bd}(-B) + R_{bd,ac}(+B) - R_{bd,ac}(-B) \\ & + R_{ca,db}(+B) - R_{ca,db}(-B) + R_{db,ca}(+B) - R_{db,ca}(-B)) \end{aligned} \tag{4.15}$$

4.4 Capacitance-Voltage measurements

A different way to determine the background concentration N_d of carriers in a semiconductor, is the capacitance-voltage (C-V) measurement. The C-V method relies on the fact that the width of a reverse biased space charge region of a junction depends on the applied voltage. The space charge Q_{sc} per unit area of the semiconductor junction under an applied bias V is:

$$Q_{sc} = qN_dW = \sqrt{2q\epsilon_s N_d \left(V_{bi} - V - \frac{kT}{q}\right)}\,, \tag{4.16}$$

where W is the depletion layer width defined in Eq. (2.51) and V_{bi} is the built in potential defined in Eq. (2.49) (section 2.2.1). The depletion layer capacitance per unit area is given by:

$$C = \frac{|\partial Q|}{\partial V} = \sqrt{\frac{q\epsilon_s N_d}{(V_{bi} - V - \frac{kT}{q})}} = \frac{\epsilon_s}{W}\,. \tag{4.17}$$

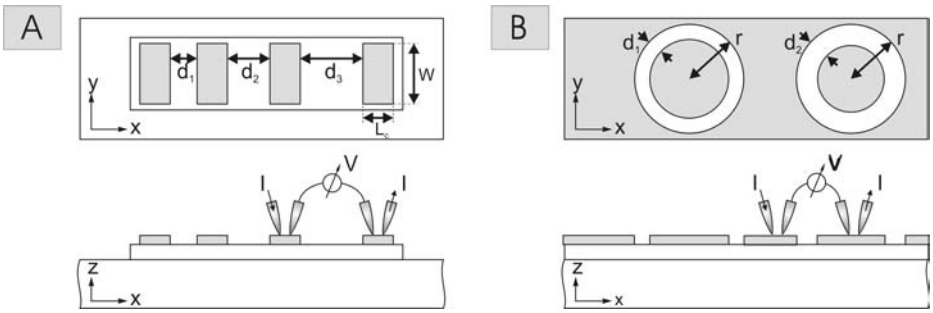

Figure 4.5: Contact resistance test patterns. (a) TLM and (b) CLM configuration.

Equation 4.17 can be written in the form

$$\frac{1}{C^2} = \frac{2(V_{bi} - V - \frac{kT}{q})}{q\epsilon_s N_d} \tag{4.18}$$

$$-\frac{d(1/C^2)}{dV} = \frac{2}{q\epsilon_s N_d} \tag{4.19}$$

$$N_d = -\frac{2}{q\epsilon_s \frac{d(1/C^2)}{dV}} \tag{4.20}$$

$$W = \frac{\epsilon_s}{C}\,. \tag{4.21}$$

In the case of uniform doping concentration, N_d is constant within the depletion region and a strait line should be obtained by plotting $1/C^2$ versus V. The intercept on the X-axis of the line represents V_{bi}, the built-in potential[1]. If N_D is not constant, the doping profile can be determined from the slope of the curve and equation 4.20.

4.5 TLM and CLM

The ohmic contacts are of great importance in relation with the quality and the reliability of the microelectronic devices. The resistance of an ohmic contact can be evaluated by the transmission line method (TLM). The TLM structure is a series of identical contact pads, of width w and length L_C, spaced at varying intervals d_1, d_2, d_3, ... (Fig. 4.5A). The TLM structure requires an additional mesa etching, in order to restrict the current flow only between the contact pads, along the x direction (with the convention of Fig. 4.5A). A similar technique, the circular transmission line method (CLM) does not require additional mesa etching: the current confinement in the direction perpendicular to the contact is obtained with concentric circular contacts (Fig. 4.5B). In both cases, to avoid the eventual influence of external series resistances, a four point measurement (Kelvin method) is suggested: two probes carry the current and two probes sense the

[1]From Eq. (4.18), if $V = V_{bi}$ ideally $1/C^2 = 0$

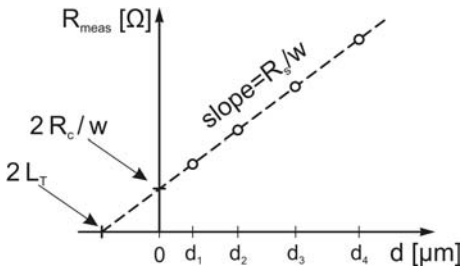

Figure 4.6: Evaluation of the contact and sheet resistances for TLM measurements.

voltage. The expression of the measured resistance between two contacts separated by the distance d_i is:

$$R_{meas} = R_C \cdot X + R_S \cdot Y \ , \tag{4.22}$$

where $R_C\,[\Omega\,mm]$ is the contact resistance, $R_S\,[\Omega/\Box]$ is the sheet resistance of the semiconductor, and X and Y depend on the geometry of the contact. For a TLM structure, we have:

$$X = \frac{2}{w} \tag{4.23}$$

$$Y = \frac{d_i}{w} \tag{4.24}$$

and for a CLM structure, it results:

$$X = \frac{1}{2\pi} ln\left(\frac{1}{r} + \frac{r}{r-d_i}\right) \tag{4.25}$$

$$Y = \frac{1}{2\pi} ln\left(\frac{r}{r-d_i}\right) \ . \tag{4.26}$$

In Fig. 4.6, the measured resistances are plotted as a function of the distance d_i. Fitting Eq. (4.22), the values of R_S and R_C can be obtained. Then, the specific contact resistance, $\rho_c\,[\Omega\,cm^2]$ is given by:

$$\rho_C = \frac{R_C^2}{R_S} \ , \tag{4.27}$$

and the transfer length L_T (also known as effective contact length) is:

$$L_T = \frac{R_C}{R_S} \ . \tag{4.28}$$

It can be noticed that the intercept with the x-axis of the fitted line in Fig. 4.6 is twice L_T. For the validity of the above analysis, one assumption has been made: the transfer length L_T must be much smaller than the contact length L_C [MD82].

4.6 Short pulse DC measurements

Mainly the DC measurements have been carried out using a Curve Tracer Sony-Tektronix 370A. Additionally to this, a driver transistor has been included in the circuit, so that 80 μs pulse measurements could be possible. The measurement setup is shown in Fig. 4.7(top). The circuit of the setup operates as following: the base output of the Curve Tracer operates in pulse mode and drives the base of an external control transistor with current pulses of 1mA. The Collector output (voltage supply) is connected to the Gunn diode and then the circuit is closed through the control transistor. To avoid the eventual influence of external series resistance, a four point measurement (Kelvin method) is used. The Gunn diode chip is connected to the measurement circuit, using micro-manipulators with Au needles. The measurement table has a heater, which permits I-V characteristics measurements in a temperature range from room temperature till 200°C.

The study of the breakthrough voltage without damaging the Gunn diode requires DC measurements with very short pulses ($\ll 80\ \mu s$). Moreover, with different pulse length, the influence of the diode selfheating on the I-V characteristics can be determined. For these two reasons, a 100 ns measurement setup has been designed and realized [Pro04]. The principle scheme of the measurement set-up is presented in Fig. 4.7(bottom).

100 ns pulses are generated from a low-power pulse generator and are amplified by a custom-designed printed circuit board (PCB), powered by a computer controlled DC power supply. The pulses are forwarded to the terminal of the diodes. The short pulse length requires a special attention in the terminal connection, in order to avoid line reflections. Therefore, on-wafer measurements are performed with HF picoprobes. For the packaged diodes, a further custom adaptor is connected directly to the PCB. The voltage drop on the diode and on a known serial resistance within the PCB are measured with a digital oscilloscope. The serial resistance voltage drop is proportional with the current flowing through the diode. The sweep range of the voltage pulse can be tuned from 0 V up to 20 V and the current is limited to 3 A. A HP-VEE program running on a PC controls the measurements through a IEEE488 interface bus and computes the diode DC characteristics from the oscilloscope raw data.

4.7 S-parameters measurements

4.7.1 Network Analyzer Measurement systems

Network analyzers characterize accurately components by measuring their effects on the amplitude and phase of swept-frequency and swept-power test signals. Network analysis satisfies the engineering need to characterize the behavior of passive and active components quickly and accurately over broad frequency ranges.

Most of the devices used to collect data for this work, have been measured from 500MHz up to 110GHz, with 201 frequency steps. The S-parameters measurements need to be performed over appropriate bias range. The bias voltage should be varied

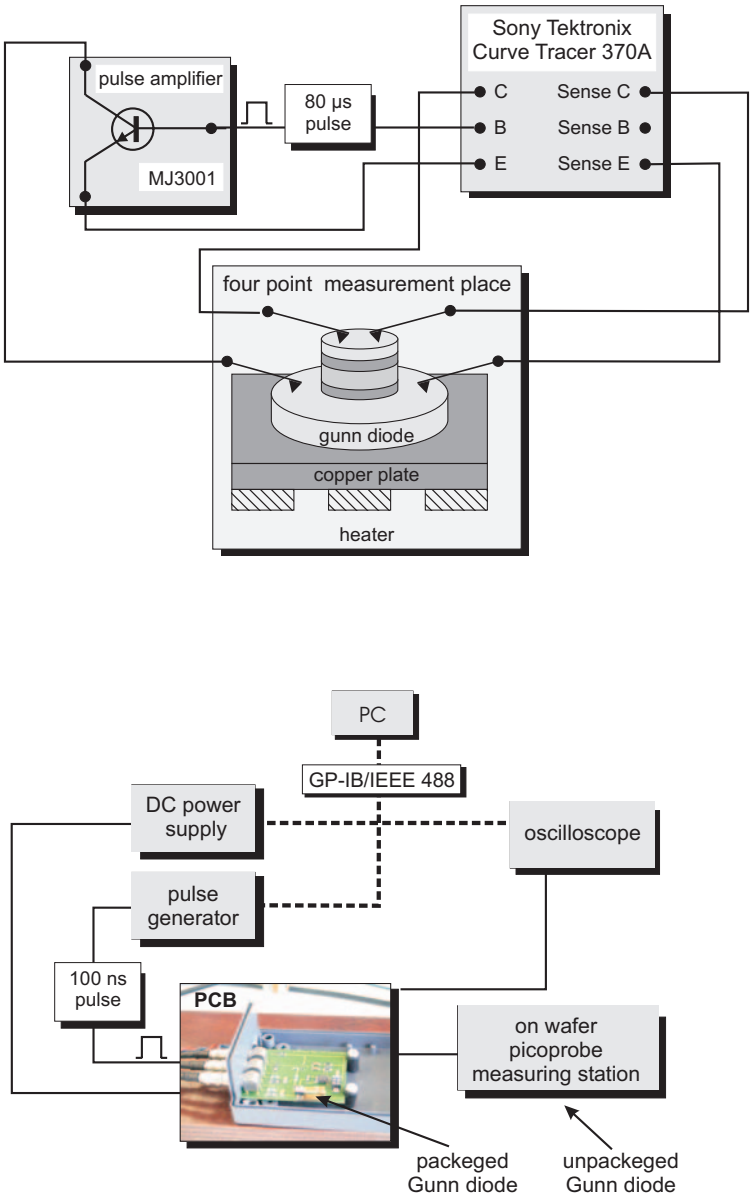

Figure 4.7: Measurement setup for continuous and pulse (80 μs) DC measurements with heating possibilities from room temperature till about 200 °C (top). Measurement setup for very short pulse (100 ns) DC measurements (bottom).

from negative to positive values, linearly increasing up to 5 or 8 V (depending on the breakdown voltage of the device).

Temperature dependent measurements have been more complicated and time consuming: they have required to build a compact custom-made temperature controller based on a peltier element and a PT100 thermosensor. The temperature is function of the resistance of the PT100, which is embedded in a flat copper block. The peltier element cools or heats (depending on the terminal polarity) the copper block, transferring the heat to or from a big metal reservoir, kept at room temperature. In the considered setup, the sample is fixed with vacuum on the copper block and the temperature can be tuned from 2 °C up to 80°C. Lower temperatures can not be reached because of ice formation and higher ones could damage the HF picoprobes.

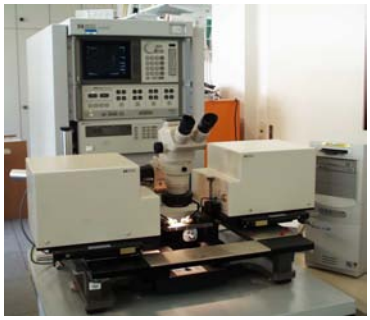

Figure 4.8: Vector network analyzer HP8510C (8510XF)

When making on-wafer measurements, an ongoing concern is how accurate and repeatable are the collected data. The hardware has to be as good as practically possible, balancing performance and costs; **error corrections** can be an useful tool to improve measurement accuracy. The basic source of measurement errors are:

Systematic errors: due to imperfection in the analyzer and test setup. They are repeatable (and therefore predictable) and are assumed to be time invariant. Systematic errors are determined during the calibration process and they are used for corrections during the measurements.

Random errors: unpredictable, since they vary in a random fashion. Therefore they cannot be removed by calibration. The main contributors to random errors are source phase noise, sampler noise and IF noise.

Drift errors: are due to the instrument or test-system performance changing after the calibration has been done. The main cause is temperature variation and can be removed by further calibrations and/or providing a stable ambient temperature.

Before a network analyzer can make error-corrected measurements, the network analyzer systematic errors must be measured and removed. Calibration is the process of quantifying these errors by measuring known precision standards. Three techniques are commonly used to calibrate network analyzers and wafer probing stations:

Short Open Load Through (SOLT) is a two-port calibration, typical for coaxial transmission medium. It uses a short, an open and a load at each port as impedance standard to measure reflection errors. A through standard measures the frequency response tracking. A load match and an open signal path measure the isolation between ports [Gol91]. With non-coaxial transmission medium, the calibration standards of the SOLT is difficult to fabricate.

Through Reflect Line (TRL) is a two-port calibration, which requires a through connection, a reflection standard, and a reference transmission line. It uses calibration standards, which are easily fabricated and characterized; for this reason, it is preferred for non-coaxial environment.

Line Reflect Match (LRM) is a two-port calibration similar to TRL. Instead of TRL, it is based on fixed loads and not transmission line(s), as reference impedance. LRM is a particularly convenient broadband calibration for non-coaxial environments with accuracy as good as TRL.

The LRRM[2], a variation of LRM, was used for most of the measurements with the HP8510C-XF vector network analyzer in Figure 4.8; it was usually software assisted by WinCal, a program developed by Cascade Microtech, which supplied also the picoprobes and the probing station.

4.7.2 Displaying data: Smith Chart

During HF measurements and after data has been collected, it is essential to have an overview over the produced results. The fastest way is to display data with some kind of graphical interfaces (normally integrated in the measurement system or in a software package for computer controlled measurement systems). The most popular diagram for each parameter are:

- Magnitude and Phase amplitude Chart,
- Polar Chart,
- Smith Chart[3] (Fig. 4.9).

Smith chart represents the standard for S_{11} and S_{22}, while polar chart is more used for S_{12} and S_{21}. Magnitude and Phase amplitude chart can be used for all S-parameters. Assuming that the concepts of magnitude and phase amplitude chart and of polar chart are clear to the reader, Smith chart is defined in the followings. To simplify the analysis two assumptions are made:

1. the transmission line is essentially lossless[4], meaning that the characteristic impedance is entirely real;
2. the load impedance Z_L is normalized to the characteristic impedance Z_0[5].

The Smith Chart is derived from the relationship between complex reflection coefficient Γ and complex impedance Z.

$$\Gamma = \frac{Z-1}{Z+1} \tag{4.29}$$

[2]Line Reflect Reflect Match: it requires calibration standards kits with loads, shorts and through
[3]The Smith Chart was developed by Phillip H. Smith in 1937 to ease his RF design work in Bell Labs.
[4]Most transmission lines have losses low enough for this assumption to hold.
[5]The Smith Chart relies on normalized impedances.

Writing the impedance and the reflection coefficient as function of the real and imaginary components, $Z = r + jx$ and $\Gamma = \Gamma_r + j\Gamma_i$, equation 4.29 is equivalent with:

$$r = \frac{1 - \Gamma_r^2 - \Gamma_i^2}{(1 - \Gamma_r)^2 + \Gamma_i^2} \tag{4.30}$$

$$x = \frac{2\Gamma_i}{(1 - \Gamma_r)^2 + \Gamma_i^2} \, . \tag{4.31}$$

To actually see the form of the equations for deriving the Smith Chart, we rearrange the terms to obtain the equations for a set of circles:

$$\left(\Gamma_r - \frac{r}{1+r}\right)^2 + \Gamma_i^2 = \left(\frac{r}{1+r}\right)^2 \tag{4.32}$$

$$(\Gamma_r - 1)^2 + \left(\Gamma_i - \frac{1}{x}\right)^2 = \left(\frac{1}{x}\right)^2 \, . \tag{4.33}$$

From equations 4.32 and 4.33 the Smith Chart can be easily drawn. Some key features of this chart (Fig. 4.9) are listed:

- The horizontal axis through the origin represents all purely resistive impedance.
- The outermost rim represents all purely reactive impedances.
- We can see a family of circles: each of them is a constant resistance set of points.
- We can see a family of arcs: each of them is a constant reactance set of points.

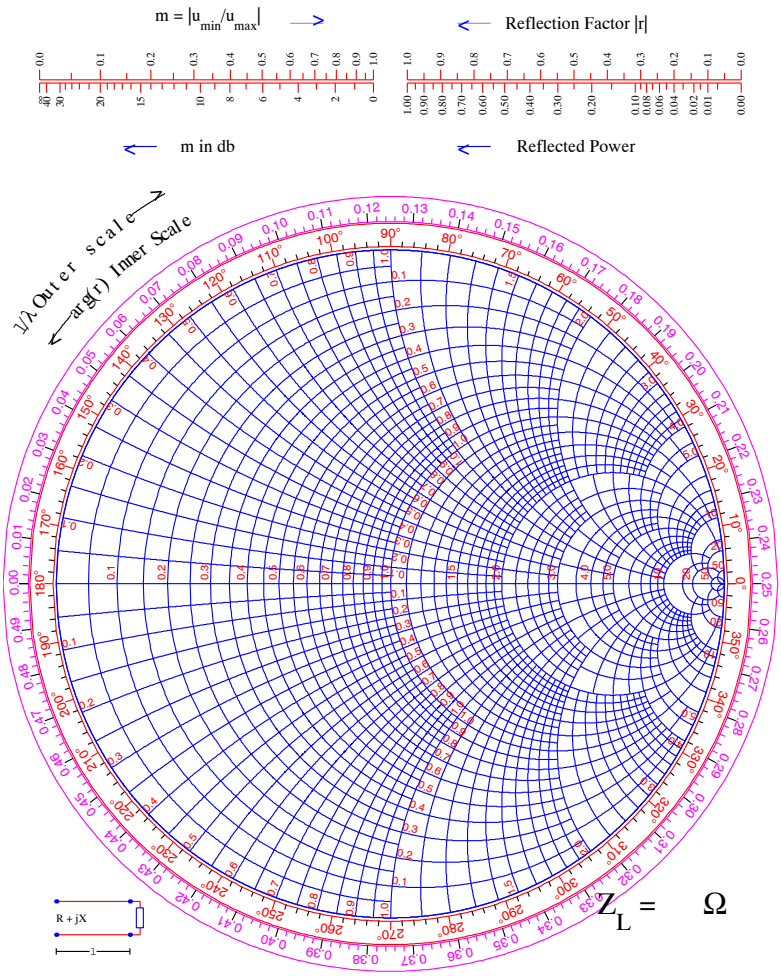

Figure 4.9: Smith Chart

Chapter 5

Technology

In this chapter, the processing flow and the technological procedures involved in the fabrication of planar Gunn devices, are presented in detail. The first technological stage, the epitaxial growth of the device structure, has been already described in chapter 3, referring to MBE and MOVPE systems. After the epitaxial growth, the 2-inch wafers were cleaved or sawed. The complete processing was carried out on 1×1 cm samples. The next sections deal with the steps required for the device fabrication:

1. mesa definition and etching;
2. self aligned ohmic contacts deposition and annealing;
3. diode electrical isolation etching down to the semi-isolating substrate;
4. diode planarization / passivation;
5. bond-pads, low-pass filter and resonant circuit deposition;
6. plated air-bridge fabrication (optional).

The air-bridge interconnection (step 6) represents an alternative to the device planarization (step 4). In the last case, the top diode contact is electrically connected making a ramp with an isolating material (polyamid planarization); in the first case, a thick gold bridge is fabricated. The higher effort in the case of air-bridges, is balanced by a better cooling of the device from the top side (see section 2.4) and by a lower fault rate due to the thicker interconnection lines.

Depending on the compound semiconductor type (GaAs and GaN), each step requires a particular approach. The differences between the adopted solutions for GaAs and GaN will be discussed. A detailed list of the process parameters can be found in appendix C.

5.1 Mesa etching

The Gunn diode mesa etching is the first step of the developed processes. Three semiconductor layers are removed around the mesa: top contact, injector (if available) and active region. After the etching, the semiconductor surface is supposed to be 200 nm inside the

bottom contact layer. A detailed description of the considered layer structures is given in chapter 3. Including 100 nm tolerance, the required mesas heights are between 2.3 and 2.8 μm.

For the mesa etching of a Gunn diode, two possibilities are available: dry Reactive Ion Etching (RIE) and wet chemical etching. Dry etching has been chosen, because it allows an exact definition of the mesa[1], prevents unwanted under-etch and provides smooth and nearly vertical side-walls. For both GaAs and GaN mesas, a chlorine based gas mixture is preferable. The demand of deep mesas requires high etch rates. Chlorine based plasmas are highly aggressive for Ga-based III-V semiconductor, because the chloride Ga_2Cl_6 is highly volatile [PRA94]. The use of methan is not indicated for two reasons: the CH_4/H_2 process presents low etch rates and there is the risk of formation of solid gallium carbide. The considered etching process ECR (Electron Cyclotron Resonance) -RIE was proposed by Kaindl at al. [KSF95] and by Franz et al. [Fra94, FR99]. The ECR-RIE has been carried out in a Oxford Plasmalab System 90 equipment. The working principle of ECR is based on the electron cyclotron frequency:

$$\omega_c = \frac{eB}{m_e}. \tag{5.1}$$

In the ECR chamber, the gas mixture is situated between two magnets, providing a static magnetic field B. In Eq. (5.1) e is the electron charge and m_e is the electron mass. The plasma is excited by a microwave field in the presence of the magnetic field of the correct magnitude to cause the electrons to spiral at the microwave frequency ω_c, thus increasing the probability of ionization. The current flowing in the upper magnet is 185 A, while the one flowing in the lower magnet is 25 A. The both magnets contribute to realize the resonance condition; tuning the lower magnet current the thickness of the ECR layer (accelerating layer) can be changed: the corresponding the plasma density influences the etch rate and uniformity [PRA94]. Once the plasma is stable under a constant pressure of 2 μbar, the etching process begins applying a R.F. power of 50-60 W. The RF signal causes a bias difference between the top and the bottom part of the ECR chamber and directs the plasma towards the lower part, where the etching takes place. The main advantage of ECR-RIE is the separation of the plasma generation region from the one where the sample is etched. In this way, the sample can be etched smoothly, reducing the crystal defects induced by the process.

5.1.1 ECR-RIE of GaAs/AlGaAs mesa.

Before starting the real etching, the ECR chamber is cleaned with O_2 plasma for 30 minutes and with H_2/Ar plasma for 10 minute. The oxygen based process removes the eventual polymers in the chamber and the hydrogen one neutralizes the oxygen residuum.

The chosen conditions for the GaAs dry etching are listed in appendix C.4 and are inspired from the optimization work of Stock [Sto03]. The mesa area is defined evaporating Ti patterns as etching masks. After the Ti lift-off, an oxygen plasma treatment removes

[1]The area of the mesa is proportionally related to the diode maximum current. The inaccuracy in defining the diode mesa prevents the fulfilment of the design specification.

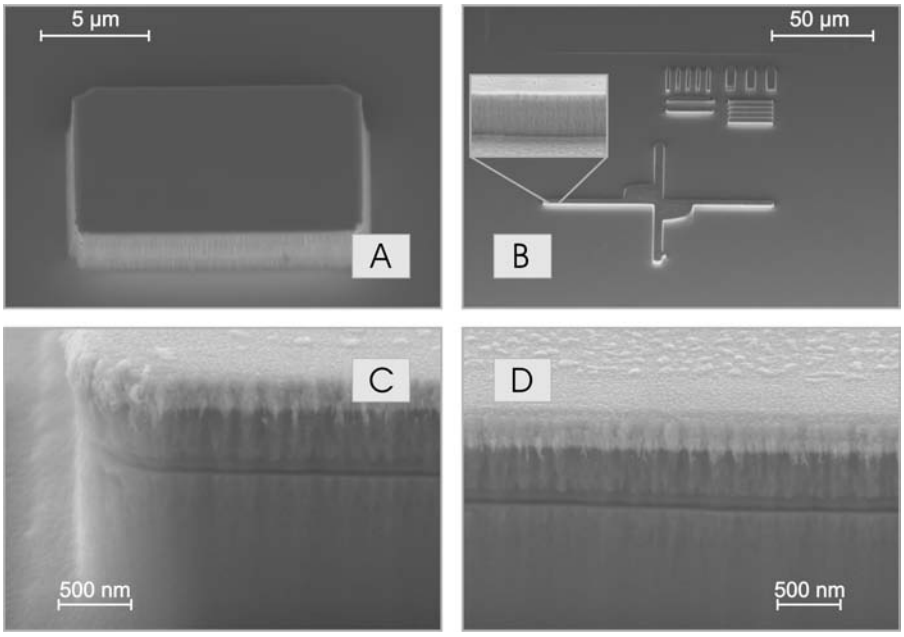

Figure 5.1: SEM pictures of the GaAs Gunn diode mesas after ECR-RIE etching in $Cl_2/H_2/Ar$ Plasma.

possible resist traces. Now, it is possible to start the ECR-RIE with a $Cl_2/H_2/Ar_2$ gas mixture. The etch-rate is between 350 and 450 nm/min, depending on the sample temperature, gas pressure and RF power. The etch-rate has been monitored sampling the etched thickness with a Dektak profilometer. The selectivity of the plasma process between the Ti masks and the GaAs sample is 1:8.

In Fig. 5.1, SEM pictures of the etched GaAs samples are presented. A typical mesa of a graded gap injector Gunn diode and an alignment mark pattern are shown in Fig. 5.1A and B, respectively. The shape of the Ti mask is perfectly reproduced, no under-etch is present and the sidewalls are smooth and vertical. After the plasma process, the Ti mask is easily removed in a hydrofluoric acid (HF) buffered solution (AF91). HF is not aggressive for GaAs or AlGaAs if the Al concentration is under 35%. In Fig. 5.1C and D, a thin horizontal line can be noticed in the sidewalls. The diodes in pictures C and D, in fact, have a double AlAs thin layer (resonant tunneling injector). The thin line originates from the under-etch of the two AlAs layers, during the Ti removal. The under-etch does not represent a serious threat for the device: considering a under-etch of about 30 nm and a diode area of about 400 μm^2, the estimated change in the current is lower than 0.1% .

5.1.2 ECR-RIE of GaN mesa

Before the mesa-etching, the ECR-RIE chamber is cleaned, as described in section 5.1.1. Then, to the GaN sample, a gas mixture of Cl_2/Ar is applied. In comparison with the GaAs process, here hydrogen is not used. For GaAs, hydrogen plays a moderator role, it reduces the etch-rate and provides smooth surfaces [vH95]. However, for GaN, the etch-rate is considerably lower and there is no need of hydrogen. Concerning the GaN surface morphology, the effect of hydrogen can not be noticed. Hydrogen is still used to start the plasma, but it is not present anymore during the etching process.

The mask choice for the GaN ECR-RIE was a difficult task. It has already been shown that using a thin Ti mask and etching with $Ar/CH_4/H_2/Cl_2$ plasma result in an inhomogeneous etch profile, with spikes [Jav03]. In our test with Cl_2/Ar gas mixture, the selectivity between Ti and GaN was low and significant redeposition next to the mesas has been observed. Resist and Si_3N_4 masks have been tried without much success. Good results appeared, only, with a mask of evaporated nickel. Figure 5.2A shows an etched GaN mesa before the Ni removal. The walls are perfectly vertical and smooth. The morphology of the etched surface is not regular: GaN spikes cover the whole etched surface. Figure 5.2B presents a better morphology obtained after tuning the etch-process: the chamber pressure has been decreased and the proportions between argon and chlorine have been modified. The remaining spikes can be eliminated by argon sputtering.

5.1.3 GaN nanocolumns: a topdown approach.

During our early tests, it was discovered that Ti could favor the spikes and support the generations of nanocolumns on GaN. The 350 Ti mask is etched in circa 6-7 minutes with a rate of 50-60 nm/min. The Ti micro-masking effect has been amplified by changing the gas relations between argon and chlorine and the microwave power.

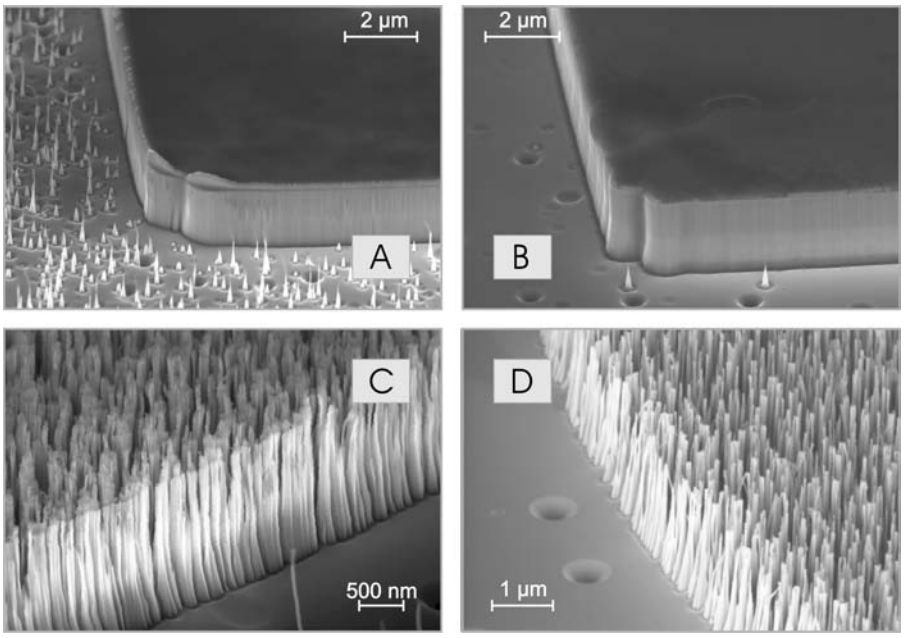

Figure 5.2: SEM pictures of the GaN Gunn diode mesas after ECR-RIE etching in Cl_2/Ar Plasma and nanocolumns appearance.

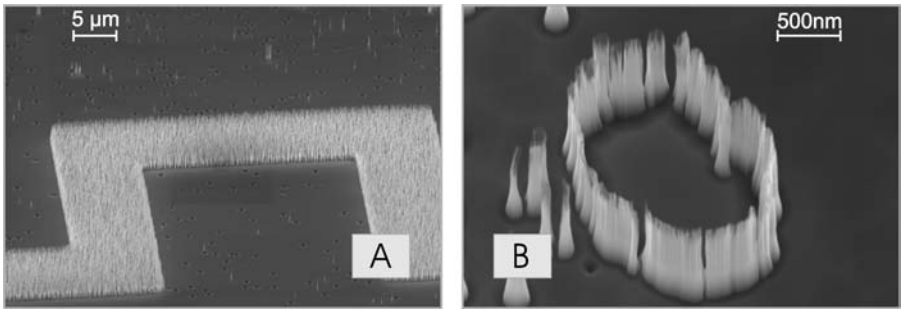

Figure 5.3: Lithographical control of the nanocolumns location (with topdown approach). The nanocolumns pattern are defined by optical and E-Beam lithography (A and B respectively).

Figure 5.2C and D illustrate GaN nanocolumns fabricated by ECR-RIE etching. The nanocolumns have diameters from 30 to 80 nm and heights from 1.4 to 2 μm. The etching is clearly anisotropic and the sidewalls are notably smooth. The nanocolumns are homogenously distributed on the sample with a density of $2-3\times10^9$ cm^{-2} and reproduce the Ti patterns deposited before etching. If we compare the column density with the estimated dislocation density of the original GaN wafer ($< 10^8$ cm^{-2}), no correlation can be found. In addition, we have observed a decreasing density of nanocolumns in the areas without Ti micro-masking of the same etched samples (Figure 5.3A). In those areas, the nanocolumns density decreases dramatically, which indicates a masking effect of different origin, probably due to Ga droplets not removed before the processing. We can therefore suggest that, unlike photoelectro-chemical (PEC) nanocolumn etching [VRJ$^+$01], the Ti ECR-RIE nanocolumns process is not dominated by the influence of dislocations. Even if we cannot explain completely the influence of the process parameters on the nanocolumn formation, we have observed a good reproducibility of the columns. Concerning the stability of the etching in relation to the process parameters, further detailed structural investigations are planned.

In connection to the spatial control of the nanocolumns, some attempts have been performed using thin patterns realized by means of electron beam lithography. Despite the successful result shown in Fig. 5.3B, two problems need to be solved in this approach.

- The available electron beam lift-off technique does not allow a thick Ti deposition. The thin Ti layer limits the etching time and the related nanocolumns width and height.
- Nanocolumns appear also without Ti micro-masking. The unwanted nanocolumns are randomly distributed on the samples, are thicker and cone-shaped.

5.2 Ohmic contacts

After the mesa etching, emitter (top) and collector (bottom) contacts are deposited. The electrical quality and the mechanical stability of the metal-semiconductor contacts play a determinant role concerning the efficiency and the lifetime of the Gunn diode. The special geometry and the vertical walls of the etched mesas allow a self-aligned approach, which means that both contacts are deposited at the same time and the division between emitter and collector is defined by the diode sidewall and not by a resist pattern. The self-aligned approach reduces the collector series resistance, minimizing the distance, which electrons have to drift in the bottom contact layer before entering in the metal conductor. Moreover, the process is simple and reliable, because it provides a high tolerance to lithography misalignment.

The considered contact technology produces an annealed ohmic contact (see also chapter 2.2.1). Thanks to the high doping at the interface metal-semiconductor, after the thermal treatment, the typical interface Schottky barrier becomes extremely thin. The barrier height is determined in both GaAs and GaN by the Fermi level pinning at the metal-semiconductor interface [Lüt95, IL03]. The thinner the barrier, the higher is the tunneling probability of the electrons crossing it.

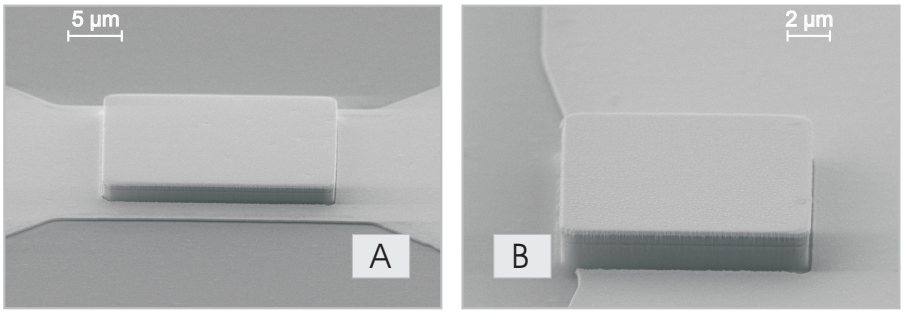

Figure 5.4: SEM pictures of the GaAs Gunn diode ohmic top and bottom contact. After the annealing process, the contacts present a relative flat surface and well defined edges.

The contact process flow is divided in three steps. At the beginning, the semiconductor surface has to be cleaned: the native oxide (about 1 nm) is removed from the surface by wet-chemical etching. Immediately after the cleaning, before the semiconductor oxidizes again, the metal is evaporated[2]. Then, the liftoff process is followed by the thermal annealing.

The chosen metal layer sequence for GaAs ohmic contacts is Ge/Ni/Au. After the deposition, the sample is alloyed at 400 °C for 75 s. For GaN Ti/Al/Ni/Au ohmic contacts have been deposited and annealed at 900 °C for 30 s. More details on the parameters of the two processes can be found in appendix C.5 and in [Lep97, Jav03].

Figures 5.4A and B illustrate two ohmic contacts layouts, which are realized on GaAs, for the planar oscillator integration (two port configuration) and for the S-parameters measurements (one port configuration). The surface after the annealing is relatively flat and the contact edges are well-defined. It can be noticed that there is practically no separation between the mesa wall and the edge of the bottom metal contact (self-aligned lithography).

5.3 Electrical isolation of the single Gunn diodes

The insulation of the Gunn diodes consists in a single etch process, removing the remaining electrical path between the diodes: the bottom contact semiconductor layer. In this way, the coplanar bond-pads and the oscillator components lay on the insulating material.

The GaAs diodes are covered with a positive thick resist pattern. After the optical lithography, the sample is baked for about 20 minutes, in order to harden the resist and improve the adhesion. Then, the open semiconductor material is removed down to the semi-insulating substrate. About 600 nm of GaAs is etched with a sulfuric acid and oxygen peroxide solution. After the wet-chemical etching, the hard resist mask can not

[2]It has been noticed that 10 seconds in situ sputtering before the metal evaporation improves further the contact quality.

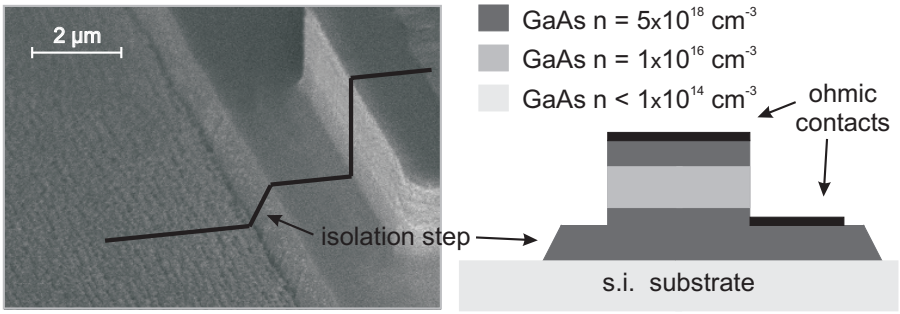

Figure 5.5: SEM picture of the GaAs Gunn diode after the wet-chemical etching for the device electrical isolation. On the left, a schematic view of the isolation step is shown.

be removed simply with acetone and propanol, but it requires 30 minutes of O_2 plasma oven process. In Fig. 5.5, a GaAs Gunn diode after the isolation treatment is presented. It is interesting to notice the oblique slope provided by this etching; the soft angle, in fact, acts as a ramp and it will be perfectly covered by the metal pads, avoiding the connection breaks.

Unfortunately, the GaAs process can not be directly transferred to the GaN one. Due to the strong bond energies, which distinguishing group III-nitrides from other compound semiconductors, it is difficult to find suitable etching techniques. Wet chemical etching is not applicable to GaN because of the low etch rates and the problem to find an appropriate mask. The solution is coming from argon ion sputtering. After protecting the GaN diodes with thick resist, as described for GaAs, the sample is bombarded by argon ions. The incident angle determines different etching profiles. Too small incident angle leads to very steep sidewalls and too high angle causes redeposition of etched material on sidewalls. An angle of 30 °C represents a good compromise [Jav03].

5.4 Polyimide planarization / passivation

In this process step, the Gunn diode mesa is covered with Duramide, a photoimageable polyimide precursor. The aim of this process step is to protect/passivate the Gunn diode mesa and to provide a basis for the electrical connection of the top contact, to the bond-pads. The sample is coated with a thick Duramide layer. A negative lithographic process defines rectangular patterns around the mesas (Fig. 5.6A). The lithographic process parameters (described in detail in appendix C.2) provide oblique walls of the patterns. These walls will support the connections to the bond-pads and for this reason, they should have an angle with the substrate as low as possible.

After the Duramide developing, the sample is baked in vacuum at 350 °C for one hour. During the hardening, Duramide undergo a final polymerization and should not come in contact with oxygen. The Duramide thickness is now measured with a profilometer: typical values are between 5.6 and 5.9 μm. Then, the cured Duramide film is etched

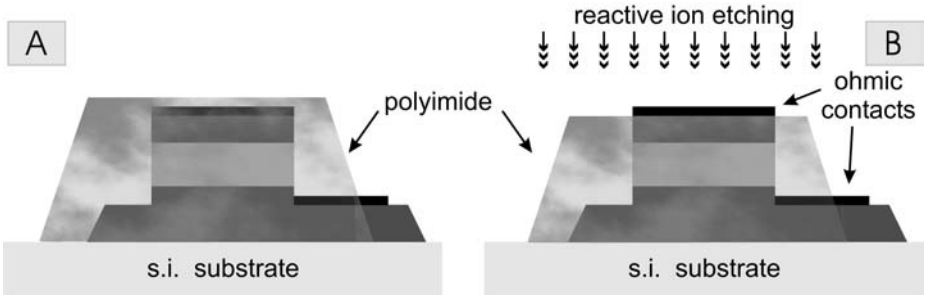

Figure 5.6: Schematic view of the planarization with polyimide: (a) the diode mesa is covered with polyimide, (b) the polyimide is etched up to the top contact level.

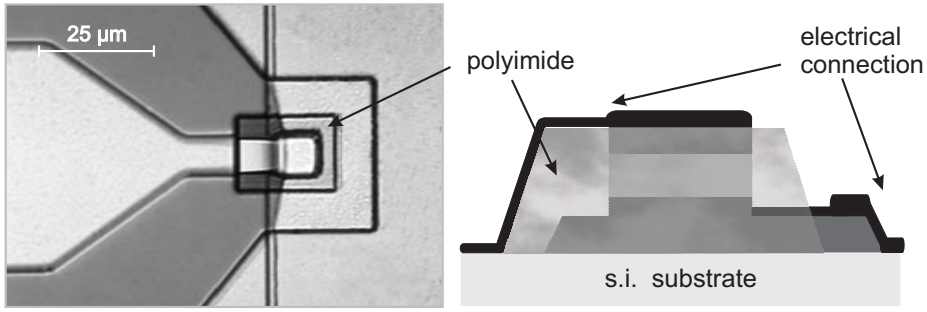

Figure 5.7: Optical microscope picture and schematic view of the bond-pads deposition after the polyimide planarization.

using a RIE process based on a gas mixture of O_2 and CF_4 [Sto99]. Figure 5.6B, shows schematically the principle behind the etching: the RIE process is stopped just after the opening of the top contacts. Taking into account, that the Duramide is not perfectly uniform on the sample (it is thicker at the borders), an over-etch of 200 nm is necessary.

5.5 Deposition of the bond-pads and of the oscillator passive elements

In this section, the processing of the coplanar-waveguide (CPW) pads is considered. At the same time, the passive components of the planar oscillators (low-pass filters, HF coupler and resonators) are deposited, as well. As explained before, two techniques have been developed for the top contact connection. Depending on the case, the bond-pads are combined with a polyimide planarization or with air-bridges.

Figure 5.7, illustrates how the polyimide acts as a fundament for the connections.

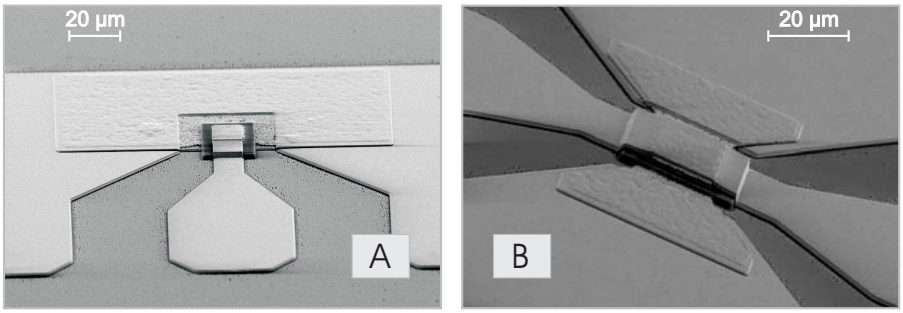

Figure 5.8: SEM pictures of the finished GaAs Gunn diode with coplanar pads: (a) the diode is designed in a one port configuration (S-parameter measurements), (b) the diode is designed in a two port configuration (integrated planar oscillator).

Unluckily, the polyimide is not a perfect ramp: some discontinuities could appear at the interface between the top contacts and the polyimide. For this reason, a special attention has been payed to the metal layers to be deposited. Also, the use of the rotating evaporation allows different incident angles for the incoming metal and a better coating of steep walls.

A special sequence of titan and gold (Ti/Au/Ti/Au, 50nm/50nm/50nm/650nm) has demonstrated excellent mechanical properties regarding the discontinuity between the polyimide layer and diode top contact. In Fig. 5.8, two SEM pictures of the finished GaAs Gunn diodes are presented. In one case, the diode is used for the S-parameters measurements (one port configuration) and in the other one, it is part of the integrated planar oscillator (two port configuration). The dimensions of the CPW layouts are matched to 50 Ω lines.

In Fig. 5.9, pictures of the GaAs MMIC Gunn diode oscillators are shown. The oscillators are composed of three parts: the periodic slow-wave low-pass filter (Fig. 5.9A), the interdigitated capacitor HF coupler (next to the Gunn diode Fig. 5.9B) and the different planar resonators (Fig. 5.9C).

For the air-bridge solution, the geometries and layout remain the same, except for the top contact connection, which is missing. Concerning the metal deposition, a simpler sequence (Ti/Au, 30nm/650nm) has been chosen. An alternative to the titanium layer could be chromium. Both metals exhibit a good adhesion to the substrate and once they are covered by gold, they do not oxidize. Ti/Au is a better option from the point of view of the lift-off process.

5.6 Air-bridge interconnection (optional step).

After CPW pads deposition, the top contact (emitter) is connected via air-bridges to the middle pads. This final process step represents a better alternative to the planarization with polyimide; in fact, air-bridges have several advantages over dielectric crossovers. In

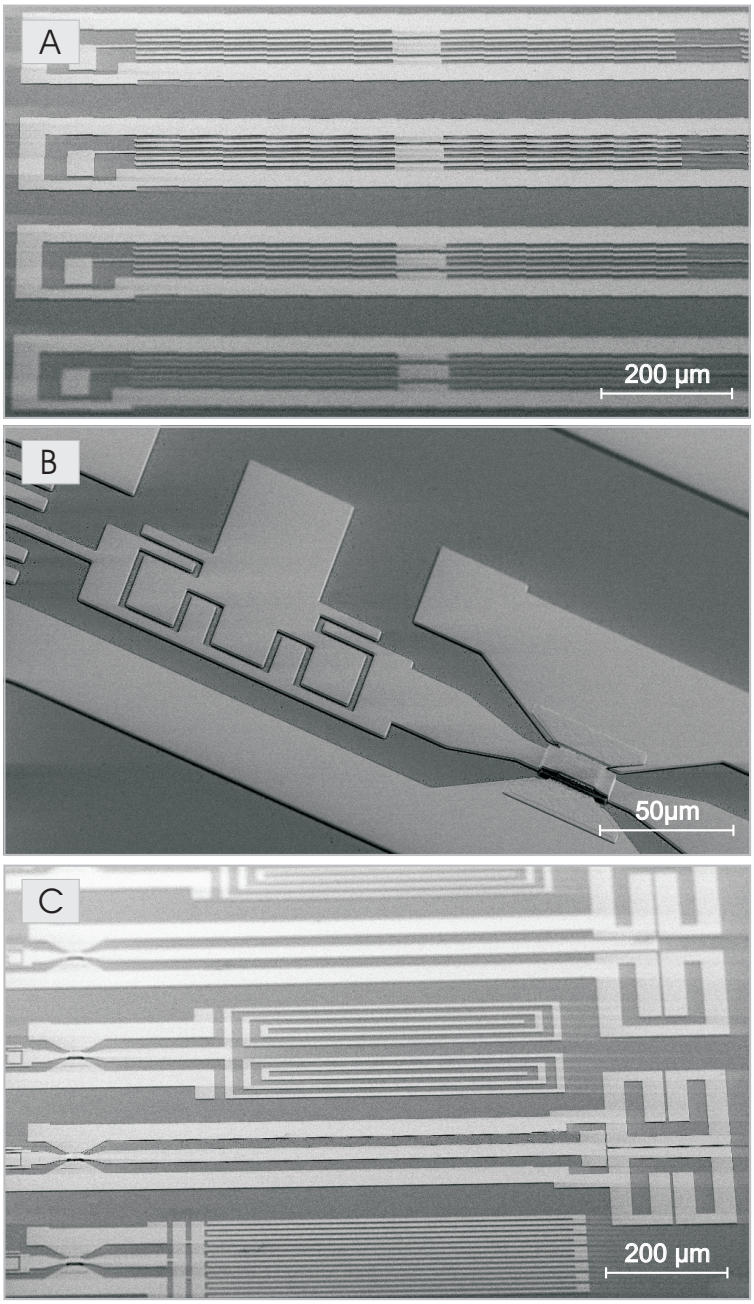

Figure 5.9: SEM pictures of the monolithic planar Gunn oscillator: (a) low-pass filters (DC input), (b) HF coupler (microwave output), (c) different resonators.

chapter 2.4, it has been suggested to exploit the good heat conductivity of gold in combination with thick air-bridges for cooling the Gunn diodes. Moreover, the bridge thickness permits device operations at high current densities and reduces the series inductances. Last but not least, the parasitic capacitance between the bridge and any metallization layer beneath is very low because of the height of the bridges and the low dielectric constant of the air.

The fabrication of airbridges involves many steps (see Fig. 5.10). Two resist patterns are required to define the plated gold layer; the *preplate* and *plate* patterns work together to define the electroplated gold-metal level. Openings in the preplate resist are defined in the places that necessitate interconection (Fig. 5.10A). After the resist development, a prolonged bake has been performed (see appendix C.2). This postbake ensures a perfect dryness of the resist layer and prevents the process compromise during the next softbake step.

After the *preplate* pattern is processed, the sample is covered with a thin intermediate Cr/Au/Cr seed layer, which serves to carry the electroplating current (Fig. 5.10B). Alternatives are Au/Ti[3] or only Au. Au/Ti prevents under-plating and Cr/Au/Cr provides a very good adhesion between the seed layer and the resist patterns. On the other hand, using only gold simplifies its removal later on. On top of the intermediate metal layer, a second resist is patterned to define the horizontal extent of any plated geometry, whether it is part of an air bridge or in contact with underlying metal (Fig. 5.10C).

For plating, a gold-bath from Enthone-Omi has been used. The bath, which is based on a gold cyanide complex, is kept at a temperature of 60 °C during plating. For more details on the plating step, see appendix C.5.

After plating the intermediate metal, the two resist layers have to be removed (Fig. 5.10E). The second resist layer receives a long flood exposure and then is developed away. 30 minutes of O_2 plasma etching cleans eventual remaining traces. The intermediate seed metal from not plated areas is etched with $(KI + I_2) : H_2O$ solution or sputtered with argon ions. Finally, the *preplate* resist is removed through boiling acetone and 30min of O_2 plasma etching.

The fabricated gold airbridges, realized during the processing of the graded gap injector GaAs Gunn diodes, are shown in Fig. 5.11. Two typical layouts are presented: two port configuration for integrated planar oscillator (A and B) and one port configuration for S-parameter measurements (C and D).

[3]Before plating the Ti layer is removed with HF.

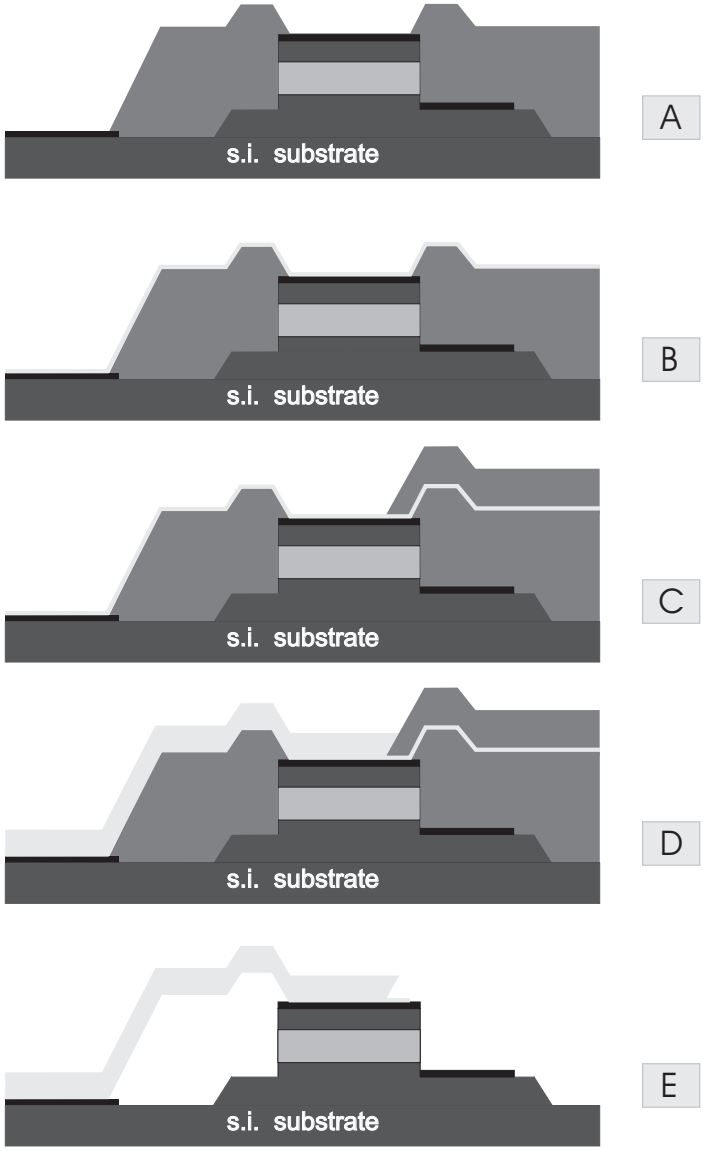

Figure 5.10: Air-bridge fabrication using gold plating process: (a) first lithographic process to open windows on interconnecting metal areas, (b) thin seed gold layer deposition for the plating current conduction, (c) second lithographic process to delimitate the plating areas, (d) plating of the gold bridges, (e) removing of the resist and of the seed gold layer [Lep97].

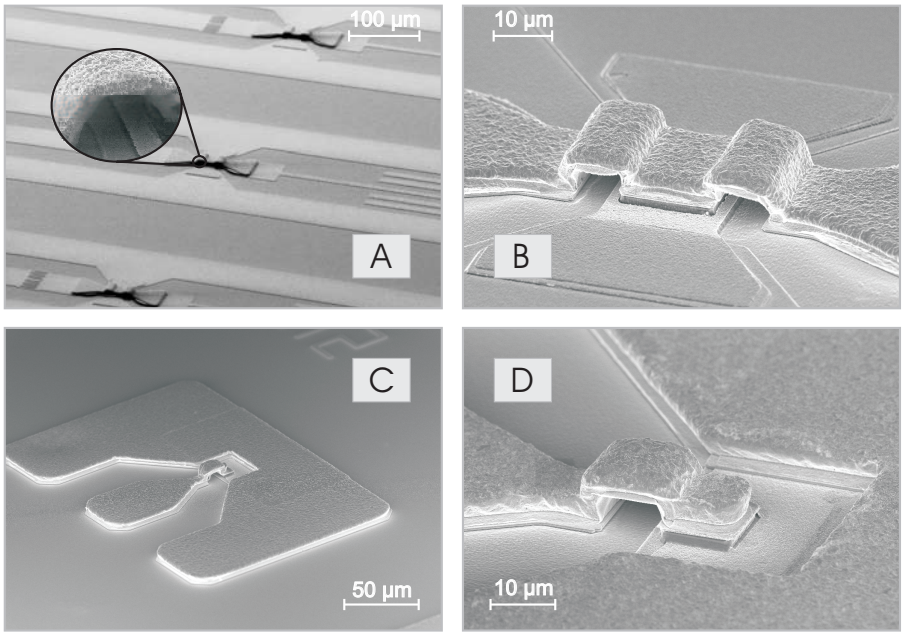

Figure 5.11: SEM pictures of the gold airbridges on GaAs Gunn diodes: in (a) and (b) the diodes are designed in a two port configuration (integrated planar oscillator), in (c) and (d) the diodes are designed in a one port configuration (S-parameter measurements)

Chapter 6

Experimental results and discussion

The electrical properties of the fabricated Gunn diodes and their temperature dependence are analyzed in this chapter from several points of view. Considering the numerous aspects to be treated, in order to avoid confusion, the discussion has been divided into three main topics.
The first two deal with the behaviour of the Gunn diodes, as single active devices, at low and high frequency, pointing out the electrical influence of each layer of the device structure. Special attention is given to the role of the two hot electron injectors: the graded gap barrier and the resonant tunneling double barrier.
The third part presents two different Gunn oscillator approaches: a conventional one based on a cavity resonator is compared with a novel quasi-planar monolithic integrated circuit (MMIC).

6.1 Gunn diode direct current behavior

6.1.1 Contacts

The parasitic connection resistances have a negative effect on the DC, high frequency and noise performance of an electronic device. Those resistances are basically the result of two components: the connection lines and the contact resistances. Because of the particular geometry of the Gunn diodes, the connection lines can be neglected, and the crucial parameter becomes the ohmic contact.

The available ohmic contact technology (section 5.2 [Lep97, Jav03]) did not require any improvement or optimization. However, TLM and CLM measurements (see section 4.5) have been systematically performed as quality verification to detect the process reproducibility or irregularity. The contact pads of the TLM structures are $150 \times 50\ \mu m^2$ squares and are separated by increasing distances of 5, 10, 15, 20, 40, 80 and 120 μm. The six circular shaped CLM structures consist of outer circles with constant diameter of 100 μm^2 and concentric inner circles with a decreasing diameters of 96, 92, 88, 84, 80 and 68 μm.

A measurement example for a TLM structure is shown in figure 6.1. The different linear I-V characteristics (Fig. 6.1 left side) are depending on the distance between pads.

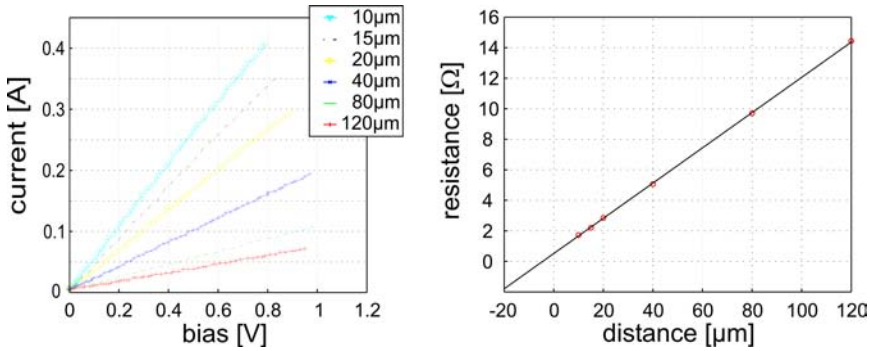

Figure 6.1: Graphic analysis of the transmission line measurement. On the left, I-V characteristics for the different distances between contacts. On the right, resistance versus pad distance.

The interpolation of the resistance dependance on the contact distance (Fig. 6.1 right side) provides the contact resistance $R_C\,[\Omega\,mm]$, the effective contact length $L_T\,[\mu m]$, the specific contact resistance $\rho_c\,[\Omega\,cm^2]$ and the sheet resistance $R_S\,[\Omega/\square]$.
All these parameters are summarized in table 6.1 for different wafers.

Table 6.1: Ohmic contacts for different processed wafers

W-number		R_C $[\Omega\,mm]$	L_T $[\mu m]$	ρ_c $[\Omega\,cm^2]$	R_S $[\Omega/\square]$
17008	GaAs	0.047	2.7	$1.2 \cdot 10^{-6}$	17.6
18006	GaAs	0.040	2.3	$9.2 \cdot 10^{-7}$	17.4
18038	GaAs	0.038	2.2	$8.2 \cdot 10^{-7}$	17.5
19032	GaAs	0.038	2.1	$8.0 \cdot 10^{-7}$	17.9
G695E2t	GaN	0.165	0.7	$1.1 \cdot 10^{-6}$	238
G695E2b	GaN	0.097	2.0	$1.9 \cdot 10^{-6}$	48

Concerning GaAs, the specific contact resistance ρ_C remains under $\sim 1 \cdot 10^{-6}$, which defines the upper limit for good ohmic contacts. The differences between the GaAs results are due to the process reproducibility and on the slightly different doping concentration of the considered wafers.
The values for GaN, instead, refer to the same wafer G695 and to the same sample E2. They have been prepared and annealed in the same time. The only difference is that G695E2t was processed on the top GaN contact layer and that G695E2b was processed on the bottom contact layer. Even if the doping nominal level is the same for the two layers, the top one is thinner than the bottom one (200 nm vs. 800 nm); this could explain the lower values of G695E2b sheet resistance. Another aspect that should be taken into account, is the influence of the dry etching and the related crystal deterioration: the bottom ohmic contact G695E2b lays on a surface which was subjected to an aggressive chlorine based plasma process. An improved plasma etching process could reduce the

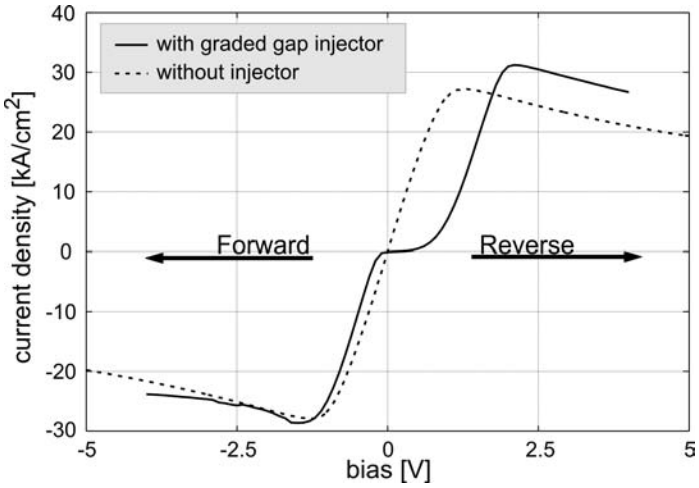

Figure 6.2: I-V characteristics for two Gunn diodes: one with the graded gap injector (solid curve), the other one without (broken curve). Negative voltages correspond to forward currents, positive voltages to reverse currents.

reported inconsistency between top and bottom contacts.

6.1.2 I-V characteristics of graded gap injector GaAs Gunn diodes

Figure 6.2 shows the DC characteristics of two GaAs Gunn diodes: one with the graded gap injector (GGI) and the other one without. In our case, the current flows in the forward direction when a negative voltage is applied on top of the device. As expected, the I-V characteristics of the diode without injector is symmetric. The diode with the graded gap injector presents an asymmetric I-V curve with a well pronounced Schottky-like behavior. In addition, the maximum current in the reverse direction (positive voltages) is about 10% higher than in the forward one. This is an indication for different electron occupations of the L-valley, causing different drift velocities for the two current directions.

In order to find the most effective injector, devices with different maximum aluminium concentrations have been compared (28%Al up to 34%Al). The DC characteristics of the diodes for low voltages are shown in Fig. 6.3: especially in the reverse direction, the Schottky-like behavior becomes more pronounced with increasing Al concentration, i.e. higher barriers.

In the steep increasing part of the I-V curves, the slopes in the two directions are nearly identical. These slopes reflect the quality of the ohmic contacts and no relevant change has been observed for different Al concentrations in the barriers.

After the linear region, the current peak and the DC negative differential resistance should be interpreted as a pure self heating effect. Considering the poor heat properties

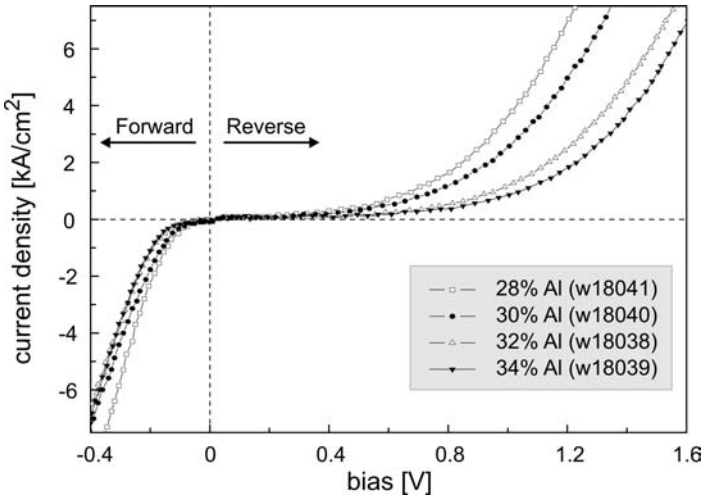

Figure 6.3: Low voltage I-V characteristics of diodes with different Al maximum concentration in the graded barrier.

Table 6.2: Peak current densities in the forward and reverse direction for different Al concentrations in the injector.

		28% Al	30% Al	32% Al	34% Al
J_p^{fw}	$[\frac{kA}{cm^2}]$	30.40	29.60	28.80	28.40
J_p^{re}		31.05	31.20	30.60	30.96
J_p^{fw}/J_p^{re}		**0.98**	**0.95**	**0.94**	**0.92**

of GaAs, self heating is playing an important role (see section 6.1.6 and section 6.2.1).

In the reverse current direction, electrons enter the active-region directly without passing any hot electron injector. In this case, no enhanced L-valley occupation can be expected. This results in a current peak nearly independent of the Al-concentration.

In the forward direction, different injectors lead to different occupations of the L-valley and therefore to different peak drift velocities and peak currents. The forward current decreases with increasing Al concentration. The ratios between the peak current densities J_p in both directions are presented in Table 6.2.

The current maxima in the forward and in the reverse direction can be used as a measure of the injector effectiveness. The lower the ratio J_p^{fw}/J_p^{re}, the more efficient is the electron injection in the L-valley (Table 6.2). Nevertheless, only a high frequency investigation allows an analysis of the Gunn diode injector in the whole operating bias range ($3\,V - 6\,V$), obtaining a quantitative estimation of the related L-valley occupations (see section 6.2.4).

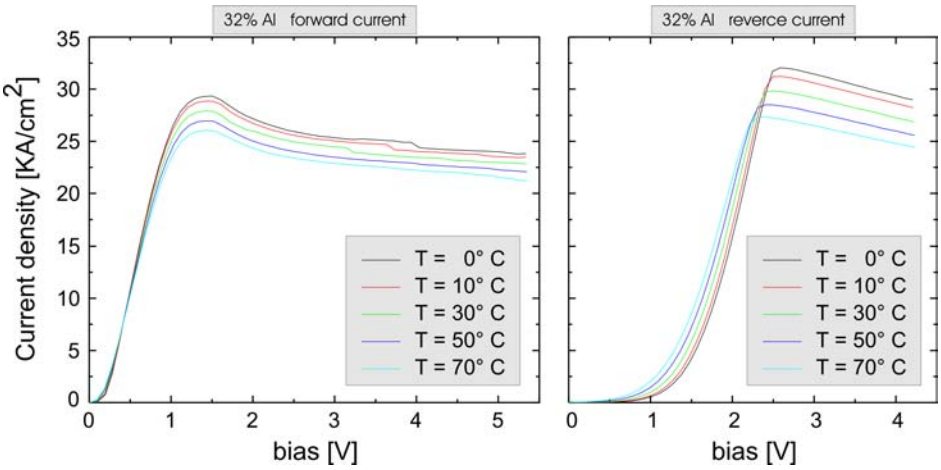

Figure 6.4: Forward (left diagram) and reverse (right diagram) I-V characteristics of a graded gap injector Gunn diode (32% Al) for different temperatures.

6.1.3 Temperature dependant DC modelling of graded gap injector GaAs Gunn diodes

The graded gap injector of the Gunn diodes can be analyzed using temperature dependent DC measurements. An example of the DC temperature behavior of a GaAs Gunn diode is shown in Fig. 6.4 for an injector with 32% maximum Al concentration. As expected, the peak current is strongly temperature dependent. This effect is directly connected with an increase of the active region resistance with temperature.
The primary explanation comes from the relative occupations of the Γ and L-valley: higher the temperature, higher the L-valley occupation and lower the average drift velocity and current. The effect is stronger in the reverse direction, because of the higher number of electrons remaining in the Γ valley.
In the I-V characteristics region where the slope is positive, an important factor contributing to the change of the diode resistance is the increase of scattering processes with temperatures. Scattering is not connected with the injector properties nor with the current direction.

For low voltages, we assist to the opposite phenomena: the current increases rising the temperature. The low voltage behavior is extremely influenced by the injector: the thermionic emission of the electrons over the barrier increases dramatically with increasing temperatures.

Temperature dependent simulations of graded gap injector Gunn diodes

In chapter 2.2.2, the equivalent circuit for a graded gap injector Gunn diode has been described and Eq. (2.60) has been proposed for analytical modelling. A simulation package

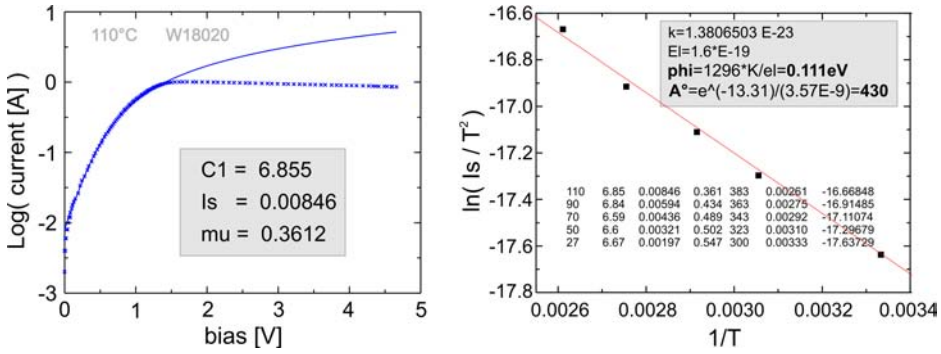

Figure 6.5: Graphical procedure to obtain the barrier height ϕ, the effective Richardson constant A^* and the saturation current Is.

for an automatic evaluation of temperature dependent I-V characteristics in connection with Eq. (2.60) has been written. A complete description of the methods and the software code can be found in [FML03].

Using Eq. (2.60) and taking as fitting parameters c_1, μ and I_s, the measured I-V curves have been fitted at different temperatures (left diagram of Fig. 6.5). For each temperature, a set of c_1, μ and I_s has been obtained. Assuming that the temperature dependance of the injector is described by a Richardson law (see section 2.2.1 and Eq. (2.53)) , I_s is given by:

$$I_s = AJ_s = AA^*T^2e^{-\frac{q\phi}{kT}} \tag{6.1}$$

where ϕ is the barrier height of the graded gap emitter and A the diode cross-section area. As seen from Eq. (6.1), the representation of $ln(I_s/T^2)$ versus 1/T is a straight line (right diagram of Fig. 6.5). The slope of the fitted line gives the barrier height ϕ and the intersection with the axis $1/T = 0$ gives $A \cdot A^*$.

The described procedure has been applied to several diodes with different injectors. For a better visualization of the results, only four cases are considered, focusing on the influence of the maximum Al concentration in the graded barrier. The diode layer structures have been grown in a sequence and processed simultaneously to minimize inaccuracy or inhomogeneity. In Fig. 6.6, the barrier height ϕ is represented as a function of the saturation current I_s at 50°C.

The general tendency in Fig. 6.6 follows the expectations. Increasing the maximum Al concentration in the graded barrier, the saturation current decreases and the barrier height increases.

Once the layer-structure is decided and the parameters c_1, μ and I_s are determined, the described procedure is suggested as a production benchmark. In a global environment, where costs and quality issues are strongly connected, minimum reliability targets lower then 2ppm[1] are standard requirements. Each production step is a potential thread for the

[1]Maximum failure rate per year in part per million.

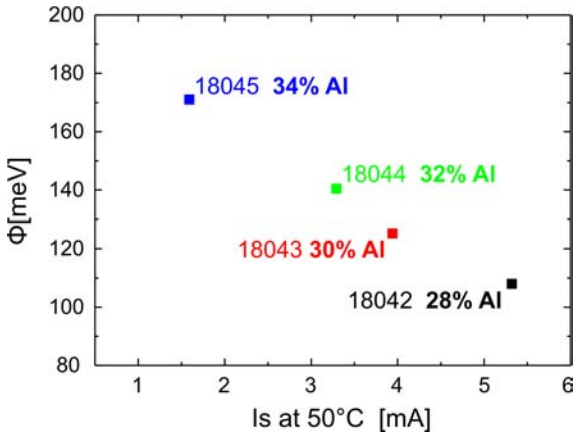

Figure 6.6: The graded gap barrier height as function of the saturation current Is at 50°C for different maximum Al concentration (28%, 30%, 32% and 34%) in the graded gap injector. The processing and the measurements of the diodes considered in this diagram belongs to the cooperation project [Pro04].

fulfillment of these severe targets and needs a constant control. The proposed benchmark gives a full overview on the layer structure and processing quality with a small effort (DC measurements).

6.1.4 I-V characteristics of resonant tunnelling injector GaAs Gunn diodes

The typical I-V characteristics of a Gunn diode with resonant tunneling injector (RTI) is illustrated in Fig. 6.7. For low voltages, the I-V curve of the RTI Gunn diode in the forward and in the reverse direction is symmetric. This symmetry confirms the good quality of the double barrier structure and of the ohmic contacts. The low voltage asymmetry observed in the case of GGI Gunn diode (Fig. 6.3) was due to the Schottky-like behavior of the graded barrier. The Schottky-like characteristic is a distinctive feature of the graded gap injector and causes unwanted voltage drop.

Applying higher voltages, the current shows a peak and a negative slope witnesses the self heating of the device. As for the GGI Gunn diode, the forward current peak is much lower than the reverse one. This is a first hint of the resonant tunneling injector effectiveness. The already defined ratio between the peak current density in the forward (24.5 kA/cm^2) and in the reverse direction(35 kA/cm^2), J_p^{fw}/J_p^{re} is equal to 0.7. In comparison with the graded gap injector (0.9), this is a much better result. Moreover, the negative slope of the RTI diode in the forward direction is flatter than the one in the reverse: this gives the impression of a less influence of the forward current by self-heating effects.

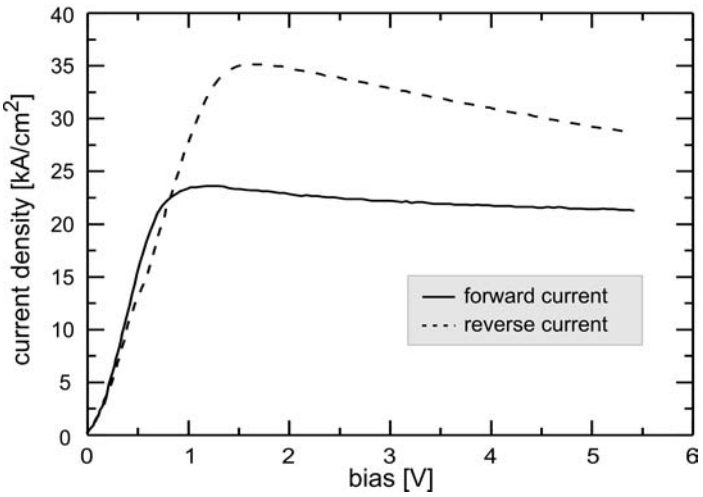

Figure 6.7: I-V characteristics of a typical resonant tunneling injector Gunn diode.

One final remark for the RTD specialists concerns the resonance of the double barrier and the peak to valley ratio. Figure 6.7 does not show any steep negative differential resistance (typical in RTD structures) because of the particular design of the device. The peak current of the isolated double barrier structure has been estimated at current densities higher than $60kA/cm^2$. The Gunn diode active region prevents the flowing of such a high current and avoids the undesirable bistability. For thick AlAs double barriers ($\geq$6 monolayers), such a phenomenon is expected in the following conditions: the measurement has to be carried out at lower temperatures, with very short pulses, and in the reverse direction, where the Gunn diode current densities are higher.

6.1.5 I-V characteristics of GaN Gunn diodes

Figure 6.8 shows representative I-V characteristics of GaN Gunn diodes. The considered structure does not present an injector and no distinction between forward and reverse polarity is made because of the nearly symmetrical results. The measurements have been carried out in three different conditions: 80 μs, 300 μs and no pulses. There is practically no difference between the three situations up to 7 V. In all three cases, the curves are linear, confirming the good quality of the ohmic contacts. After 7 V, the slope of the solid curve (no pulses) starts to decrease. The current saturates and does not show any maximum like in GaAs Gunn diodes without injector. The current starts to saturate at higher biases, 8.5 and 10 V for 300 and 80 μs pulses, respectively. This effect is clearly connected with self-heating: even if GaN is a good thermal conductor, the Gunn diode active region is not in direct contact with an efficient heat-sink, but with a thick sapphire substrate. As reference, the thermal conductivity at room temperature of GaN

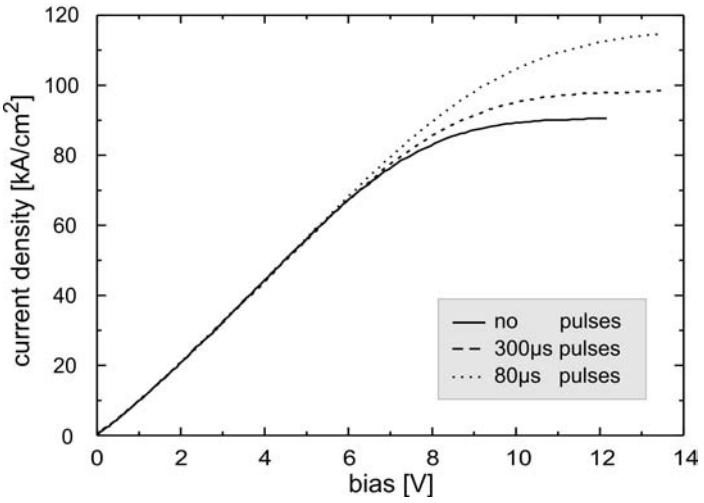

Figure 6.8: I-V characteristics of a typical GaN Gunn diode with $80\mu s$ and $300\mu s$ long pulses.

is 130 $Wm^{-1}K^{-1}$ but the one of sapphire is only 30 $Wm^{-1}K^{-1}$. Moreover, the power density, to be dissipated, reaches 1 MW/cm^2.

Which is the real origin of the current saturation shown in Fig. 6.8? Is the intervalley transfer playing a role in this phenomenon? Concerning this aspect, it is difficult to make a real comparison of the DC properties of the presented GaN Gunn diode with data from the literature. Considering the threshold field E_T as the electric field at witch the slope of I-V is zero, values of about 87.5 kV/cm can be estimated (80 μs long pulses). This value is from 30% up to 40%, lower than the simulated values reported in the literature [KOB+95, AWR+98]. The discrepancy could be explained as misinterpretation of the device length (the active region has been considered $1.6\mu m$ long in the previous estimation).

The maximal current density levels are around 90 kA/cm^2. Taking as reference value typical GaAs Gunn diodes without injector, the maximal current densities range from 30 to 40 kA/cm^2. The current density differences are due to the different doping concentrations (10^{17} cm^{-3} for GaN and 10^{16} cm^{-3} for GaAs) and to the respective maximal drift velocities, which were already described in chapter 2.1.2 and in Fig. 2.4.

6.1.6 100 ns pulse measurements: heat effects evidences

In section 6.1.3, it has been shown how sensitive are Gunn diodes to the environment temperature shifts. In section 2.4, it has been demonstrated that the inside temperature of the Gunn diode is much higher than the environment one, because of the self-heating. If we want to measure I-V characteristics without self-heating effects, very short pulses

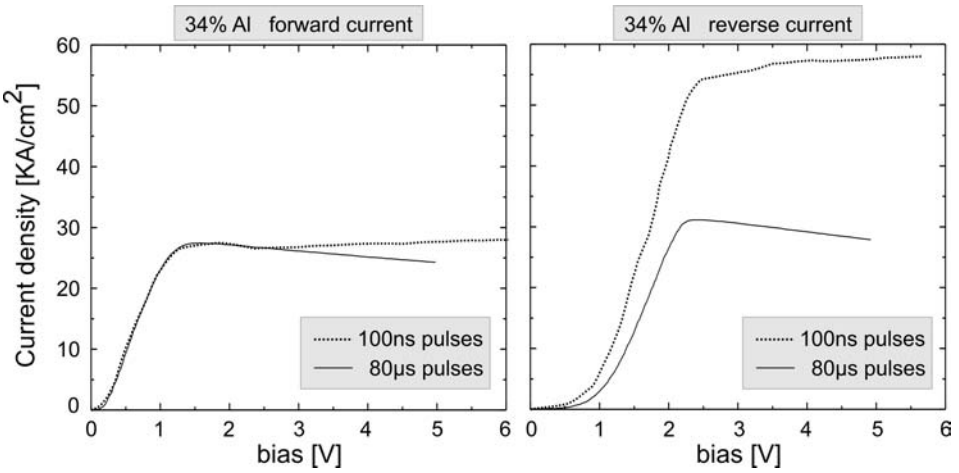

Figure 6.9: Forward (left diagram) and reverse (right diagram) I-V characteristics of a graded gap injector Gunn diode (34% Al) with 100ns and 300μs pulses.

with a low duty cycle have to be used. For this purpose, very short pulse measurements have been carried out. The description of the measurement setup can be found in chapter 4.6.

In Fig. 6.9, the I-V characteristics of a graded gap injector Gunn diode with very short pulses (100ns) are illustrated. For comparison, measurement carried out with longer pulses (80μs) are also presented. It can be noticed, that with short pulses, the I-V curves do not show a negative slope. 80μs pulses, instead, are enough long to heat up the diode. This confirms, beyond doubt, that self heating is the origin of the negative slope in the I-V characteristics of the Gunn diodes. A better estimation of the negative slope dependance on the heating time (pulse length) is given in section 6.2.1.
In the forward current direction, up to the current peak, there is practically no difference between long and short pulse I-V curves; after the current peak, the difference remains marginal. For the reverse bias, however, there is a large difference between the two cases. The current increase is dramatic when the short pulses are applied. The above evidences demonstrate the effectiveness of the injector. In the reverse direction, the electron occupation of the Γ valley is high. A long pulse length causes a stronger self-heating of the active region leading to a higher inter-valley transfer, a lower Γ valley occupation and a lower mean drift velocity. In the forward direction, the Γ valley occupation is low because of the injector; a further decrease due to the heating has only marginal effects on the current.
The ratio between the peak currents in the two directions is now free from self-heating effects and can give a clear estimation of the injector effectiveness.

The short pulse setup was also used to determine the breakthrough voltage for diodes with different injectors and with different passivation [Pro04]. The breakthrough voltage

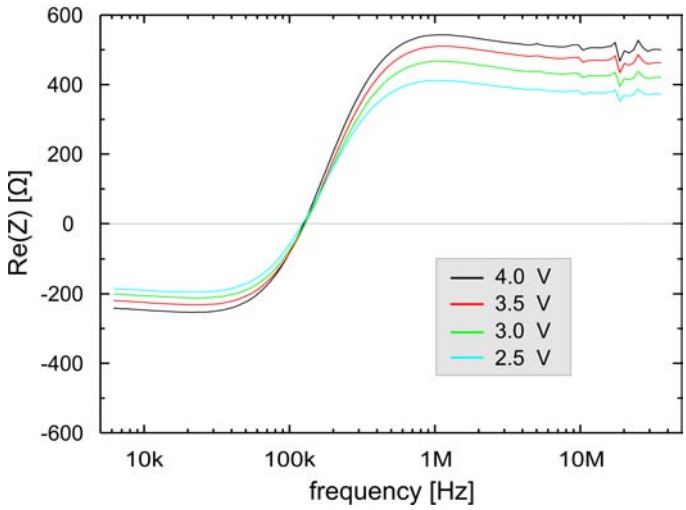

Figure 6.10: Differential resistance vs. frequency in the forward direction. Diode parameters: no injector, area=256 μm^2, active region length= 1.6 μm. [Sto03]

is indicated by a sudden increase in the current behavior for high biases. Measuring the breakthrough voltage with long pulses, it damages irreversibly the Gunn diodes, due to the current stress. With short pulses, the influence of a Si_3N_4 passivation has been examined. The average value of the measured breakthrough voltages is about 9V. Negligible differences have been found between passivated and unpassivated diodes. As expected, the breakthrough voltage is slightly higher in the forward direction because of the lower current density.

6.2 Gunn diode high frequency behaviour

6.2.1 Impedance measurements up to 50MHz

In section 6.1.6, it was demonstrated that the I-V characteristics of a GaAs Gunn diode, measured with very short pulses (100 ns), does not have a negative slope after the threshold voltage. The negative differential resistance appearing for longer pulses (80μs) was explained as consequence of the heating of the diode. Due to restrictions of the pulse setup, it was not possible to determine the exact pulse length, which represents the transition from a negative slope behaviour to a positive one. An interesting method for this estimation is proposed in [Sto03]: the impedance-frequency characteristics of the Gunn diodes are measured, in order to study the transition frequency at which the resistance from negative becomes positive. The measurement is performed with an Agilent 4294 Precision Impedance Analyzer in a frequency range from 5 kHz up to 50 MHz.

In Fig. 6.10, the real part of the measured impedance is presented as function of the frequency for a GaAs Gunn diode without injector. The absolute value of the differential resistance increases for increasing bias voltages. For all the biases, the transition from negative to positive differential resistances appears at a frequency between 100 and 200 kHz. This transition can be better understood introducing an equivalent circuit for the temperature changes inside the diode. The thermal resistance and capacity of the Gunn diode mesa are defined as:

$$R_{TH} = \frac{h}{\lambda A} , \tag{6.2}$$

$$C_{TH} = c_v m , \tag{6.3}$$

where c_v is the specific heat capacity, m the mass, h the thickness, A the area, and λ the thermal conductivity. It is now possible to express a time constant τ_{TH} and the related frequency for the defined RC system:

$$\tau_{TH} = R_{TH}C_{TH} = \frac{c_v m h}{\lambda A} , \tag{6.4}$$

$$f_{TH} = \frac{1}{2\pi\tau_{TH}} = \frac{\lambda A}{2\pi c_v m h} . \tag{6.5}$$

Assuming an uniform material, the mass m can be expressed as

$$m = \rho V = \rho A h , \tag{6.6}$$

where ρ is the density and V the volume of the mesa. The time constant and the frequency can be written as:

$$\tau_{TH} = R_{TH}C_{TH} = \frac{c_v \rho h^2}{\lambda} , \tag{6.7}$$

$$f_{TH} = \frac{1}{2\pi R_{TH}C_{TH}} = \frac{\lambda}{2\pi c_v \rho h^2} . \tag{6.8}$$

Equation 6.7 and 6.8 are now independent on the mass and area of the mesa. This property has been confirmed experimentally in [Sto03], where the transition frequency from negative differential resistance to positive one was constant with different diode areas.

For our GaAs mesa c_v is 350 $J/(kgK)$, λ is 46 $W/(mK)$, ρ is 5500 kg/m^3 and h is 3 μm. f_{TH} can be estimated as:

$$f_{TH} \approx 422\ kHz . \tag{6.9}$$

The computed f_{TH} is two times higher than the transition frequency of the measured diodes in Fig. 6.10. The RC model, actually, is taking into account only the volume of the mesa. In reality, the effective volume should consider also a part of the semiconductor under the diode. Increasing the parameter h with 2 μm, f_{TH} results:

$$f_{TH} \approx 152\ kHz . \tag{6.10}$$

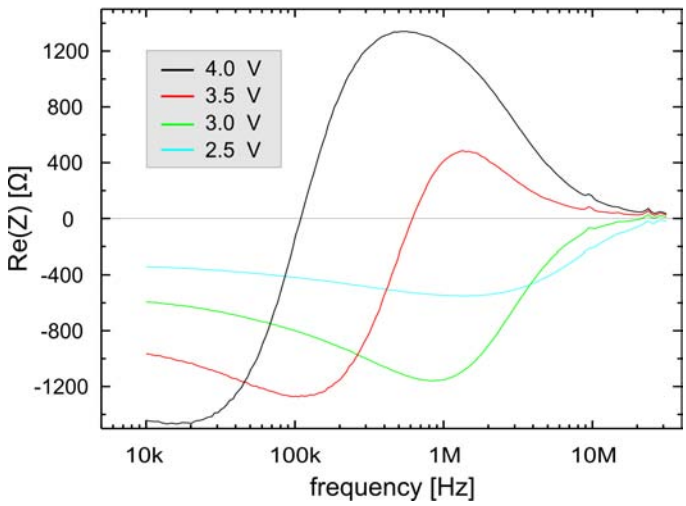

Figure 6.11: Differential resistance vs. frequency in the forward direction. Diode parameters: graded-gap-injector (32% Al), area=196 μm^2, active region length= 1.8 μm.

The corrected value of f_{TH} matches quite well the behaviour of the measured GaAs Gunn diodes without injector.

Impedance measurements have been also performed on graded gap injector GaAs Gunn diodes. A Gunn diode with a hot electron injector does not follow anymore the described model. The heating of the device is not uniform. Furthermore, the dissipated power density distribution is depending on the voltage. In Fig. 6.11, it can be noticed that the transition frequency changes with voltage. At 4 V the transition frequency is between 100 and 200 kHz, like for the diodes without injector. For lower voltages, the transition frequency shifts to much higher frequencies.

To understand Fig. 6.11 and the injector influence, let us consider a diode bias range from 2 up to 6 V. If we assume the current to be constant after the threshold voltage, the power dissipated in the injector is also constant. In the same bias range, the diode dissipated power increases linearly with the terminal voltage. From these considerations, at higher voltages, the influence of the injector can be almost neglected, explaining the similarity found at 4 V between diodes with and without injector.

6.2.2 High frequencies investigations of GaAs Gunn diodes

Gunn diodes are normally mounted in a cavity and the resulting oscillators are measured and used as microwave generators. The literature of the last 30 years deals extensively with such data. Despite the possibility to de-embed the package, the cavity and the outside circuit from the measured data, it is very hard to achieve a good characterization of the device. The resulting information does not help to explain completely the behavior

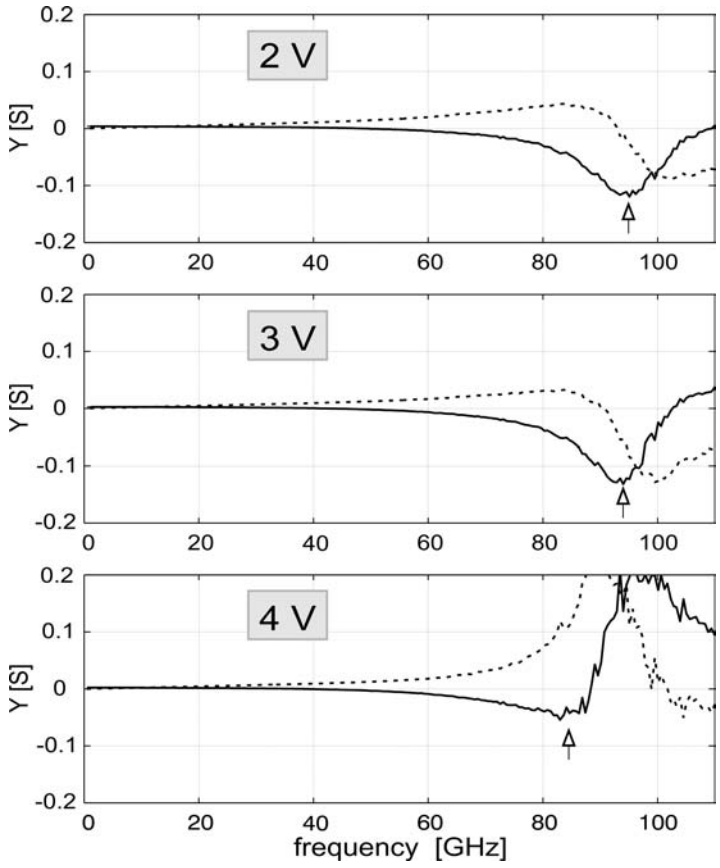

Figure 6.12: Conductance and susceptance, solid and broken curve, vs. frequency for different applied positive DC bias. Diode parameters: no injector, area=196 μm^2, active region length= 1.6 μm.

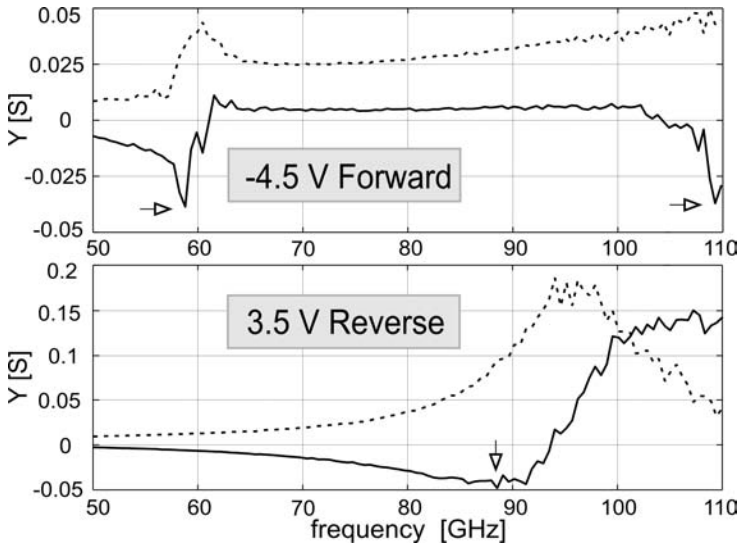

Figure 6.13: Conductance and susceptance, solid and broken curve, vs. frequency in the forward and the reverse direction. Diode parameters: graded-gap-injector (32% Al), area=196 μm^2, active region length= 1.8 μm.

of the diode itself. Therefore, S-parameter measurements up to 110 GHz have been performed, in order to evaluate the small signal behavior of Gunn diodes with and without hot electron injector, at very high frequencies.

A complete description of the S-parameters and of the network analyzer setup can be found respectively in chapter 2.3.1 and 4.7.1.

The conductance and the susceptance of a Gunn diode without injector for different positive bias voltages are shown in Fig. 6.12. The negative conductance presents a voltage dependent minimum. The corresponding frequencies are 96 GHz at 2 V, 92 GHz at 3 V and 87 GHz at 4 V. In all the measured samples, the negative conductance minima frequency decreases with increasing voltage.

Figure 6.14 shows the admittance of a Gunn diode with the graded gap injector for negative (forward direction) and positive (reverse direction) voltages. The reverse direction looks similar to the one of the diodes without injector. It is not surprising, considering that the injector is designed to work only in the forward direction. For negative voltage, in fact, the influence of the graded gap injector leads to a sharp peak-like appearance of the negative conductance minimum near 60 GHz. The sharp negative conductance minimum is a direct consequence of the dead zone reduction caused by the injector. Additionally, a shift to lower frequencies can be observed and the second harmonic minimum appears.

Figure 6.14 shows the admittance of a Gunn diode with the resonant tunneling injector for negative and positive voltages. Again, the reverse direction looks similar to

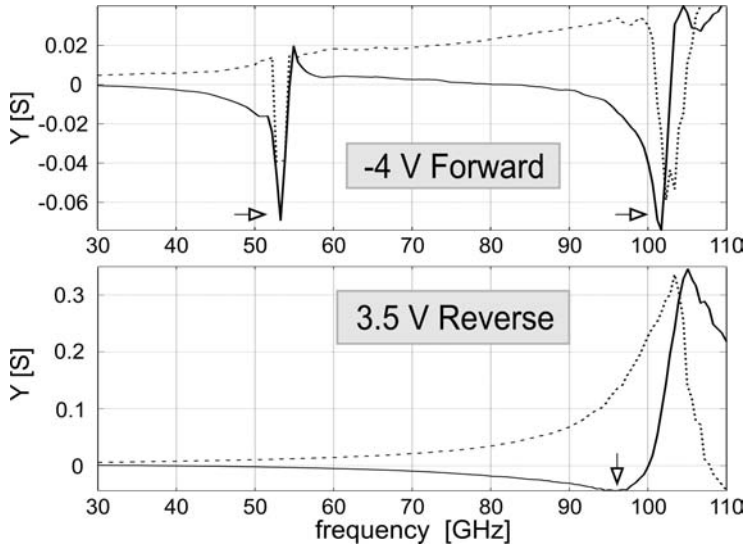

Figure 6.14: Conductance and susceptance, solid and broken curve, vs. frequency in the forward and the reverse direction. Diode parameters: resonant tunneling injector (6 AlAs monolayers per barrier), area=196 μm^2, active region length= 1.6 μm.

the one of the diodes with the graded gap injector and without injector. In the forward direction, also the resonant tunneling injector presents a peak-like resonance of the negative conductance minimum. The minimum is sharper than for the graded gap injector and the shift to lower frequency is larger. These results represent a further evidence of the significant potentials of the resonant tunneling injector.

6.2.3 Drift velocity computation and operation mode classification

On the basis of the Gunn diode small signal admittance (see section 2.1.4), after McCumber and Heime [MC66, Hei71]

$$Y(\omega, v_d, \mu_0) = A\epsilon\epsilon_0 v_d \frac{\gamma^2}{e^{-\gamma L} + \gamma L - 1}\,, \tag{6.11}$$

$$\gamma = \frac{en_0\mu_0}{\epsilon\epsilon_0 v_d} + i\frac{\omega}{v_d}\,, \tag{6.12}$$

the electron drift velocity can be derived. In Eq. (6.11) and 6.12 v_d is the drift velocity, μ_0 the mobility, ω the angular frequency, A the device area, ϵ the relative permittivity, ϵ_0 the vacuum permittivity, e the electron charge, L the device active region length and n_0 the total carrier concentration. It could be shown that at certain frequencies (f_{NCM}),

Table 6.3: Frequencies corresponding to the negative conductance minima (f_{NCM}) for diodes with different active region lengths (L) and areas at $4\,V$; as expected the product $f_{NCM} \cdot L$ remains constant.

	$L_1 = 1.8\mu m$		$L_2 = 1.5\mu m$	
Area	f_{NCM1}	$f_{NCM1} \cdot L_1$	f_{NCM2}	$f_{NCM2} \cdot L_2$
396 μm^2	59.4 GHz	1.06E5 m/s	69.8 GHz	1.05E5 m/s
196 μm^2	59.0 GHz	1.06E5 m/s	70.8 GHz	1.06E5 m/s
144 μm^2	62.0 GHz	1.11E5 m/s	70.4 GHz	1.06E5 m/s

minima in the negative conductance appear. These frequencies are directly correlated with the drift velocity v_d and the sample length L:

$$\frac{L\omega}{v_d} = 2\pi m \qquad (m = 1, 2, 3..), \tag{6.13}$$

$$f_{NCM} = \frac{v_d}{L} m, \tag{6.14}$$

where the number m accounts for higher harmonics, which can be observed also in Fig. 6.13 in the forward direction, near 110 GHz.

Equation 6.14 can be applied to the measured diodes, in order to estimate the drift velocity dependance on the electric field. In Table 6.3, samples with different active region lengths ($L_1 = 1.8\,\mu m$ and $L_2 = 1.5\,\mu m$) and different areas are compared at $4\,V$. The experimental values prove the predictions of Eq. (6.14): there is an inverse proportionality between the frequencies of the negative conductance minimum ($f_{NCM} \approx 1/\text{transit time}$) and the active region length. The value $f_{NCM} \cdot L$ can be interpreted as the average group velocity of the electrons in the active region ($\sim 1.06 \cdot 10^7\ cm/s$ for diodes with injector).

In Gunn diodes the drift velocity depends on three parameters: device temperature, electric field and injector barrier.

The shift with bias to lower frequencies of the negative conductance minima (Fig. 6.12) can be understood thinking on the electric field-drift velocity characteristic for GaAs: the increase of the applied voltage leads to a quasi-proportional change of the electric field, at the same time the drift velocity should decrease (we are considering electric fields higher than the critical electric field).

In Fig. 6.15 the measured drift velocity ($f_{NCM} \cdot L$) is shown as a function of the supplied voltage. The diode without injector behaves symmetrically applying positive and negative biases. For voltages lower than $1.5\,V$, there is no Gunn effect; from $1.5\,V$ up to $2\,V$, the drift velocity increases and reaches a maximum; for voltages higher than $2.2\,V$, the drift velocity decreases rapidly.

The drift velocity for diodes with injector is asymmetric (Fig. 6.16). In the reverse direction, it can be assumed that there is no injector, since in this configuration the graded gap barrier is situated at the end of the active region. Therefore, the voltage dependance of the drift velocity is very similar to the one without injector. In the forward direction, because of the injector barrier, the electrons are already hot when they enter the active region and the resulting drift velocity is smaller. A clear tendency can be observed as a

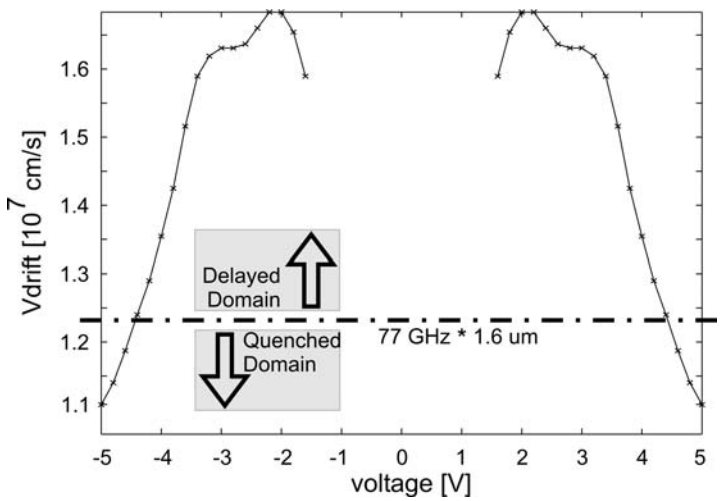

Figure 6.15: Drift velocity vs. voltage. Diode parameters: no injector, area=196 μm^2, active region length= 1.6 μm.

function of the Al-content in the injector layer: the higher the Al-content, the lower the drift velocity and the flatter the slope of the curve. This property is directly connected with the diode frequency stability. Diodes with flatter drift velocity-voltage dependance should be less affected by temperature or voltage changes, because the occupation of the L-valley is mainly dominated by the hot electron injection rather than the electrical field or temperature activated process.

A direct, voltage depending comparison between the negative conductance minima of the planar diodes and the oscillating frequencies of the packaged diodes cannot be made. When diodes are mounted inside a resonator, their behavior will be additionally affected by the resonator properties. However, with the help of the planar structures, some important trends in the high frequency behaviors have been identified, leading to a better layer structure and to an optimization of the packaged diodes.

By placing a transferred electron device in a cavity or resonant circuit, we can distinguish three main operational modes (see chapter 2.3.3):

The Transit Time mode. The oscillation frequency f_r is determined by the space charge or domain transit time τ_d:

$$f_r = \frac{1}{\tau_d} = \frac{v_{drift}}{L} \; . \tag{6.15}$$

The Delayed Domain mode. The resonant period of the circuit T_r is longer than τ_d:

$$\frac{1}{2 \cdot \tau_d} = \frac{v_{drift}}{2 \cdot L} < f_r < \frac{1}{\tau_d} = \frac{v_{drift}}{L} \; . \tag{6.16}$$

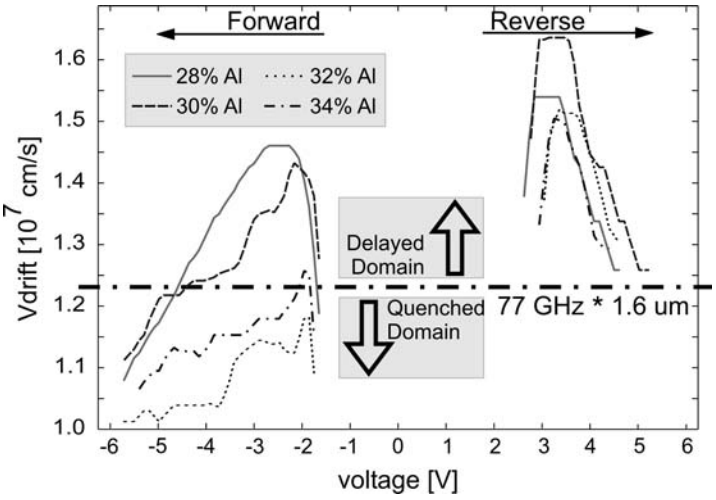

Figure 6.16: Drift velocity vs. bias voltage. Diode parameters: area=144 μm^2, active region length=1.6 μm, graded gap injector with maximum Al concentration from 28% to 34%.

The Quenched Domain mode. The resonant period of the circuit T_r is shorter than τ_d, but longer than the domain nucleation time τ_s:

$$\frac{1}{\tau_d} = \frac{v_{drift}}{L} < f_r < \frac{1}{\tau_s} \, . \tag{6.17}$$

Normally, a Gunn diode cavity oscillator has to be mechanically tuned, in order to get the largest power output at the corresponding desired frequency; comparing this target oscillating frequency with the drift velocity, the oscillating mode of the diode can be determined even before packaging. Different oscillation modes exhibit different powers, efficiencies and thermal stability properties [Hob72, Mak79].

In our case, a frequency of about 77 GHz is required, the active region is 1.6 μm long and a transit time mode is expected for drift velocities around $v_0 = 1.23 \times 10^7 cm/s$. Drift velocities lower than v_0 correspond to the Quenched Domain mode, drift velocities higher than v_0 correspond to the Delayed Domain mode. Sample with high Al content in the injector (32% and 34%) can oscillate at 77 GHz only in the Quenched Domain mode.

In the case of a second harmonic oscillator, the required frequency is 38.5 GHz and the only operating mode is the Delayed Domain for all the considered structures.

This qualitative analysis, summarized in Fig. 6.15 and 6.16, does not need the complete exact circuit conditions but neglects one important parameter: the domain formation. In fact, the domain formation time and the corresponding dead-zone length can not be easily estimated from small signal measurements. The dead-zone, that is also responsible for temperature instabilities and high noise levels, is dramatically reduced with an optimized hot electron injector.

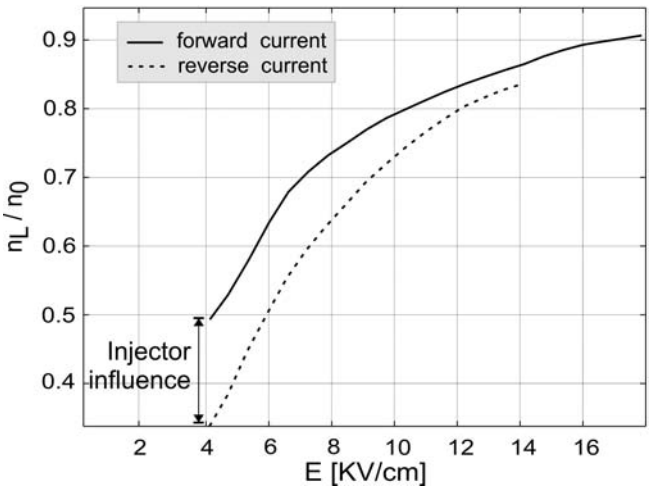

Figure 6.17: L-valley occupation for different electric fields; forward and reverse current directions (solid and dotted curve); injector with 32% Al concentration and active region 1.6 μm long.

6.2.4 Estimation of the Γ and L-valley occupation

From the determined drift velocities, quantitative values of the occupation of the Γ- and L-valley can be obtained. The drift velocity should be considered as the average of the high electron velocity in the Γ-valley and the low electron velocity in the L-valley. Defining n_Γ, n_L, μ_Γ, μ_L as the carrier concentrations and the mobility of electrons in the two valleys, v_d and f_{NCM} can be rewritten as:

$$v_d = \frac{\mu_\Gamma n_\Gamma + \mu_L n_L}{n_\Gamma + n_L} E, \tag{6.18}$$

$$f_{NCM} = \frac{\mu_\Gamma n_\Gamma + \mu_L n_L}{n_\Gamma + n_L} \frac{E}{L}. \tag{6.19}$$

As seen in Eq. (6.19), the change in f_{NCM} is caused by a change in the ratio between n_Γ and n_L. From the I-V characteristics (low voltages), we expect that the voltage drop on the injector is not symmetric in the forward and reverse directions. In order to have a reliable value of the electric field E in the active region, an accurate computation of the voltage drop on the injector has to be performed. For this purpose, results from Silvaco [Int] commercial package and manual fitting with a load-line model have been compared and taken into account. From Hall measurements of calibration samples, the Γ-valley electron mobility has been determined to be $\mu_\Gamma = 5000\ \frac{cm^2}{Vs}$. According to McCumber ($\mu_L = 100\ \frac{cm^2}{Vs}$ [MC66]) and to Hakki ($\mu_L = 200\ \frac{cm^2}{Vs}$ [Hak67]) the L-valley mobility has been assumed 40 times lower than the Γ-valley one.

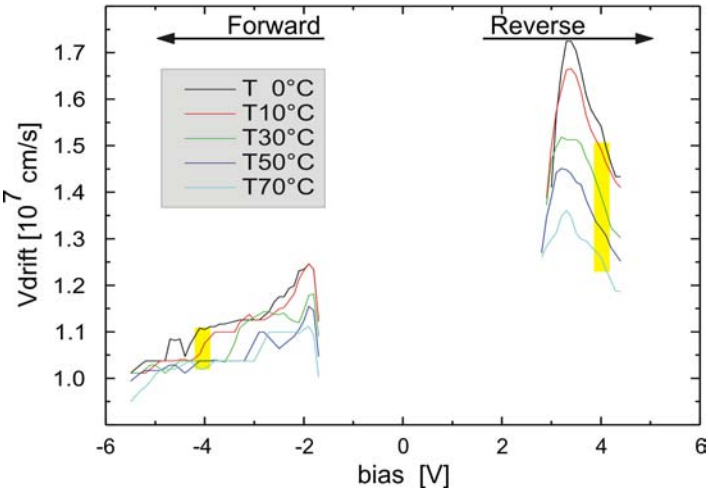

Figure 6.18: Drift velocity vs. bias voltage for different temperatures. Diode parameters: graded gap injector with maximum Al concentration 32%, area=144 μm^2, active region length=1.6 μm.

Considering $n_0 = n_\Gamma + n_L$ as the carrier concentration in the active region ($n_0 = 1.1 \cdot 10^{16}\, cm^{-3}$), n_L/n_0 can be expressed by:

$$\frac{n_L}{n_0} = \frac{\mu_\Gamma - \frac{L \cdot f_{NCM}}{E}}{\mu_\Gamma - \mu_L} \,. \tag{6.20}$$

The experimentally determined ratio of the carrier concentration in the L-valley (n_L/n_0) versus the electrical field E is presented in Fig. 6.17 for the structure with 32% aluminium content. It can be easily recognized the effectiveness of the injector, which is responsible for the occupation difference between the two current directions: this occupation difference decreases with E as the L-valley carrier concentration saturates at high electric fields.

6.2.5 Temperature dependance of the drift velocity

The Gunn diode temperature stability is a well known problem and has already been the topic of many publications ([Hob72, Mak79]) in the 1970's. Starting from a traditional approach, it is possible to identify five parameters, which concurrently contribute to the temperature dependance of the diode susceptance: low field mobility, domain transit time, domain formation, domain extinction and dielectric constant.

In this section, temperature dependant S-parameters are analyzed, showing how the Gunn diode hot electron injector influences the domain transit time and the domain creation. In order to change the active layer temperature of the diode, a custom designed

heating arrangement was used: the measurements were performed at room temperature with no need to recalibrate the network analyzer. The substrate was in contact with a copper block cooled or heated by a temperature controlled peltier element (for more details see chapter 4.7.1).

From the measured S-parameters, the temperature dependant drift velocity has been found as a function of the bias voltage (see section 6.2.3). As expected, the drift velocity decreases with increasing temperatures: for the same bias voltage, at 70 °C the drift velocity is lower than at 0 °C. At 70 °C more electrons occupy the L-valley, decreasing the average drift velocity. Figure 6.18 shows the described effect for a Gunn diode with a graded gap injector. Yellow boxes delimit the change of the drift velocity with the temperature at $+4\ V$ and $-4\ V$. It can be easily noticed, that the box in the forward current direction is much smaller than the box in the reverse direction. In other words, the considered diode is more temperature stable in the forward direction, where the graded gap injector is designed to work. Moreover, the drift velocity change with temperature of a Gunn diode with a graded gap injector is three times less than the one of a Gunn diode without a hot electron injector.

6.3 Gunn diode based oscillators

In the previous two sections, a detailed description of the main aspects concerning the electrical behaviour of single Gunn diodes has been presented. Further on, two examples of microwave voltage controlled oscillators[2] are discussed: a cavity waveguide Gunn oscillator and a MMIC Gunn oscillator. Both of them are based on a graded gap injector GaAs Gunn diode. The first VCO represents the classical solution, it is commercially available and combines good performances for a reasonable price. The second VCO is an attempt to integrate a planar resonating circuit with a Gunn diode, directly on the GaAs substrate used to grow the diode structure. The design of the coplanar wave guide (CPW) low-pass filter and of the complete planar oscillator is based on comparison of simulations with measurements.

6.3.1 The Gunn diode cavity oscillator

After the packaging, the Gunn diode chip is mounted in a resonant cavity. The current waveform of the Gunn diode is non-sinusoidal, so that higher harmonics of the fundamental frequency can be achieved. Typical cavity oscillators allow a fundamental or a second harmonic frequency generation. In the latter case, the Gunn diode is embedded in a resonator and the second harmonic is coupled out through a waveguide, which is below cutoff for the fundamental frequency. The resonator may consist in a part of the cavity itself [Bar81], or in a combination of a disk and a post in a coaxial configuration [Ond79].

The basic design of a cavity Gunn oscillator is shown in Fig. 6.19. The Gunn diode chip is pressed and fixed on the bottom of the cavity. In this way, the diode is automatically

[2] A variable frequency oscillator, whose frequency is varied by means of an applied control voltage, is called voltage-controlled-oscillator (VCO)

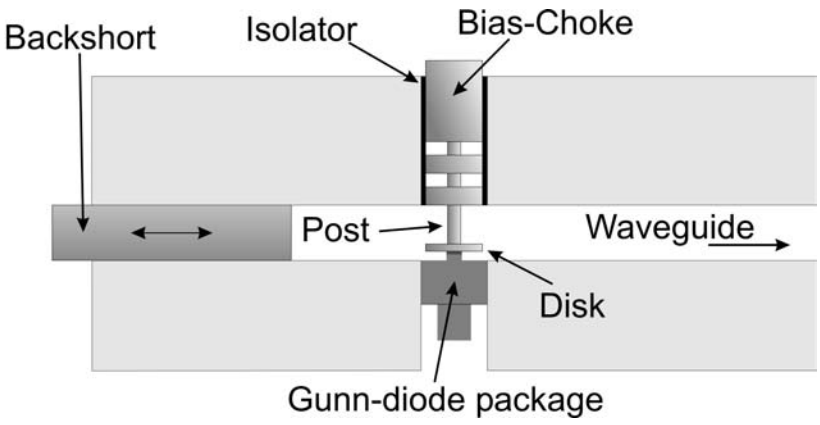

Figure 6.19: Cross sectional view of a typical Gunn diode cavity oscillator.

electrically grounded. On the top of the diode, the anode contact is connected to a disk and a post. Changing the diameter of the disk and the length of the post, it is possible to tune respectively a parallel capacitance and a series inductance. The post is combined with a bias choke from which the DC power is provided. The bias choke, which is carefully isolated from the waveguide cavity, is designed as an efficient low-pass filter, in order not to loose any HF power in the DC supply connection. In Fig. 6.19, one can see also a back-short: it is required to mechanically tune the oscillator response. Another adjustable side-short can be moved perpendicular to the cross section plane. The back-short influences strongly the oscillator power and the side-short allows a fine tuning of the frequency.

The typical behavior of a second harmonic cavity oscillator is presented in Fig. 6.20. The oscillator contains a graded gap injector Gunn diode with a maximum Al concentration of 32% and a 1.6 μm long GaAs active region. The frequency and power characteristics versus the bias voltage have been measured in CW conditions (no pulses). The Gunn diode starts to oscillate at 1.4 V, slightly after the threshold voltage. The turn on voltage, V_{ON} (the voltage above the threshold at which coherent RF power is obtained) can be found around 3 V. Between the threshold and the turn on voltage, the oscillations are incoherent. This incoherent regime is not usable; it is similar to the situation existing in a laser diode before the threshold current. From 3 to 6 V the frequency increases monotonically with the bias voltage.

6.3.2 The planar low pass filter

The miniature low-pass filter, used in the MMIC Gunn oscillator, consists in a slow-wave periodic structure proposed by Sor et al. [SQI01]. The main goal is to increase the effective capacitance and inductance along the CPW line. The inductance is enhanced reducing the CPW center conductor width and further capacitances to the ground are

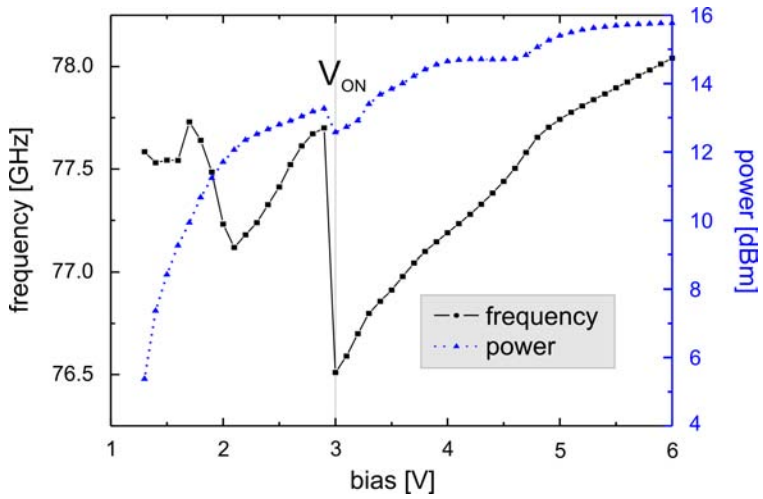

Figure 6.20: Frequency and output power, solid and broken curve, vs. voltages for a graded gap injector Gunn diode second harmonic cavity oscillator [Pro04].

created branching out the center conductor and the two grounds. The form of the cell with the equivalent lumped element circuit is illustrated in Fig. 6.21.

Two cell and three cell configurations with 1 *mm* and 0.8 *mm* length per cell respectively, have been considered. For both of them, the scattering parameters have been simulated and measured. A detailed description of the measurement equipment can be found in section 4.7.1. The low-pass filter has been designed and simulated using Sonnet Design Suite V.9 [V.903]

Figure 6.22 shows the response of a periodic low-pass filter with three 0.8 *mm* long cells. A good match between the simulated and experimental S-parameters can be noticed. The excellent periodic low-pass filter capabilities demonstrated in [SQI01] have been confirmed. With 1 *mm* long cells, the cutoff frequency decreases. This can be

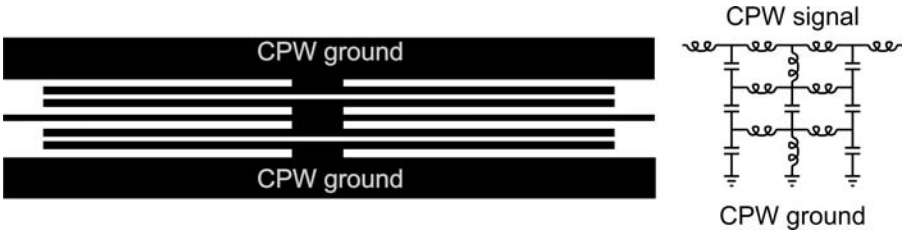

Figure 6.21: Schematic view and equivalent circuit of an unit cell of the periodic low pass filter.

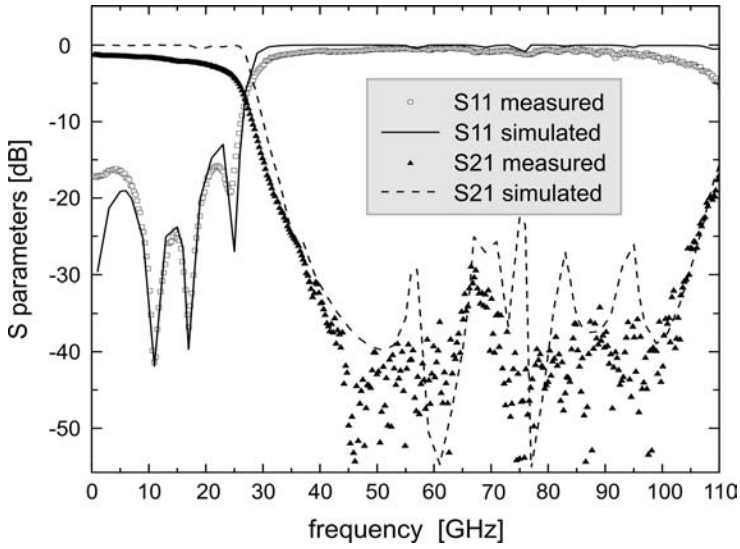

Figure 6.22: Simulated and measured response of the three cell, periodic low-pass filter. The unit cell length is 0.8mm.

understood considering that, with the same effective dielectric constant, the cut-off frequency is inverse proportional to the cell length.

The influence of the cell number is demonstrated in Fig. 6.23, where two and three cell low-pass filter are presented. A sharper roll-off can be accomplished simply by inserting more cells. On the other hand, adding cells can be seen as a disadvantage, if the integrated circuit size is a priority. The two cell low-pass filter with 1 mm long units resulted in the best tradeoff between performance and size.

In conclusion, the periodic structure has demonstrated a compact size, low insertion losses at low frequencies (pass-band region), high attenuation levels at high frequencies (band-stop region) and a simple filter synthesis and fabrication.

6.3.3 The planar resonant circuit

A schematic view of the voltage controlled oscillator (VCO) is shown in Fig 6.24. Even if the Gunn diode is a two terminal device, it has been implemented in a two port configuration. The first port is connected to the resonator and the second one leads to the coupler and to the low-pass filter for the DC supply. All the passive elements have been simulated with Sonnet Design Suite V.9 [V.903]. The coupler consists in an interdigitated capacitor with 5 fingers. Two kinds of resonators have been examined: the first one combines a coplanar line and two hairpins, the second one combines a slightly shorter coplanar line with a double T structure. Both of them are variations of the basic $\lambda/2$ resonator.

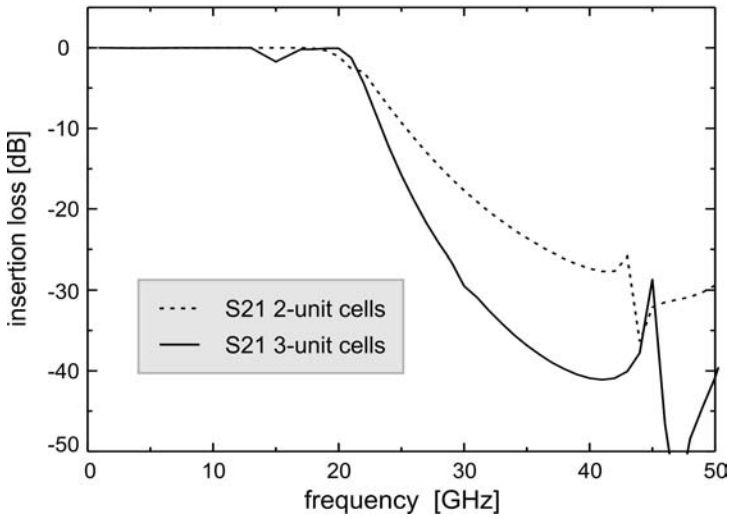

Figure 6.23: Effect of additional cells on the low-pass filter roll-off. Simulated insertion loss of two and three cell. The unit cell length is 1 mm.

The oscillator design started from DC and S-parameters measurement data of the planar graded gap injector Gunn diode, as described in section 6.2.2.

The oscillating frequency is given by the generalized oscillating condition

$$Y_d + Y_L = 0 \,, \tag{6.21}$$

where Y_d is the admittance matrix of the diode and Y_L is the admittance matrix for the passive elements. The diode conductance was negative over a wide frequency range, allowing us a simple design of the passive elements, using a short signal analysis. The simulation of the whole resonant circuit Y_L is much time consuming: it requires a 3 port computation (DC-in, HF-out and the diode input) and a high meshing precision of the passive elements (resonator, coupler an low-pass filter). For this reason, only the interval 25 to 60 GHz has been considered, assuming no oscillation could take place out of this range. For frequencies lower than 25 GHz, the low-pass filter influences Y_L and strong resonances could appear. These resonances, on the other hand, can not lead to oscillations, because the real part of diode admittance, $\mathrm{Re}(Y_d)$ is positive under 25 GHz.

The simulated response of the two considered circuits (at the diode port) is presented in Fig. 6.25 and in Fig. 6.26. The first one shows a resonance at 36 GHz and the second one at 44.5 GHz. The maximum intensity for the conductance is respectively 53 and 68 mS. Concerning the peak width, the 36 GHz resonance seems slightly sharper than the other one.

No direct measurement could confirm the computations: scattering parameters can not be measured in the considered configuration and the required layout change would

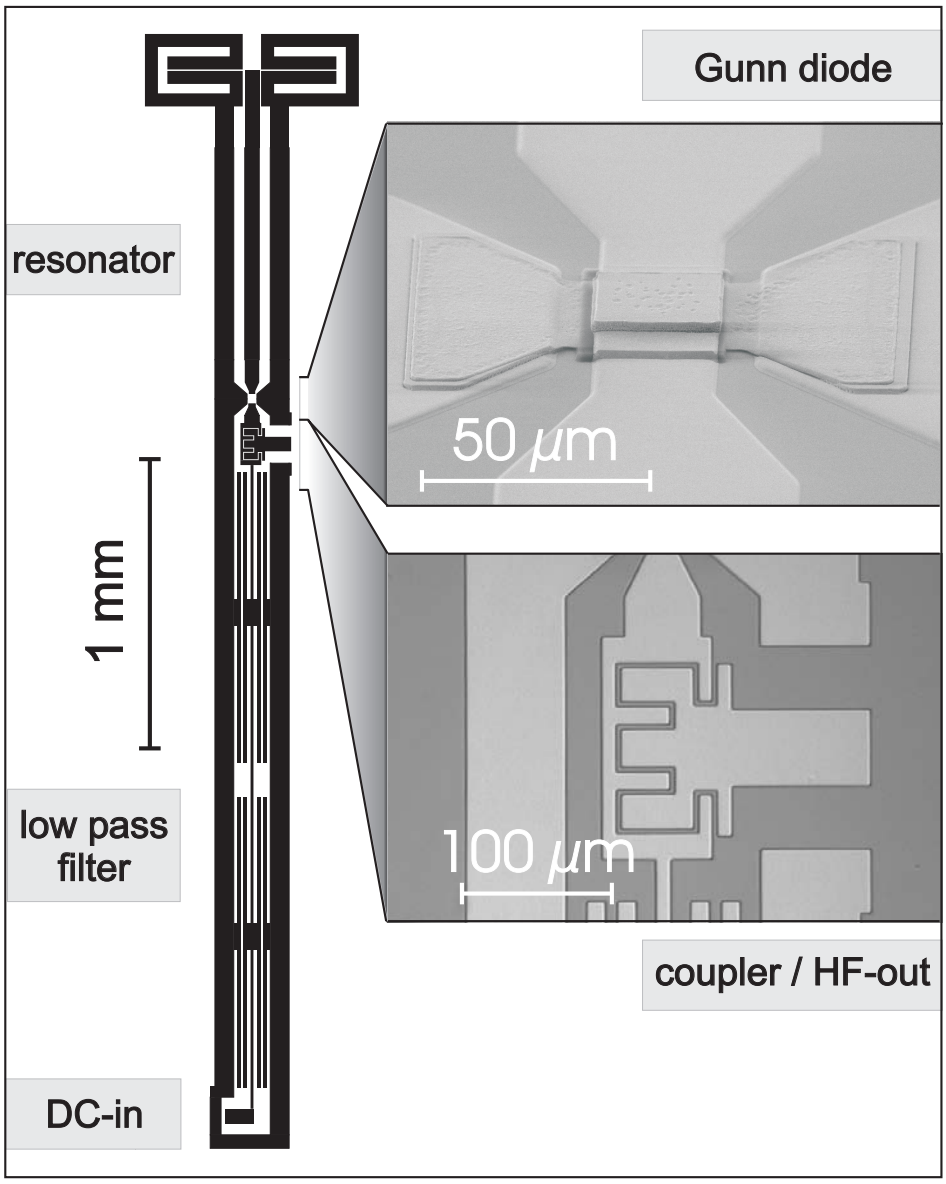

Figure 6.24: Typical Gunn diode MMIC voltage controlled oscillator layout.

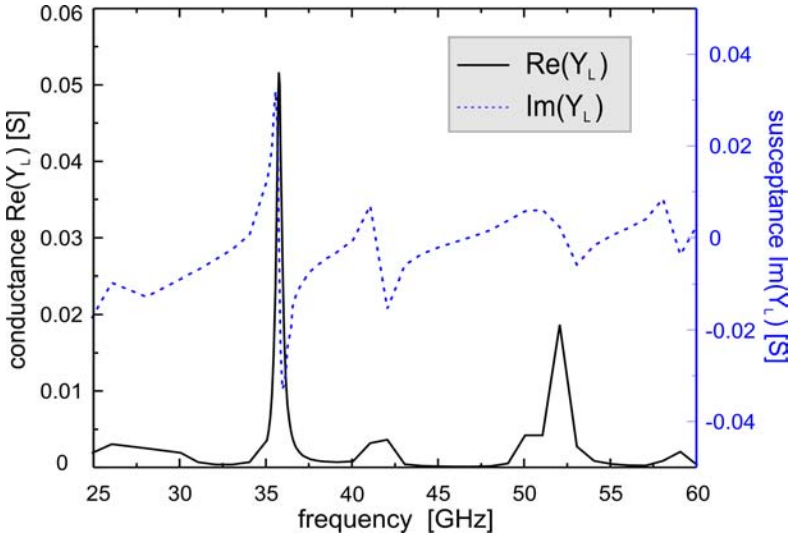

Figure 6.25: Conductance and susceptance, solid and broken curve, vs. frequency for the 36 GHz resonant circuit.

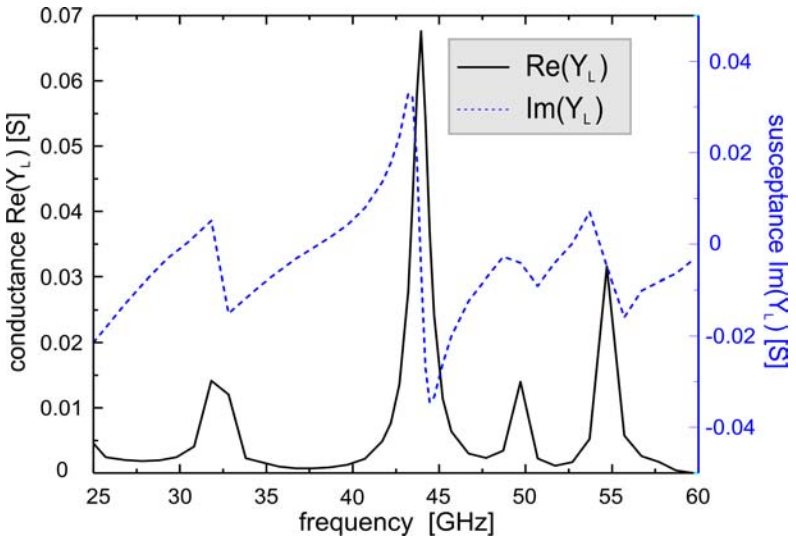

Figure 6.26: Conductance and susceptance, solid and broken curve, vs. frequency for the 44.5 GHz resonant circuit.

influence the wave propagation, probably creating artifacts. However, an indirect verification is provided in the next section, where the oscillation frequency for two oscillators based on the described resonant circuits is presented.

6.3.4 The monolithic integrated voltage-controlled Gunn oscillator

The implemented VCO was characterized using wafer probing and a measurement setup composed from a 40-GHz HP8564E spectrum analyzer, two Agilent 11970 (A and U) harmonic mixers and a DPM-2A power meter. The HP-R281A coaxial to waveguide transition connected the picoprobes to the waveguide inputs of the mixers and power meter. As explained in section 6.3.3, two different oscillating circuits have been considered.

In comparison with a cavity Gunn oscillator, the planar one does not require any mechanical tuning: no back-short or side-short are available. Frequency and power characteristics are fixed by the lithographic patterns. If this constitutes a big advantage in a mass production environment, in a research or early development stage, it reduces flexibility and restricts the tolerances for the impedance matching.

The frequency and the HF output power versus the Gunn diode tuning voltage of the first oscillator is shown in Fig. 6.27. After reaching the threshold voltage, the Gunn diode starts to oscillate. The frequency is not stable and more peaks can be seen in the spectrum analyzer. At 3.2 V, we have the so called turn-on voltage V_{ON}. After V_{ON}, the frequency starts to be stable and increases monotonously with voltage. The frequency varies from 36.65 GHz at 3.2 V to 37.55 GHz at 5.5 V. A typical behavior for a graded gap injector Gunn diode can be noticed: the turn-on voltage (3.2 V) is very close to the threshold (2.5 V). For this reason, a graded gap injector Gunn diode allows coherent oscillations over a wider voltage range compared with a standard Gunn diode [NDS$^+$89]. The frequency characteristics in Fig. 6.27 looks very similar to the one of the cavity oscillator (Fig. 6.20). The HF power can be scaled with the diode diameter and the efficiency is analogous.

The second planar oscillator with a different resonant circuit is presented in Fig. 6.28. At 4.5 V, it generates 46.5 GHz with a peak power of 3.77 mW. In this second oscillator, both the power and the frequency are higher than in the first one, but the voltage tuning of the frequency is inferior. Better tuning capabilities could be achieved adding to the second circuit a Schottky varactor.

A question remains. Why is the tuning range of the first oscillator about 1 GHz and the range of the second less than 30 MHz? Are the two tuning ranges related only to the quality factors of the respective resonant circuits? Actually, an operating mode switch could explain different pushing[3] behaviors. In section 6.2.3, a classification of the operating modes was proposed in connection to the drift velocity. 37 and 46 GHz would correspond to a velocity of $6 \times 10^6 cm/s$ and $7.4 \times 10^6 cm/s$, respectively. Remembering that all the measured graded gap injector Gunn diodes had a drift velocity higher than $9 \times 10^6 cm/s$, it can be concluded that both the planar oscillators are operated in the

[3]Frequency pushing is a measure of the sensitivity of the VCO output frequency to supply voltage, usually expressed in [MHz/V].

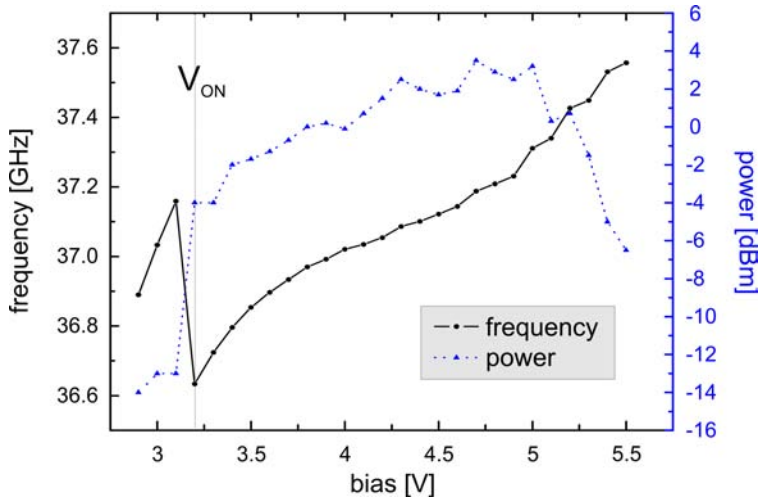

Figure 6.27: Frequency and output power, solid and broken curve, vs. bias voltage for a graded gap injector Gunn diode monolithic oscillator (resonant circuit I).

delayed domain mode.

A last consideration: the displayed power levels do not take into account the losses of the picoprobes and of the HF coaxial to waveguide transition. Estimating these losses, we expect that the total output power is with 2dB higher.

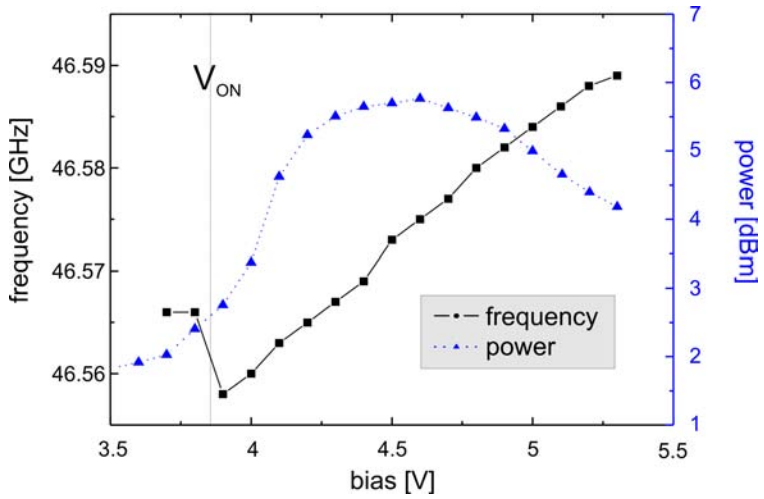

Figure 6.28: Frequency and output power, solid and broken curve, vs. bias voltage for a graded gap injector Gunn diode monolithic oscillator (resonant circuit II).

Chapter 7

Conclusions

In this thesis, Gunn diodes based on GaAs and GaN material systems were investigated with respect to microwave generation for automotive applications. Apart from the economical factor and the simple circuit requirement, the prerequisites for a microwave oscillator include: excellent frequency stability, adequate power output, low noise (in amplitude, frequency and phase modulation), variable tuning control and capability to be modulated in amplitude (AM), frequency (FM) or phase (PM). This dissertation describes the various efforts which were undertaken to improve Gunn diodes in order to achieve the targets described above.

The fabrication technology for planar GaAs and GaN Gunn diodes was developed and optimized. The GaAs Gunn diode structures were grown by MBE on 2-inch semi-insulating GaAs substrates in a Varian ModGen II machine and the GaN structures by MOVPE on 2-inch Al_2O_3 substrates in an AIXTRON reactor at the Institute of Thin Films and Interfaces of Forschungszentrum Jülich. After the epitaxial growth, $2.2 - 3.0\ \mu m$ deep mesas have been processed. Dry etching has been chosen, because it allows an exact definition of the mesa, prevents unwanted under-etching and provides smooth and nearly vertical side-walls. The demand of deep mesas required high etch rates, which were achieved with a chlorine based ECR Reactive Ion Etching. In the case of GaN, standard Ti etching masks have been replaced by Ni ones, improving the etching selectivity five times. Self-aligned emitter and collector contacts have been deposited and alloyed. The devices have been electrically isolated with a wet chemical etching or Ar ion sputtering down to the semi-isolating substrate. The problem of the top contact (emitter) wiring was solved via low-parasitic air-bridges or with a top contact planarization, on which direct metal connections are deposited. By means of finite elemente temperature simulations, it has been demonstrated that the air-bridge choice improves dramatically the cooling of the diodes. The heat generated inside the active region of a Gunn diode corresponds to power densities higher than 140 kW/cm^2 for GaAs and 1 MW/cm^2 for GaN. A heat-sink is required to cool the active region and to improve the performance and the reliability of the device. In typical Gunn diodes, the substrate is removed and a gold heat-sink is plated to the bottom contact. The airbridge technology showed up to be a valid alternative to the bottom heat-sink, which is not compatible with a planar process.

During this work, two different hot electron injectors for GaAs Gunn diode have been examined: a graded gap injector (GGI) and a novel resonant tunneling injector (RTI). The main task of a hot electron injector is to transfer as many electrons as possible from the Γ-valley to the L-valley at the very beginning of the device active region.
Within the framework of the cooperation project between Forschungzentrum Jülich and Robert Bosch GmbH [Pro04], GGI GaAs Gunn diodes have been studied and optimized. High quality planar GGI Gunn diodes have been fabricated using an air-bridge low-parasitic planar technology. RF evaluation of their performance up to 110 GHz shows the effectiveness of different graded gap injectors. The best results were found for graded AlGaAs barriers with maximum Al contents of 32% and 34%. An estimation of the possible operational modes is given for diodes used as microwave generators at 77 GHz, with application in automotive radar systems.
A second hot electron injector, the GaAs/AlAs double barrier resonant tunnelling injector has been proposed and designed. The RTI has been numerically simulated employing self-consistent real-time Green's functions [IM], in order to match the first transmission energy level for the given current density range ($23 - 27\ kA/cm^2$) to the energy gap between the L- and the Γ-valley. GaAs Gunn diodes with RTI have been successfully fabricated and characterized. RTI Gunn diodes present clear evidence of the injector effectiveness both in DC and RF conditions. A comparison between the experimental results of traditional GGI Gunn diodes and novel RTI Gunn diodes is provided, pointing out the role of the two injectors in DC and at high frequencies.

The design, processing and characterization of a novel GaAs Gunn diode based VCO-MMIC[1] fulfilled the second objective of this work. A good integration of a planar GGI Gunn diode with a CPW resonator, a periodic slow-wave low-pass filter and interdigitated HF coupler resulted in a compact size. A maximal power of 3.77 mW at 46 GHz is reported. Further increase of the power output should be achieved by increasing the Gunn diode area and connecting the device top contacts with thick airbridges. A simple and straightforward processing technology makes our proposed microwave generator competitive with cavity oscillators and transistor based MMICs.

While the processing of the GaN Gunn diodes has been successfully completed, the measurement results of the fabricated diodes should be considered as preliminary. However, during the processing work, some new interesting results for nanoelectronic devices have been obtained. Our early GaN etching tests demonstrated the possibility to fabricate GaN nanocolumns with a simple and reproducible method. Among different types of nanostructures, the nanowires and nanotubes appeared to be extremely interesting as building blocks for nanoelectronics. In our novel top down approach, the nanowhiskers were processed via ECR-RIE etching GaN layers grown by MOVPE. With the advantage of a physical etching, nanocolumns with arbitrary doping concentration as well as thin AlN layer can be fabricated.

[1] Voltage Controlled Oscillator Monolithic Microwave Integrated Circuit.

Chapter 8

Zusammenfassung

In der vorliegenden Arbeit werden Gunn-Dioden, basierend auf den Materialsystemen GaAs und GaN, hinsichtlich der Mikrowellenerzeugung in der Automobil-Branche untersucht. Zusätzlich zu den ökonomischen Faktoren und der Anforderung an einfache Schaltkreise, sind für die Mikrowellenoszillatoren folgende Eigenschaften erforderlich: exzellente Frequenzstabilität, ausreichende Ausgangsleistung, geringes Rauschniveau (in Amplitude, Frequenz und Phasenmodulierung), variable Frequenzabstimmung und die Fähigkeit in Bezug auf Amplitude (AM), Frequenz (FM) oder Phase (PM) moduliert zu werden. Diese Dissertation beschreibt die vielseitigen Bemühungen, die unternommen wurden um die Gunn-Dioden im Hinblick auf die oben genannten Eigenschaften zu verbessern.

Es wurden Herstellungstechniken für planare GaAs und GaN Gunn-Dioden entwickelt und optimiert. Das Wachstum der GaAs Gunn-Diodenstrukturen erfolgte auf einem 2 Zoll semi-isolierenden GaAs Substrat mittels einer MBE Varian ModGen II Anlage; das der GaN Gunn-Diode auf einem 2 Zoll Al_2O_3 Substrat mittels eines MOVPE AIXTRON Reaktors im Institut für Schichten und Grenzflächen des Forschungszentrums Jülich. Nach dem Epitaxiwachstum wurden 2.2 bis 3.0 μm tiefe Mesas hergestellt. Um glatte und nahezu vertikale Seitenwände zu erhalten, wurde die Trockenätzung gewählt. Außerdem verhindert diese Methode die ungewollte Unterätzung und erlaubt eine exakte Definierung der Mesa. Die Forderung nach tiefen Mesas verlangt hohe Ätzraten, welche durch einen chlorbasierten ECR-Ätzprozess erreicht werden konnten. Im Fall von GaN wurden die konventionellen Ti-Masken durch Ni-Masken ersetzt. Es kam damit zu einer Steigerung der Selektivität des Ätzens um ein Fünffaches. Selbstjustierende Emitter und Kollektorkontakte wurden aufgedampft und einlegiert. Die elektrische Isolierung des Bauelements erfolgte mittels Nassätzung oder Ar Ionensputtern bis zum semi-isolierenden Substrat. Das Problem der Kontaktierung des Topkontaktes (Emitter) konnte gelöst werden durch eine niedrig-parasitäre Airbridge bzw. durch eine Topkontakt-Planarisierung auf die direkt Metallverbindungen aufgedampft wurden. Mittels Finite Elemente Temperatursimulierung konnte demonstriert werden, dass die Airbridges die Kühlung der Diode sehr stark verbessern. Die Hitze, die in der aktiven Schicht der Gunn-Diode entsteht, entspricht einer Leistungsdichte von größer 140 kW/cm^2 (GaAs) bzw. 1 MW/cm^2 (GaN). Eine Wärmesenke ist zur Kühlung der aktiven Schicht notwendig und trägt somit zu

einer verbesserten Leistung und Zuverlässigkeit des Bauelementes bei. In herkömmlichen Gunn-Dioden wurde das Substrat entfert und eine Wärmesenke aus Gold auf den Untergrund aufgetragen. Die Airbridge stellt eine gute Alternative zu dieser Bottomwärmesenke dar, welche nicht kompatibel mit planaren Prozessen ist.

Innerhalb dieser Arbeit konnten zwei verschiedene hot electron injectors für Gunn-Dioden herausgearbeitet werden: graded gap injector (GGI) und resonant tunneling injector (RTI). Die Hauptaufgabe eines hot electron injectors ist der Transfer von möglichst vielen Elektronen vom Γ- zum L-Valley zu Beginn der aktiven Schicht des Bauelementes. Im Rahmen der Zusammenarbeit des Forschungszentrums Jülich mit der Robert Bosch GmbH erfolgte die Untersuchung und Optimierung von GGI GaAs Gunn-Dioden[Pro04]. Qualitativ hochwertige planare GGI Gunn-Dioden wurden hergestellt, unter der Verwendung von Airbridges mit niedrig-parasitärer planarer Technologie. Die Beurteilung des RF-Verhaltens bis 110 GHz zeigt die Effektivität der verschiedenen graded gap injectors. Die besten Resultate konnten für gegradete AlGaAs Barrieren mit einem maximalen Al-Gehalt von 32% und 34% erzielt werden. Dargestellt ist eine Abschätzung der möglichen Arbeitsmodi für Dioden, welche als Mikrowellenerzeuger bei 77 GHz in Radarsystemen in der Automobilbranche Einsatz finden.
Ein zweiter neuer hot electron injector, der GaAs/AlAs Doppelbarrieren-RTI konnte erfolgreich vorgeschlagen und gestaltet werden. Der RTI wurde numerisch selbstkonsistent simuliert mittels Realzeit-Green-Funktionen. Ziel dabei war die Anpassung des ersten Transmissionsenergieniveaus für einen gegebenen Stromdichtebereich ($23 - 27\ kA/cm^2$) an den Energieunterschied zwischen dem L-Valley und dem Γ-Valley. GaAs Gunn-Dioden mit RTI wurden hergestellt und charakterisiert. Für beide DC und RF Bedingungen zeigt die RTI Gunn-Diode deutliche Beweise für die Effektivität des injectors. Der Vergleich der experimentellen Ergebnisse der herkömmlichen GGI Gunn-Dioden mit denen der neuen RTI Gunn-Dioden zeigt die Bedeutung der beiden Injektoren bei DC und Hochfrequenzen.

Die Gestaltung, Prozessierung und Charakterisierung von neuartigen monolitisch integrierten Oszillatoren (MMIC-VCO) basierend auf einer GaAs Gunn-Diode, erfüllt die zweite Zielsetzung innerhalb dieser Arbeit. Dank der guten Integration einer planaren GGI Gunn-Diode mit einem CPW Resonator, einem periodischen slow-wave Tiefpassfilter und einem fingerförmigen HF-Koppler, ist der Oszillator sehr kompakt. Eine maximale Leistung von 3.77 mW bei 46 GHz konnte ermittelt werden. Die weitere Zunahme der Ausgangsleistung könnte durch eine Vergrößerung der Gunn-Dioden-Fläche und durch eine Verwendung von dicken Airbridges erreicht werden. Aufgrund der einfachen und direkten Prozessierungstechnologie ist unsere vorgeschlagene Mikrowellenerzeugung konkurrenzfähig zu Hohlraumresonator-Oszillatoren und transistorbasierten MMICs.

Während die Prozessierung von GaN-Gunn Dioden vollständig erarbeitet wurde, sind die Meßergebnisse an den hergestelten Dioden als vorläufig anzusehen. Jedoch, wurde im Rahmen der Prozessierungsarbeit ein für zukünftige Nanobauelemente interessantes neues Ergebnis gefunden. Die ersten GaN Ätztests demonstrierten die Möglichkeit zur Herstel-

lung von Nanosäulen mit einer einfachen und reproduzierbaren Methode. Innerhalb der verschiedenen Nanostrukturen, sind Nanowires und Nanotubes die erfolgversprechendsten Bauteile für eine zukünftige Nanoelektronik. In unserer neuen *topdown* Betrachtungsweise wurden die Nanosäulen mittels ECR-RIE Ätzung aus den durch MOVPE gewachsenen GaN-Schichten hergestellt.

Appendix A

Mask layout

All sets of masks used in this work were designed and fabricated at IGS-1 in Forschungszentrum Juelich. The optical lithography mask consists of a glass plate (commonly quartz, borosilicate glass or fused-silica) on which chromium patterns are defined by means of electron beam lithography. In this appendix, a brief overview of the mask layouts is presented focusing on the polyamide planar process (see section 5). Each step of the device preparation required an optical lithography mask:

1. mesa definition by reactive ion etching;
2. self aligned ohmic contacts deposition;
3. diode electrical isolation etching;
4. diode planarization / passivation;
5. bond-pads, low-pass filter and resonant circuit deposition.

Steps 1, 2 and 5 rely on a positive lithographic process, and steps 3 and 4 on a negative one.
In the case of the air-bridge process, two further layers are required. A detailed explanation of the optional air-bridge process is given in section 5.6.

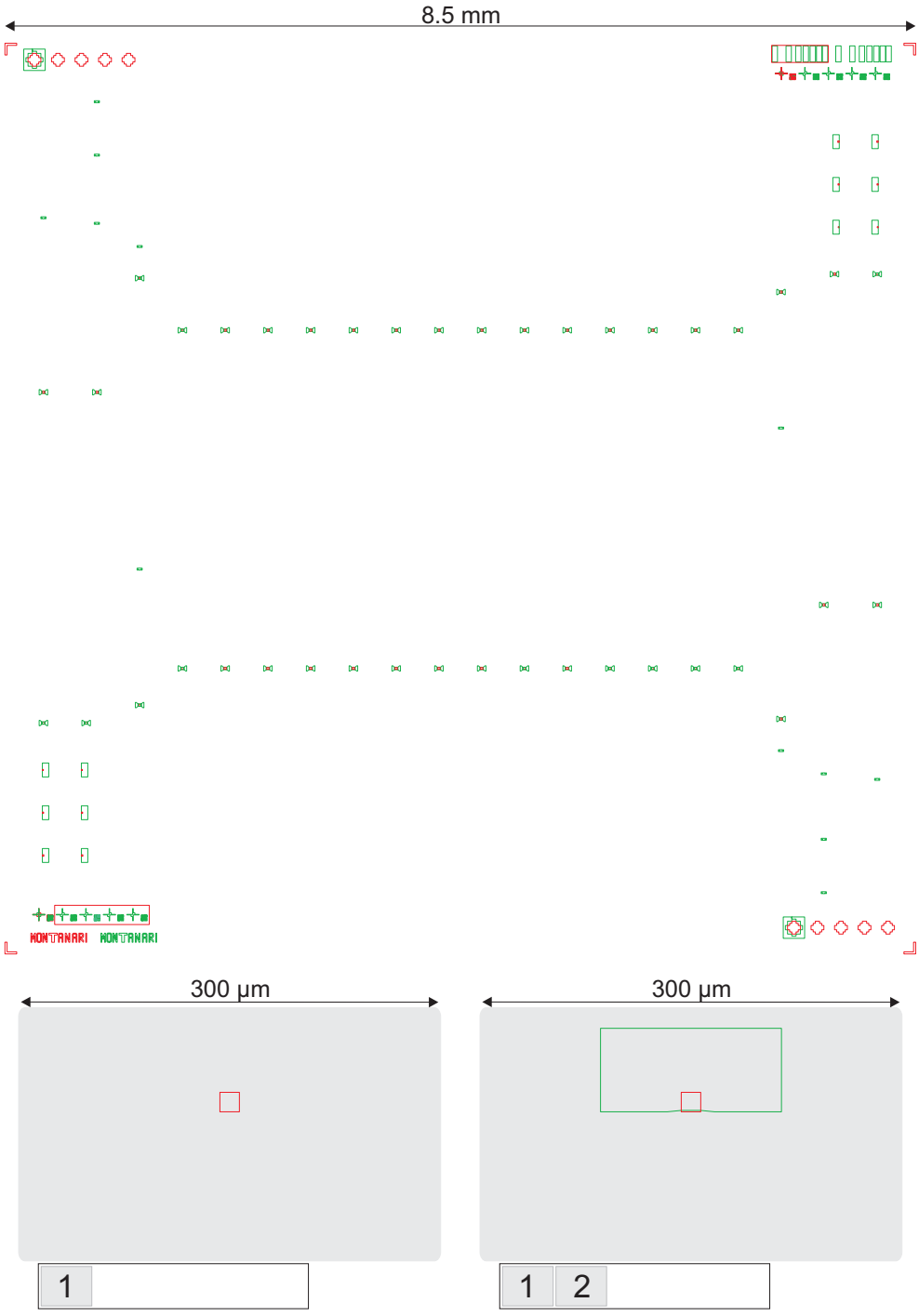
8.5 mm
MONTANARI MONTANARI
300 µm
300 µm
1
1 2

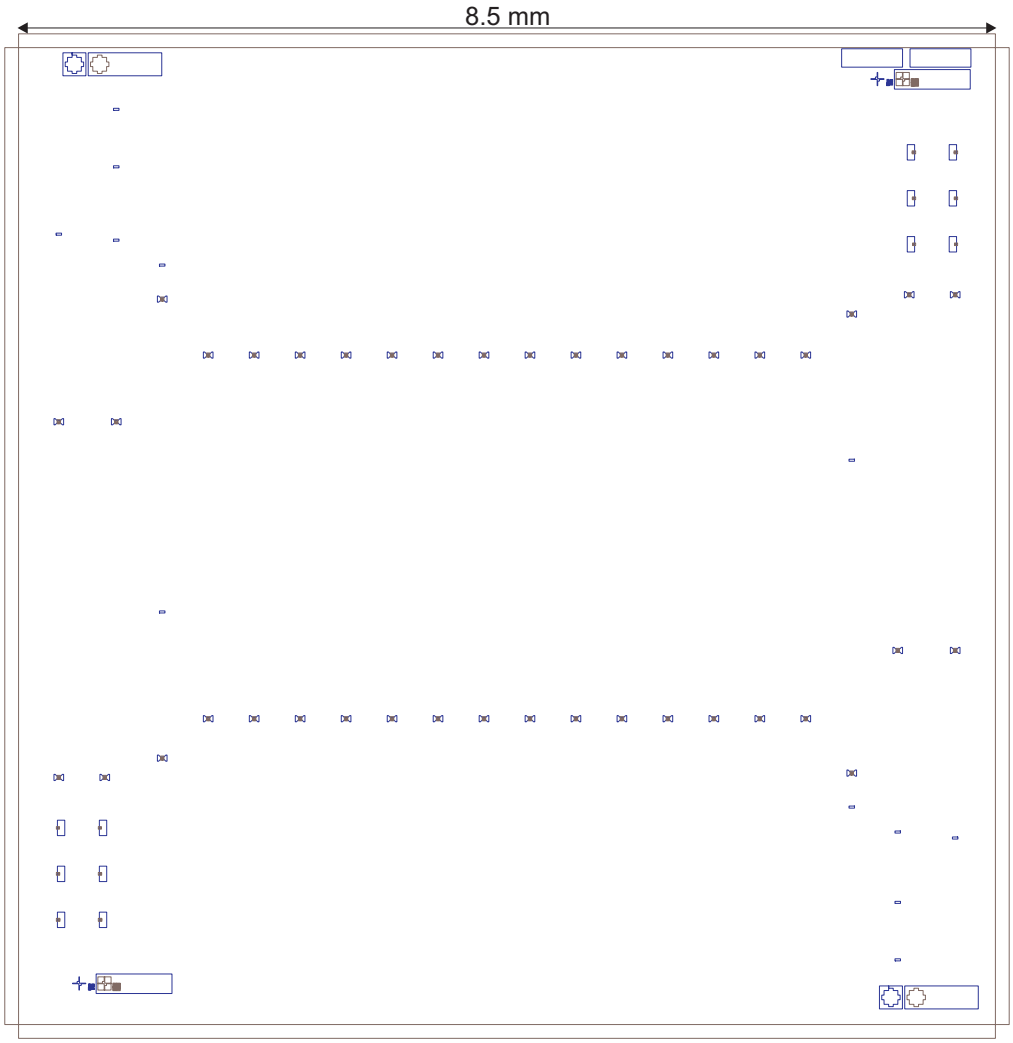
8.5 mm

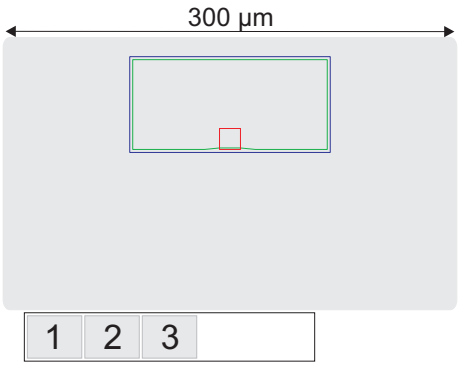
300 µm
1
2
3

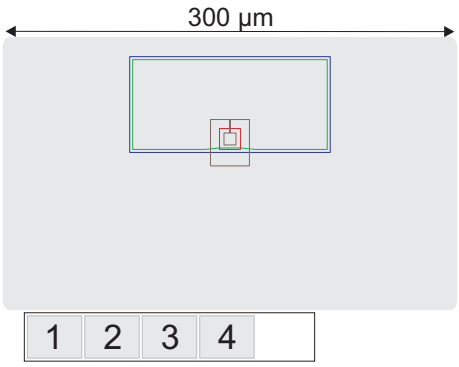
300 µm
1
2
3
4

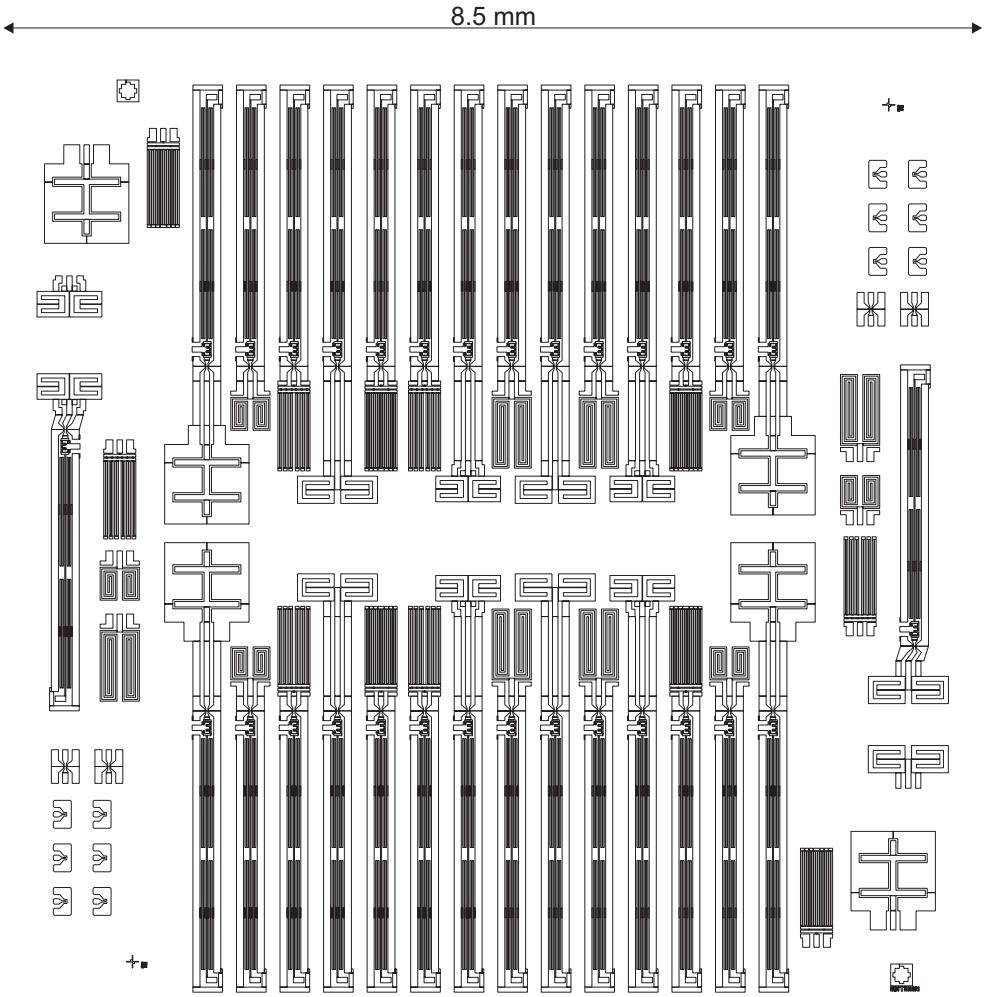
8.5 mm

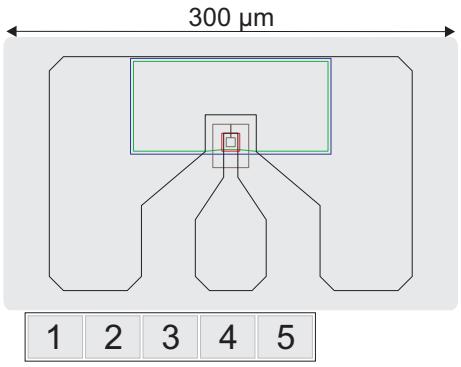
300 µm
1
2
3
4
5

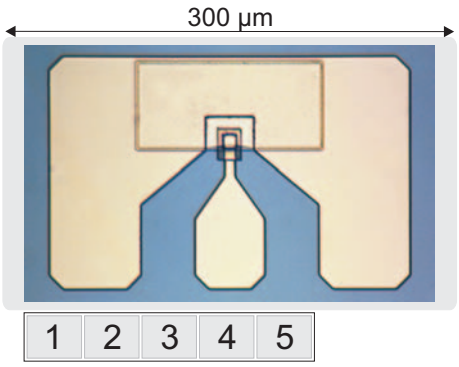
300 µm
1
2
3
4
5

Appendix B

Properties of semiconductors and table of elements

Table B.1: Properties of semiconductors at room temperature.

Properties	**Ge**	**Si**	**GaAs**	**ALAs**	**GaN**	**AlN**
crystal structure	diamond	diamond	zinc-blende	zinc-blende	zinc-blende	zinc-blende
density [g/cm^3]	5.32	2.33	5.32	3.81	6.15	3.23
lattice const. [Å]	5.646	5.431	5.653	5.662	3.189	3.112
atom/molecule density [cm^{-3}]	4.4×10^{22}	5×10^{22}	4.4×10^{22}	4.59×10^{22}	8.9×10^{22}	9.58×10^{22}
dielectric const. ϵ_r	16	11.8	13.1	10.9	8.9	8.5
energy gap Eg [eV]	0.67	1.12	1.43	2.16	3.39	6.2
breakdown field [kV/cm^2]	100	300	400	600	5000	1200
melting temperature [C]	937	1412	1240	1740	2500	3273
thermal capacity [J/kgK]	310	703	320	450	490	600
thermal conductivity [W/cmK]	0.58	1.3	0.45	0.91	1.3	2.85

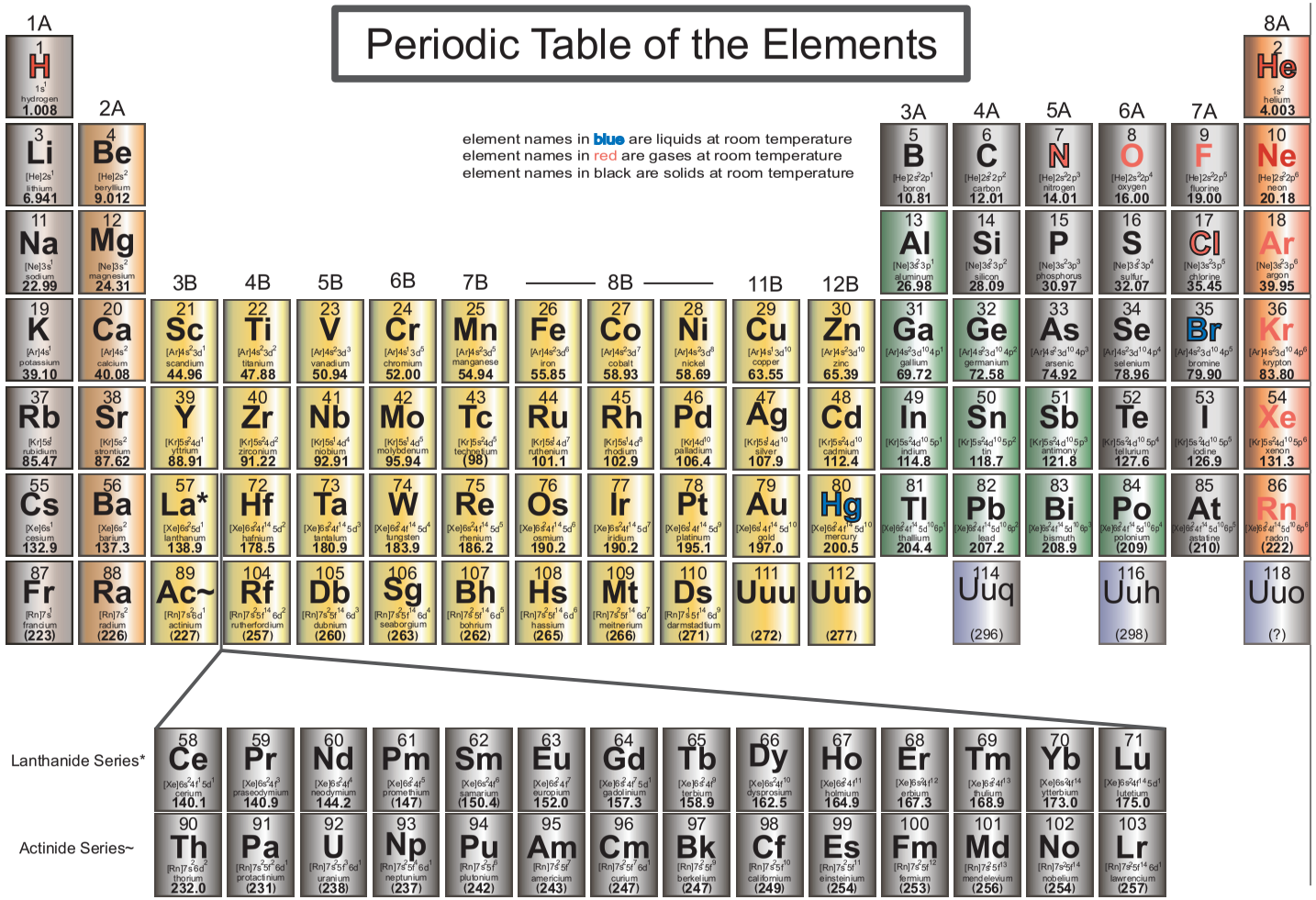
Periodic Table of the Elements
element names in blue are liquids at room temperature
element names in red are gases at room temperature
element names in black are solids at room temperature
1A
2A
3B
4B
5B
6B
7B
8B
11B
12B
3A
4A
5A
6A
7A
8A
Lanthanide Series*
Actinide Series~

Appendix C

Process parameters

C.1 Cleaning process

Cleaning before photo-lithography

- immersion (with agitation) in acetone, 2 min
- immersion (with agitation) in 2-propanol, 2 min
- nitrogen blow drying
- hot plate drying, 170°C, 5 min
- visual inspection.

Cleaning before metallization: deoxidation of GaAs

- immersion in HCl : H_2O (1:4), 30 s
- rinse in deionized (DI) water, 2 min
- nitrogen blow drying.

Plasma cleaning after photo-lithography

- Oxygen plasma etching R.I.E. Slave-chamber (Prog. Resistschleier)
  - O_2-Flow 30 ml/min
  - pressure 20 μbar
  - μwave Power 200 W
  - time 20 s
- visual inspection.

Resist removal after etch process

- immersion (with agitation) in acetone, 6 min
- immersion (with agitation) in 2-propanol, 1 min
- nitrogen blow drying
- visual inspection.

ECR-Chamber cleaning before plasma-etch

- ECR-Chamber cleaning Step I: O_2 plasma
  - O_2-Flow 30 ml/min, upper gas line
  - pressure 4 μbar
  - magnets current: upper 185 A, lower 40 A
  - μwave power 750 W, RF power 50 W
  - cooling 0°C, with He-Flow 14 ml/min cooling circuit
  - time 20 min

- ECR-Chamber cleaning Step II: H_2-Ar plasma
  - H_2 flow 20 ml/min, upper gas line
  - Ar flow 10 ml/min, upper gas line
  - pressure 4 μbar
  - magnets current: upper 185 A,ťlower 25 A
  - μwave power 600 W, RF-power 50 W
  - cooling 0°C, with He flow 14 ml/min cooling circuit
  - time 10 min

C.2 Lithography processes

Edge removal - lacquering AZ 5214

- exposure UV 365 / 7 mW, 45 s for simple resist layer, 60 s for double resist layer
- development in AZ 326 MIF (1:1), 45 s
- rinse in DI water
- nitrogen blow drying

Positive process - lacquering AZ 5214

- *optional:* adhesion-improver hexamethyldisilazane (HMDS) spinning, 4000 U/min (Prog. 4)
- *optional:* soft bake on the hot plate, 90°C, 1 min
- AZ 5214 resist spinning, 4000 U/min (Prog. 4)
- soft bake on the hot plate, 90°C, 5 min
- *optional:* edge removal
- exposure UV 365 / 7 mW, 5.5 s
- development in AZ 326 MIF (1:1), 45-50 s
- rinse in DI water
- nitrogen blow drying

Positive process - lacquering AZ 4564, resist layer for plating air-bridges

- AZ 45644 resist spinning, 5000 U/min (Prog. 5)
- soft bake on the hot plate, 90°C, 10 min
- *optional:* edge removal
- exposure UV 365 / 7 mW, 40 s
- development in AZ 326 MIF (1:1), 135 s
- rinse in DI water
- nitrogen blow drying
- post bake in oven, 100°C, 30 min

Image-reversal process - lacquering AZ 5214, simple resist layer

- AZ 5214 resist spinning, 4000 U/min (Prog. 4)
- soft bake on the hot plate, 90°C, 5 min
- *optional:* edge removal
- exposure UV 365 / 7 mW, 3.3 s (3.5 s)
- reversal bake on the hot plate, 115°C, 2 min
- flat exposure UV 365 / 7 mW, 15 s (16 s)
- development in AZ 326 MIF (1:1), 23 s
- rinse in DI water
- nitrogen blow drying

Negative process - lacquering PMMA for E-Beam lithography

- PMMA 600 resist spinning, 6000 U/min (Prog. 6)
- hard bake on the hot plate, 180°C, 2 min
- PMMA 200 resist spinning, 6000 U/min (Prog. 6)
- hard bake on the hot plate, 180°C, 2 min
- PMMA 600 resist spinning, 6000 U/min (Prog. 6)
- hard bake on the hot plate, 180°C, 2 min
- E-Beam exposure $180\mu C/mm^2$ with proximity correction
- development in AR600-55, 150 s
- rinse in propanol
- nitrogen blow drying

Image-reversal process - lacquering AZ 5214, double resist layer

- AZ 5214 resist spinning, 4000 U/min (Prog. 4)
- soft bake on the hot plate, 90°C, 1 min
- AZ 5214 resist spinning, 4000 U/min (Prog. 4)
- soft bake on the hot plate, 90°C, 5 min
- *optional:* edge removal
- exposure UV 365 / 7 mW, 4 s
- reversal bake on the hot plate, 115°C, 2 min
- flat exposure UV 365 / 7 mW, 18 s
- development in AZ 326 MIF (1:1), 26 s
- rinse in DI water
- nitrogen blow drying

Negative process - lacquering Polyamide (Durimide 7510)

Lithography

- DURIMIDE 7510 spinning, 6000 U/min (Prog. 6)
- soft bake on the hot plate, 100°C, 5 min
- exposure UV 365 / 7 mW, 20 s
- wait 30 min
- development spraying HTR-D2, 25 s
- development in HTR-D2 : 2-propanol (1:1), 25 s
- development stop in 2-propanol
- nitrogen blow drying

Polyamide hardening in vacuum oven

- evacuate the oven
- linear ramp from 100°C (Stand-By temperature of the oven) up to 350°C, slope 300°C/h
- maintain 350°C for 1 h
- linear ramp from 350°C to 100°C, slope −150°C/h
- oven with nitrogen venting

C.3 Wet-chemical etching processes

GaAs etching with sulfuric acid for substrate removal

- H_2SO_4 : H_2O_2 : H_2O (1:8:40), etch-rate r $\approx 1.0\,\mu$m/min
- rinse in DI water,
- nitrogen blow drying

GaAs etching with sulfuric acid for mesa isolation

- H_2SO_4 : H_2O_2 : H_2O (1:8:80), etch-rate r $\approx 0.52\,\mu$m/min
- rinse in DI water,
- nitrogen blow drying

Selective Etching of GaAs over $Al_{0.6}Ga_{0.4}As$

- $C_6H_8O_7$: H_2O_2 (4:1), etch-rate for GaAs r $\approx 0.43\,\mu$m/min
- rinse in DI water,
- nitrogen blow drying

Selective Etching of $Al_{0.6}Ga_{0.4}As$ over GaAs

- HF (48%) : H_2O (1:1), 2 min (with slow agitation)
- rinse in boiling DI water
- rinse in DI water,
- nitrogen blow drying

Etching process for nickel removal

- 5 g $FeCl_3$: 100 ml ethyl-alcohol : 2 ml HCl
  or
- HCl 1: 1 H_2O_2 4 min
- rinse in DI water,
- nitrogen blow drying

Etching process for titan removal

- AF 91-9 [$(NH_4)HF_2$ buffered HF solution], 1-2 min (with slow agitation)
- rinse in DI water,
- nitrogen blow drying

C.4 Plasma-etching processes

ECR-RIE process for GaAs, AlGaAs mesas

- Cl_2 flux 8 ml/min, upper gas line
- H_2 flux 5 ml/min, upper gas line
- Ar flux 2 ml/min, upper gas line
- process pressure 2 μbar
- magnets current: upper 185 A, lower 25 A
- MW-power 265 W, RF-power 50 W
- cooling 0°C, with He flow 14 ml/min cooling circuit

ECR-RIE process for GaN mesas

- Cl_2 flux 20 ml/min, upper gas line
- Ar flux 3 ml/min, upper gas line
- process pressure 2.5-3 μbar
- magnets current: upper 185 A, lower 25 A
- MW-power 300 W, RF-power 30 W
- cooling 2°C, with He flow 14 ml/min cooling circuit

ECR-RIE process for GaN nanocolumns

- Cl_2 flux 16 ml/min, upper gas line
- Ar flux 3 ml/min, upper gas line
- process pressure 2-2.5 μbar
- magnets current: upper 185 A, lower 25 A
- MW-power 300 W, RF-power 60 W
- cooling 2°C, with He flow 14 ml/min cooling circuit
- (optional) 1 min RF on / 1 min RF off

RIE process for Polyimide (Durimide 7510)

- O_2-Flus 30 ml/min
- CF_4-Flus 1 ml/min
- process pressure 1 mbar
- power 100 W

C.5 Metallization processes

Ohmic contacts (for GaAs)

- 20 nm Ge / 15 nm Ni / 200 nm Au

Ohmic contacts (for GaN)

- 35 nm Ti / 200 nm Al / 50 Ni / 200 nm Au

Bond pads

- 30 nm Ti / 600 nm Au, rotating evaporation

Bond pads for polyamide process

- 50 nm Ti / 50 nm Au / 50 nm Ti / 650 nm Au, rotating evaporation

Air-bridge seed layer

- 1 nm Cr / 90 nm Au
  or
- 80 nm Au /10 nm Ti

Lift-Off process

- immersion (with agitation) in acetone, 5 min
- *optional:* ultrasound bath
- *optional:* syringe spray
- immersion (with agitation) in 2-propanol, 2 min
- nitrogen blow drying
- visual inspection.

Annealing of Ge/Ni/Au metallization in RTP oven

temperature profile

- ramp the temperature up to 130°C, 5 s, N_2 flux 3 l/min
- preheating, 130°C, 90 s, N_2-Flus 3 l/min
- ramp the temperature up to, 400°C, 5 s, N_2 flux 3 l/min
- keep the set temperature, 400°C, 75 s, N_2 flux 3 l/min
- cool down to room temperature, 240 s, N_2 flux 5 l/min

Annealing of Ti/Al/Ni/Au metallization in RTP oven

temperature profile

- ramp the temperature up to, 900°C, 5 s, N_2 flux 3 l/min
- keep the set temperature, 900°C, 30 s, N_2 flux 3 l/min
- cool down to room temperature, 240 s, N_2 flux 5 l/min

Gold galvanic plating

- plating bath preparation (2.5 l of solution)
  - heat 1.5 l PUR-A-GOLD 401 B up to 60°C and filtrate
  - dissolve 40.2 g $KAu(CN)_2$ (62.5%) in warm DI water
  - fill with DI water up to the final volume of 2.5 l
  - gold concentration 10 g/l, pH 5.8 (at 60°C), (bath 1.11 g/ml)
- 60°C, current density 0.5 A/dm^2, magnetic stirrer , agitate, r $\approx 0.25\,\mu m/min$
- rinse in DI water,
- nitrogen blow drying

List of Figures

List of Tables

Bibliography

[AM88] E.E. Altshuler and R.A. Marr. A comparison of experimental and theoretical values of atmospheric absorption at the longer millimeter wavelengths. *IEEE Transactions on Antennas and Propagation*, 36:1471, 1988.

[AP00] E. Alekseev and D. Pavlidis. Microwave potential of GaN-based Gunn devices. *Electronics Letters*, 36:176, 2000.

[AWR+98] J.D. Albrecht, R.P. Wang, P.P. Ruden, M. Farahmand, and K.F. Brennan. Electron transport characteristics of GaN for high temperature device modelling. *Journal of Applied Physics*, 83(9):4777–4781, 1998.

[Bar81] H. Barth. A wideband, backshort-tunable second harmonic W-band Gunn-oscillator. *1981 IEEE MTT-S International Microwave Symposium Digest*, page 334, 1981.

[BFH66] P. N. Butcher, W. Fawcett, and C. Hilsum. A simple analysis of stable domain propagation in the Gunn effect. *Brit. J. Appl. Phys.*, 17:841–850, 1966.

[BHT72] P.T. Bulman, G. S. Hobson, and B.C. Taylor. Transferred electron devices. *Academic Press London and Newyork*, 1972.

[BPBP93] R. Blundell, D.C. Papa, E.R. Brown, and C.D. Parker. Resonant tunnelling diode oscillator as an alternative LO for SIS receiver applications. *Electronics Letters*, 29:288, 1993.

[But65] P. N. Butcher. Theory of stable domain propagation in the Gunn effect. *Phys. Lett.*, 19(7):546–547, Dec. 1965.

[CBK+88] N. R. Couch, P. H. Beton, M. J. Kelly, T. M. Kerr, D. J. Knight, and J. Ondria. The use of linearly graded composition AlGaAs injectors for intervalley transfer in GaAs: Theory and experiment. *Solid-State Electron.*, 31(3/4):613–616, March-April 1988.

[CET74] L. L. Chang, L. Esaki, and R. Tsu. Resonant tunneling in semiconductor double barriers. *Appl. Phys. Lett.*, 24(12):593, 1974.

[CF02] H. Cords and A. Förster. Berechnung der Temperaturverteilung in einer Gunn Diode. Technical report, Forschungszentrum Jülich GmbH, 2002. FZJ-ZAT-371.

[Cop67a] J. A. Copeland. Characterization of bulk negative-resistance diode behavior. *IEEE Trans. Elec. Dev.*, ED-14(9):461–463, Sept. 1967.

[Cop67b] J. A. Copeland. LSA oscillator-diode theory. *J. Appl. Phys.*, 38(8):3096–3101, July 1967.

[Dav98] J.H. Davies. *The Physics of Low-Dimensional Semiconductors*. Cambridge University Press, 1998.

[Dun65] Dunod, editor. *Instabilities of Current and of Potential Distribution in GaAs and InP*. Proc. Plasma effects in Solids, 1965.

[FML03] A. Foerster, S. Montanari, and M.I. Lepsa. Simulation der Gunn-Dioden I-V Kennlinie. Technical report, ISG-1, Forschungszentrum Juelich, 2003.

[FR99] G. Franz and F. Rinner. Reactive ion etching of GaN and GaAs: Radially uniform processes for rectangular, smooth sidewalls. *J. Vac. Sci. Technol. A*, 17(1):56–61, Jan./Feb. 1999.

[Fra94] G. Franz. *Oberflächentechnologie mit Niederdruckplasmen*. Springer Verlag, 1994.

[Gol29] V.M. Goldschmidt. *Trans Faraday Soc.*, 25:253, 1929.

[Gol91] J.M. Golio. *Microwave MESFETs and HEMT*. Artech House, Motorola, Tempe, Arizona, 1991.

[Gun63] J. B. Gunn. Microwave oscillations of current in III-V semiconductors. *Solid State Commun.*, 1(4):88–91, 1963.

[Gun64] J. B. Gunn. Instabilities of current in III-V semiconductors. *IBM J. Res. Dev.*, 8:141–159, April 1964.

[GWCE88] Z. Greenwald, D. W. Woodard, A. R. Calawa, and L. F. Eastman. The effect of a high energy injection on the performance of mm wave Gunn oscillators. *Solid-State Electron.*, 31(7):1211–1214, July 1988.

[Hak67] B. W. Hakki. Amplification in two-valley semiconductors. *J. Appl. Phys.*, 38(2):808–818, Feb. 1967.

[Hei71] K. Heime. Der Gunn-Effekt. *Der Fernmelde-Ingenieur*, 25:1–29/1–32, Nov./Dec. 1971.

[HFKC62] R. N. Hall, G.E. Fenner, T. J. Kingsley, J. D.and Soltys, and R.O. Carlson. *Phys. Rev. Lett.*, 9:366, 1962.

[Hil62] C. Hilsum. Transferred electron amplifiers and oscillators. *Proc. IRE*, 50:185–189, 1962.

[HLK+03] C.G. Hwang, J.S. Lee, J.H. Kim, N.H. Myung, and J.I. Song. Simple K-band MMIC VCO utilizing a miniaturized hairpin resonator and a three-terminal p-HEMT varactor with low phase noise and high output power properties, 2003.

[Hob72] G.S. Hobson. Velocity-field characteristics for l.s.a. operation. *Solid-State Electronics*, 15:1107, 1972.

[Hob74] G. S. Hobson. *The Gunn Effect*. Clarendon Press, Oxford, 1974.

[HSCK96] S. Hutchinson, J. Stephens, M. Carr, and M. J. Kelly. Implant isolation scheme for current confinement in graded-gap Gunn diodes. *Electron. Lett.*, 32(9):851–852, April 1996.

[IL03] H. Ibach and H. Lueth. *Solid-State Physics*. Springer Verlag, 2003.

[IM] M. Indlekofer and J. Malindretos. Wingreen simulator. http://www.kfa-juelich.de/isg/mbe/software.html.

[Ind99] K. M. Indlekofer. *Transportuntersuchungen und quantenmechanische Beschreibung von Einelektronenstrukturen in Halbleiterheterostrukturen*. PhD thesis, University of Aachen RWTH, 1999.

[Int] SILVACO International. 4071 patrick henry drive, building 1, santa clara, ca 95054.

[Jav03] P. Javorka. *Fabrication and Characterization of AlGaN/GaN High Electron Mobility Transistors*. PhD thesis, University of Aachen RWTH, 2003.

[Kal03] N.E. Kaluza. *MOVPE Growth and Characterization of $Al_xGa_{1-x}N/GaN$ Heterostructures for HEMT application*. PhD thesis, University of Aachen RWTH, 2003.

[Kel96] M.J. Kelly. *Low-Dimensional Semiconductors*. Oxford University Press, 1996.

[KO81] A.P.S. Khanna and J. Obregon. Microwave oscillator analysis. *IEEE Transactions on Microwave Theory and Techniques*, MTT-29:606–608, June 1981.

[KOB+95] J. Kolnik, I.H. Oguzman, K.F. Brennan, Rongping Wang, P.P. Ruden, and Yang Wang. Electronic transport studies of bulk zincblende and wurtzite phases of GaN based on an ensemble Monte Carlo calculation including a full zone band structure. *Journal of Applied Physics*, 78:1033, 1995.

[Krö64] H. Krömer. Theory of the Gunn Effect. *Proc. IEEE*, 52:1736, 1964.

[KSF95] J. Kaindl, S. Sotier, and G. Franz. Dry etching of III/V-semiconductors: Fine tuning of pattern transfer and process control. *J. Electrochem. Soc.*, 142(7):2418–2424, July 1995.

[Kur65] K. Kurokawa. Power Waves and Scattering Matrix. *IEEE Trans. Microwave Theory and Techniques*, 13(2), 1965.

[Lan99] J. Lange. Resonante Tunnelstrukturen im System AlGaAS/InGaAs. Master's thesis, University of Aachen RWTH, 1999.

[Lep97] M.I. Lepsa. *Two and three terminal double barrier resonant tunneling devices.* PhD thesis, University of Eindhoven, 1997.

[LR90] C. Lee and V. Ravaioli. Monte Carlo comparison of heterojunction cathode Gunn oscillators. *Electron. Lett.*, 26(7):425–427, 1990.

[Lüt95] H. Lüth. *Surfaces and Interfaces of Solid Materials*. Springer Verlag, 1995.

[Mak79] T. Makino. Effects of the operational modes on the temperature dependence of the Gunn diode admittance. *Solid-State Electronics*, 22:761, 1979.

[Mal02] J. Malindretos. *Entwicklung und Charakterisierung planarer Resonanz-Tunneldioden für den Einsatz in integrierten digitalen Schaltkreisen*. PhD thesis, University of Aachen RWTH, 2002.

[MC66] D. E. McCumber and A. G. Chynoweth. Theory of negative-conductance amplification and of Gunn instabilities in two-valley semiconductors. *IEEE Trans. Elec. Dev.*, ED-13(1):4–21, Jan. 1966.

[MD82] G.S. Marlow and M.B. Das. The effects of contact size and non-zero metal resistance on the determination of specific contact resistance. *Solid-State Electronics*, 25:91, 1982.

[MM93] K. Maezawa and T. Mizutani. A new resonant tunneling logic gate employing monostable-bistable transition. *Jpn. J. Appl. Phys.*, 32:42–44, 1993.

[MMP+91] G. Millington, R.E. Miles, R.D. Pollard, D.P. Steenson, and J.M. Chamberlain. A resonant tunnelling diode self-oscillating mixer with conversion gain. *IEEE Microwave and Guided Wave Letters*, 1:320, 1991.

[Mor99] Hadis Morkoç. *Nitride Semiconductors and Devices*. Springer-Verlag, 1999.

[NDS+89] S. Neylon, S. Dale, H. Spooner, D. Worley, N. Couch, D. Knight, and J. Ondria. State-of-the-art performance millimetre wave gallium arsenide Gunn diodes using ballistically hot electron injectors. *IEEE 1989 MTT-S International Microwave Symposium Digest*, 1:519–522, 1989.

[Nea97] D.A. Neamen. *Semiconductor Physics and Devices*. Irwin Book Team, The McGraw-Hill Companies, 1997.

[Ond79] J. Ondria. Wide-band mechanically tunable w-band (75-110 ghz) cw Gunn diode oscillator. *AGARD Conference Proc.*, page 12/1, 1979.

[Pac96] Hewlett Packard. Test & measurement application note 95-1, 1996.

[PRA94] S.J. Pearton, F. Ren, and C.R. Abernathy. Low temperature electron cyclotron resonance plasma etching of GaAs, AlGaAs, and GaSb in Cl_2/Ar. *Applied Physics Letters*, 64:1673, 1994.

[Pro04] Cooperation Project. Herstellung und Untersuchung von GaAs Gunn-Dioden, 2000-2004. Forschungzentrum Jülich / Robert Bosch GMBH.

[PSS+04] M. Peden, R. Scurfield, D. Sleet, D. Mohan, A.A. Hyder, E. Jarawan, and C. Mathers. World report on road traffic injury prevention. Technical Report ISBN:9241562609, World Health Organization, 2004.

[QRK+62] T.M. Quist, R.H. Rediker, R.J. Keyes, W.E. Krag, B. Lax, A. L. McWhorter, and H. J. Zeiger. *Appl. Phys. Lett.*, 1:91, 1962.

[Riz01] A. Rizzi. Private communications, 2001.

[RW61] B. K. Ridley and T. B. Watkins. The possibility of negative resistance effects in semiconductors. *Proc. Phys. Soc.*, 78:293–304, 1961.

[SHMS98] J.P. Sun, G.I. Haddad, P. Mazumder, and J.N. Schulman. Resonant tunneling diodes: models and properties. *Proceedings of the IEEE.*, 86(4):641–660, April 1998.

[SMI+01] J. Stock, J. Malindretos, K.M. Indlekofer, M. Pottgens, A. Forster, and H. Luth. A vertical resonant tunneling transistor for application in digital logic circuits. *IEEE Transactions on Electron Devices*, 48:1028, 2001.

[SQI01] J. Sor, Y. Qian, and T. Ithoh. Miniature low-loss cpw periodic structures for filter applications. *IEEE MTT-S*, 49(12):2336–2341, 2001.

[Sto99] J. Stock. Herstellung eines vertikalen resonanten Tunneltransistors und Charakterisierung der Eigenschaften bei Raumtemperatur. Master's thesis, Universoty of Aachen RWTH, 1999.

[Sto03] J. Stock. *Herstellung und Charakterisierung von GaAs Gunn-Dioden für Anwendungen bei 77 GHz*. PhD thesis, University of Aachen RWTH, 2003.

[Sze81] S. M. Sze. *Physics of Semiconductor Devices*. Wiley-Interscience, 2 edition edition, 1981.

[Sze98] S. M. Sze. *Modern Semiconductor Device Physics*. John Wiley & Sons, 1998.

[TE73] R. Tsu and L. Esaki. Tunneling in a finite superlattice. *Applied Physics Letters*, 22(11):562–564, 1973.

[V.903] Sonnet Software V.9. 100 Elwood Davis Road North Syracuse, NY13212, 2003. www.sonnetsoftware.com.

[vdP58] L. J. van der Pauw. A method of measuring specific resistivity and hall effect of discs of arbitrary shape. Technical report, Philips Res. Reports, 13,1-9 1958.

[vH95] J. G. van Hassel. *Dry Processing of GaAs-Based MESFETs and Pseudomorphic HFETs*. PhD thesis, Technische Universität Eindhoven, 1995.

[VRJ+01] P. Visconti, M.A. Reshchikov, K.M. Jones, F. Yun, D.F. Wang, R. Cingolani, H. Morkoc, C.W. Litton, and R.J. Molnar. Highly selective photoenhanced wet etching of GaN for defect investigation and device fabrication. *GaN Related Alloys - Symposium*, page G3.14.1, 2001.

[War66] F. L. Warner. Extension of the Gunn-Effect Theory. *Elec. Lett.*, 2(7):260–261, July 1966.

[Was03] R. Waser. *Nanoelectronics and Information Technology: Advanced Electronic Materials and Novel Devices*. Wiley-VCH Verlag, 2003.

Acknowledgement

This dissertation was carried out at the institute ISG1 of Forschungzentrum Jülich. The success of this work would not have been possible without an excellent guidance, support and cooperation. Among others, I would like to acknowledge and say thanks to the following people :

Prof. Dr. *H. Lüth* for the great opportunity to perform my PhD work in Germany. His great enthusiasm in scientific research combined with the friendly atmosphere made the last three years a wonderful experience.

Prof. Dr. *R. Waser* for kindly accepting to referee this work.

Prof. Dr. *A. Förster* for being my research advisor during the last three years. He has constantly amazed me with his ability to simplify complicated research problems. I would like to express my deepest gratitude to him for showing to an engineer how interesting solid state physics could be.

Dr. *M. Lepsa* for sharing with me his extraordinary experience in semiconductor processing and physics. Despite my repeated failures, his enthusiasm and strong support motivated me to finally succeed in this project. Also, many thanks for the fruitful discussions and for the critical review of this work.

Dr. *M. Indlekofer* for the helpful suggestions, the many explanations, the excellent simulation program Wingreen, and the review of this work.

Dr. *J. Stock* for the introduction to the clean room activities and for the helpful advices with plasma etching. The friendly atmosphere in the office during the first two years developed, later, in an excellent external collaboration.

Mr. *J. Wensorra* for many interesting not only scientific discussions.

Dr. *R. Calarco*, Dipl. Ing. *M Bertelli*, Dipl. Ing. C. *Varini*, Dipl. Phys. *E. Dona* and Prof. Dr. *A. Rizzi* for helping me not to forget the Italian language during the three long years in Germany. The topic did not matter: politics, sport, military service or cooking, there was always a reason for a funny remark.

Mr.*C. Krause* for the outstanding MBE growths and for the numerous metal depositions.

Dr. *N. Kaluza*, Dr. *H. Hardtdegen* and Dipl. Ing. *R. Steins* for the excellent epitaxial growth of GaN for nanocolumns and Gunn diodes.

Dr. *R. Calarco*, Dipl. Phys. *R. Meijers*, Mr. *T. Richter* and Dipl. Phys. *N. Thillosen* for sharing with me the nanocolumns topic. I am also grateful to *R. Meijers* for helping me with the AFM measurements.

Dr. *D. Freundt* and his group from Bosch GmbH for the intensive cooperation regarding the ACC project. The collaboration gave me the chance to familiarize with the working attitude of a big international group.

Mr. *F. Mohammed* for his diligent work about short pulse measurements and for his very nice personality.

Dipl. Ing. *A. Fox*, Dr. Ing. *M. Marso* and Prof. Dr. Ing. Kordoš for the interesting discussions in the field of high frequency devices and the disposal of the S-parameter characterization setup.

Mrs. *I. Schumacher*, Miss *M. Gruber* and Miss *M. Tödt* for the help and support in solving all kind of administrative problems.

Dipl. Ing. *A. Steffen* and *J. Müller*, as well as all co-workers of the clean-room for their help with processing of the samples. Dipl. Ing. *F. Ringelmann* for the introduction to plasma etching, the professional interest in my work and for the RIE maintenance. Miss. *A. Pracht*, Mr. *J. Zillikens* and Mr. *H. Wingens* for the numerous metal depositions. Miss. *S. Bunte* for precise cutting of the GaN samples.

Mrs. *M. Nonn*, an example of efficiency and accuracy, for the excellent lithography masks and Dr. *A. van der Hart* for the electron beam lithography with proximity-correction.

Dipl. Ing. *H.P. Bochem* and Mrs. *E. Brauweiler-Reuters* for the several and high quality SEM images.

Dr. *S. Vitusevych*, Dr. *S. Danylyuk* and Dr. *A. Kluschin* for the disposal of the high frequency mixers and spectrum analyzers.

Dipl. Ing. *J. Bernát* and Dr. Ing. *P. Javorka* for the helpful tips in the GaN device processing.

PD Dr. *T. Schäpers*, Dr. *M. Mikulics*, Mr. *K. Wambach*, Mr. *K. Nicoll*, Dr. *J. Malindratos*, Dr. *V. Guzenko*, Dr. *M. Kočan*, Dr. *R. Adam*, Dr. *P. Vagner*, Dr. *M. Wolters*, Dr. *J. Moers*, Dr *I. Batov* , Prof. Dr. *P. Kordoš*, Dr. *L. Vescan*, Dr. *S. Trellenkamp*, Dr. *M. von der Ahe*, Dr. *A. Tönnesmann*, Dr. *T. Stoica*, Dr. *M. Goryll*, Dipl. Ing. *G. Heidelberg* and Dr. *G. Crecelius* for attributing to this work in various ways.

Dipl. Geol. *M. Kloppisch* for her permanent moral support and the constant help in learning the German language. I am grateful for the review of my numerous German texts.

The administrative and technical coworker as well as all other not namely mentioned people for their versatile support and kindness.

Schriften des Forschungszentrums Jülich
Reihe Informationstechnik / Information Technology

1. **SAM – Untersuchung von Aushandlungen in Gruppen mittels Agentensimulation**
   von N. Lepperhoff (2002), VI, 278 Seiten
   ISBN: 3-89336-298-3

2. **Praxisbezogene IDL-Programmierung**
   von M. Busch, R. Bauer, H. Heer, M. Wagener (2002), XVI, 216 Seiten, 12 farb. Abb.
   ISBN: 3-89336-308-4

3. **Segmentierung von Volumendatensätzen mittels dreidimensionaler hierarchischer Inselstrukturen**
   von J.-F. Vogelbruch (2002), V, 191 Seiten, zahlr. farb. Abb.
   ISBN: 3-89336-309-2

4. **ComputerMathematik mit Maple**
   von J. Grotendorst (2003), VI, 274 Seiten mit beiliegender CD-ROM, zahlr. farb. Abb.
   ISBN: 3-89336-325-4

5. **ComputerMathematik mit Maple – Zweite überarbeitete und erweiterte Auflage**
   von J. Grotendorst (2004), VI, 294 Seiten mit beiliegender CD-ROM, zahlr. farb. Abb.
   ISBN: 3-89336-354-8

6. **The Internet in Germany: Atlas of Providers and Regions**
   by N. Lepperhoff, W. Fischer (2004), VIII, 103 pages, many coloured fig.
   ISBN: 3-89336-358-0

7. **Störstellen in Galliumnitrid-basierenden Transistoren**
   von M.J. Wolter (2004), V, 132 Seiten, 19 farb. Abb.
   ISBN: 3-89336-361-0

8. **Programming in C++: Audio-Visual Lecture of the course "Object-oriented programming in C++"**
   von B. Mohr, M. Boltes, R. Koschmieder (2004), DVD (18 hours, 22 minutes recorded in 15 sessions)
   ISBN: 3-89336-369-6

9. **Fabrication and characterization of planar Gunn diodes for Monolithic Microwave Integrated Circuits**
   by S. Montanari (2005), c. 150 pages, 26 col. fig.
   ISBN: 3-89336-396-3

Simone Montanari was born in Sassuolo (Modena, Italy) and studied information engineering at the University of Modena with specialization in electronics and telecommunications. He completed his studies with his master-thesis in 2001 at the ISI institute in Research Centre Jülich (Germany) on Pseudomorphic and Metamorphic AlInAs/InGaAs HEMTs under the supervision of Prof. P. Kordoš. Afterwards, he joined the group of Prof. H. Lüth and Prof. A. Förster (ISG-1 Research Centre Jülich) investigating on Gunn diode based microwave generation. He submitted his Ph.D. dissertation at the faculty of Electrical Engineering of the University of Aachen (RWTH, Germany) in January 2005. He is currently working by Robert BOSCH GmbH in the field of semiconductor device failure analysis.

Forschungszentrum Jülich
in der Helmholtz-Gemeinschaft

Band/Volume 9
ISBN 3-89336-396-3

Informationstechnik
Information Technology